Calibrating the Electromagnetic Calorimeter of T2K

PhD Experimental Particle Physics Thesis

M. A. George

August, 2010

Abstract

In this thesis, I describe the first calibration of the T2K ND280 electromagnetic calorimeter using cosmic muons. T2K is a long baseline neutrino oscillation experiment whose main aim is to observe for the first time the $\nu_\mu \to \nu_e$ oscillations. A complete understanding of the ν_μ disappearance or $\nu_\mu \to \nu_x$ oscillations, $x = \mu$ or τ, and neutrino–nucleon interactions will complete the T2K physics programme.

T2K produces an intense muon neutrino beam at the J-PARC facility on Japan's East coast. This neutrino beam is then detected twice: once 280 m from its start by ND280—whose purpose is to characterise the beam—and then again 295 km away at the far detector Super-Kamiokande on the West coast of Japan. One of the components of the ND280 detector is the electromagnetic calorimeter.

A thorough understanding of the electromagnetic calorimeter is crucial. In this thesis I first describe the quality assurance of the photosensors used in the calorimeter. Then I describe the cosmic muon flux simulation, that I adapted from CORSIKA for the electromagnetic calorimeter studies, and now adopted by the whole T2K collaboration. This is followed by a description of calibration of the calorimeter using the cosmic muon flux, in particular the light yield attenuation, and finally the comparison of the results obtained with cosmic muons taken at two different locations, CERN and Tokai. Moreover, I describe the ND280 Workbook, an online guide to the ND280 software, including tutorials and information for all the ND280 collaborators, that I developed in its entirety.

Dedication

This thesis is dedicated to my mum Joan George—you are always my inspiration and my strength.

Thank you.

Acknowledgements

I would like to start by thanking my colleagues on the T2K collaboration for the many useful insights and the helpful feedback I gave received over the past few years, and the odd karaoke night or two... In particular, I would like to thank everyone on T2K UK. It has been a pleasure to work with so many brilliant physicists and I am now lucky enough to call many of you friends.

My supervisor Francesca DiLodovico and everyone at Queen Mary University of London—thank you so much for your help and support, it has been great working with you.

I also owe a huge debt of gratitude to my senior school school teacher Peter Moore, who first nurtured my love of physics—those hours discussing degree level topics , chalk in hand (even when you were no longer my teacher) were not wasted!

I must also thank Antonella De Santo—my third year project supervisor—the skills that you taught me were essential to my PhD.

Last but by no means least I would like to thank my mum and my partner. I am so lucky to have you both—you have made this period so much easier and happier for me—I love you both. To my friends—thank you so much for your constant support and for putting up with me over these last few months and for sticking by me even though you have probably forgotten what I look like.

Contents

List of Figures

1 Introduction

The Tokai-to-Kamioka T2K experiment is a long baseline neutrino oscillation experiment. A neutrino beam is created at the proton synchrotron at the J-PARC facility in Tokai on the East coast of Japan and travels the 295 km to Japan's West coast where it is detected at the Super-Kamiokande (Super-K) detector in Kamioka. The experiment aims to answer many of the remaining questions in neutrino oscillations: to narrow down the value of θ_{13}, to find whether θ_{23} mixing is maximal (i.e. θ_{23} close to 45°), to help determine (in contribution with other experiments) the sign of Δm^2_{23} and to move us closer to knowing whether neutrino oscillations could be *CP* violating. To do this we must examine changes in the beam which are due to oscillations. In order to to understand how the constituent particles which make up the beam have changed and hence analyse the oscillation parameters, we must first understand the beam constituents at its origin and then detect the beam again after possible oscillation. To do this we need two detectors, the first—close to the source of the beam—to determine the beam's initial make-up and in addition a second detector—after some distance—to detect the beam after oscillation. T2K's near detectors ND280 are situated at 280 m from the target at J-PARC and are made up of one on-axis and one off-axis detector working together to observe the beam with necessary accuracy.

The electromagnetic calorimeter or ECal has 13 modules which encompass the inner off-axis detector. These ECal modules were built, commissioned and tested by the UK collaboration and have therefore been the focus of much of my work. Cosmic muons are essential to the calibration of this detector and its photosensors.

The thesis contains details of my major contributions to the T2K collab-

oration. My work assembling and testing the multi-pixel photon counters (MPPC's), which are used in all but one of the ND280 sub-detectors. I describe the ND280 software suite which I have helped in the development of and used to do much of my work—as well as producing the Workbook that is an in-depth guide to the software, its use, instructions for developers and guides to those beginning work in the ND280 T2K collaboration. I describe my production of the cosmic muon flux—which is now the standard ND280 cosmic flux MC, used by all ND280 sub-detector groups for calibration and MC data comparisons etc. As leader of the UK ECal cosmic muon analysis group, I determined and oversaw much of the calibration and analysis work, which I present here along with my own contributions to the ECal calibration and analysis effort. I describe my work to produce the attenuation constants for each bar of the DSECal and future ECal modules and comparisons between cosmic MC and data for the CERN calibration runs.

2 Neutrino Oscillations

Neutrinos are fermions belonging to the lepton sector of particles and are electrically neutral. There are three "flavours" of neutrino, named after its charged lepton counterparts: electron (e), muon (μ) and tau (τ), each with their equivalent anti-particle. They can only interact via the weak force and can undergo charged-current and neutral-current interactions. The weak force gives rise to very small cross sections at low energies, making neutrinos highly penetrating particles, meaning that they can travel through many light years of material without a single interaction. They are left-handed particles (right-handed anti-particles) and therefore their spin and moment are known to be in opposing directions (the helicity of a particle is Left-handed if the direction of its spin is opposite to the direction of its motion, whereas it is Right-handed if its spin and momentum are opposite).

Naturally produced neutrinos originate from cosmic ray interactions in the atmosphere and pp and CNO (hydrogen burning) reactions in the Sun (as well as all other stars, including supernovae and relic neutrinos from the formation of the universe). They are also produced in beta decays, in nuclear reactors and at accelerators.

The existence of the neutrino was first postulated by Wolfgang Pauli in 1930. In a letter to the participants of the Tübingen conference on radioactivity, he proposed a solution to the problem that the products of nuclear beta decay sum to less than that required by the laws of conservation of energy [1].

Due to the illusive nature of the neutrino it was another twenty-five years before the first neutrino was observed by Frederick Reines and Clyde Cowan of the Los Alamos National Laboratory [2], who, in 1955 discovered the electron neutrino. Their detector had a cross-sectional area of $\sim 2\text{m}^2$ and consisted

of two 100 litre tanks of water with cadmium chloride (CdCl) dissolved in each, with scintillator layers in between and on either side of the tanks. Every scintillator layer was read out by photomultiplier tubes. Electron neutrinos were identified by the flashes of scintillation light made in the scintillator by the production of an electron in ν_e charged current interactions. Despite the high level of neutrino flux produced by the reactor, neutrino interactions were extremely rare, with a signal rate of only three events per hour. Nevertheless the electron neutrino was observed and subsequently—in 1995—Reines and Cowan were awarded the Nobel Prize for their momentous contribution to particle physics.

The muon neutrino was the next to be discovered in 1962 by Leon Lederman, Melvin Schwartz and Jack Steinberger of Brookhaven National Laboratory [3]. After the discovery of the τ lepton in 1975, it became apparent that there should also be a tau neutrino, ν_τ, which, having undergone a charged-current interaction, would produce a τ lepton. The direct production of a tau lepton from a ν_τ charged current interactions was finally achieved at Fermilab in 2000 by the DONUT experiment [4], more than thirty years after the discovery of the first two neutrino flavours. DONUT used the Tevatron accelerator to produce an intense neutrino beam, thought to contain all three neutrino flavours. The detector consisted of a long target of iron plates, sandwiched between layers of emulsion which recorded particle interactions. The neutrino beam passed through this detector, where one in every $1 \times 10^{12} \nu_\tau$ interacted with an iron nucleus to become a tau lepton. This tau decays quickly but its decay can be observed by the three-dimensional track seen in the emulsion. The millions of candidate tracks were narrowed down to ~ 1000, via the application of appropriate event selections, and finally four of these tracks were

demonstrated to show the production of a tau lepton and its decay.

Neutrino physics and the search for the three neutrino flavours, which spanned over 59 years, has lead to one of the most exciting periods in particle physics. Due to the atmospheric neutrino anomaly and the solar neutrino deficit problem, which are explained below, we have shown through experiment, that neutrinos have mass and that they oscillate (change flavour over some distance travelled). Neutrino oscillations were first postulated in 1957 by Bruno Pontecorvo [5] and independently in 1962 by Maki, Nakagawa and Sakata [6], but, especially since the introduction of the standard model of particle physics, were considered implausible since, for oscillations to occur, neutrinos must have mass, not suggested by the model. Neutrino oscillations are the first direct evidence of physics beyond the Standard Model [7], which has, until now, proved reliable and have paved the way for new physics—and one day, for a new model of particle physics.

We have yet to probe many aspects of neutrino oscillations including their suggested *CP* violation—a contributor to the matter anti-matter asymmetry of the universe. T2K aims to answer many of these questions. An explanation of neutrino oscillations will follow, considering the simplified two flavour and full three flavour models, the fixed and experimental parameters involved and oscillations propagated in both matter and a vacuum are examined.

2.1 The Solar Neutrino Deficit

Solar neutrinos, specifically electron neutrinos, originate from the pp chain (Figure 1) and and stellar fusion reactions (CNO cycle (Figure 2)) reactions which take place in the Sun. The pp chain contributes $\sim 98\%$ of the total solar neutrino flux, which in turn contributes a mere 2% to the total solar

energy emitted; the rest is emitted in the form of photons. Although we cannot directly observe the centre of the Sun, due to the short mean free path of photons, we do have a thorough understanding of the solar interior, its reactions and processes. The 'luminosity constraint' argument, for example, uses the solar luminosity $= 2.4 \times 10^{39}\text{MeVs}^{-1}$ known to an accuracy of ~ 0.4 %, to predict the solar neutrino flux. Since we know from the pp and CNO reactions combined that two neutrinos are associated with an energy release of $\sim 26.73\,\text{MeV}$, see Equation 1, we can use this fact, together with the knowledge of the solar luminosity, to predict that the electron neutrino flux, in the absence of oscillations, will be $\sim 6.4 \times 10^{10}\text{cm}^{-2}\text{s}^{-1}$, see Reference [8].

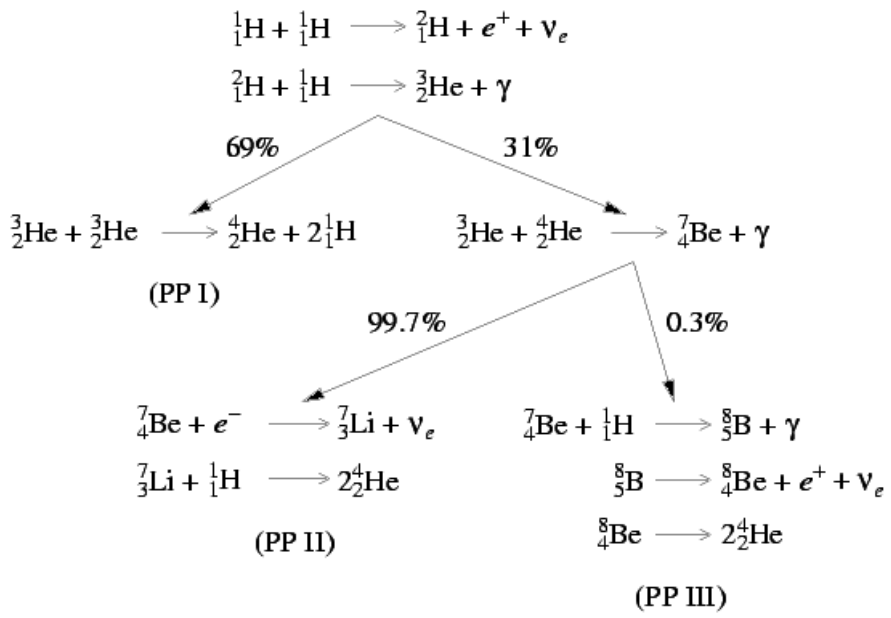

Figure 1: The proton-proton chain reaction which converts hydrogen to helium in the Sun [9].

$$4p + 2e^- \rightarrow He + 2\nu_e + 26.73\text{MeV} \tag{1}$$

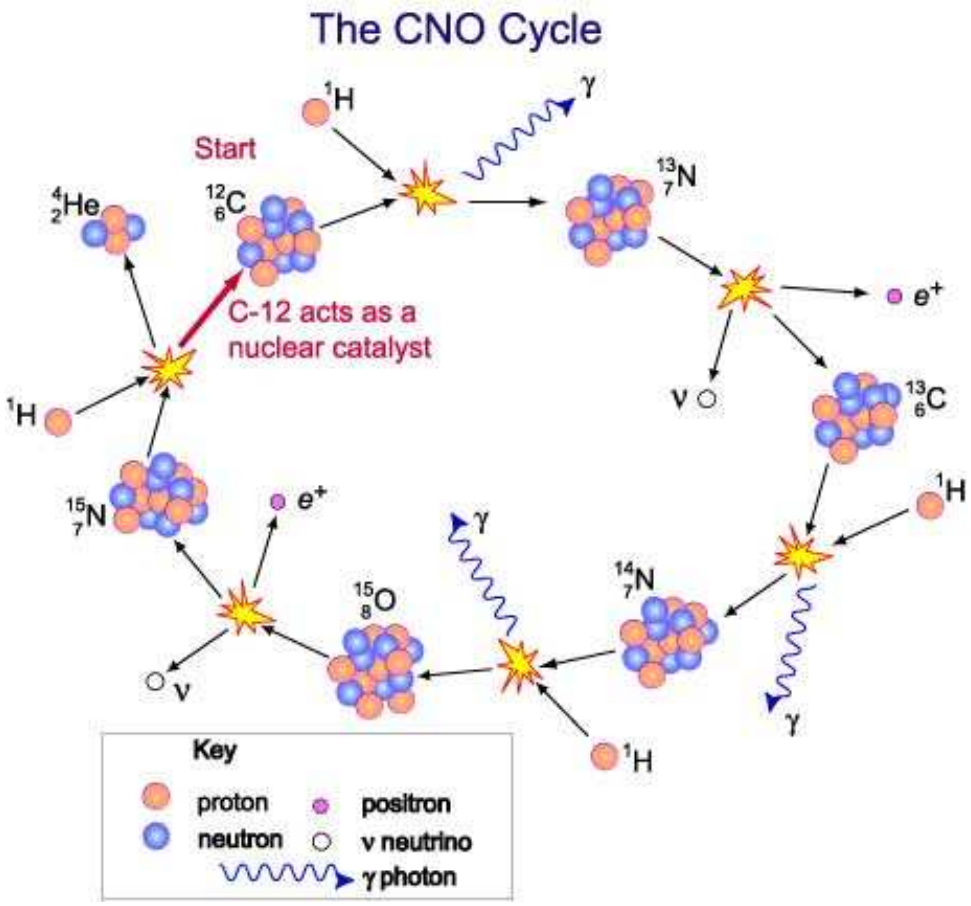

Figure 2: The carbon nitrogen oxygen cycle which takes place with nuclear fusion in the Sun [10].

Our understanding, from this and many other arguments, allows us to predict accurately the electron neutrino flux produced in the Sun. As the neutrino's cross section for interaction is so small, we expect to observe the same electron neutrino flux (to within a few percent) at the detector. However—experimentally—the flux is seen to be reduced to ∼50% of that expected.

The solar neutrino deficit problem was first solved by the SNO [11] heavy water (D_2O) experiment in Canada and then the KamLAND [12] experiment in Japan, showed that this was due to neutrino oscillations.

2.1.1 Solar Neutrino Models

There have been many prominent and significant solar models which can accurately predict solar neutrino energies and flux. The most accredited and scientifically accepted of these is the Bahcall-Pinsonneault Standard Solar Model (BP-SSM) [8]. The BP-SSM has been used by many successful experiments which search for neutrino oscillations and is accepted as accurate. There have been many versions of the BP-SSM, becoming increasingly more accurate each time. Figure 3 shows the solar neutrino flux (vertical axis) and range of neutrino energies (horizontal axis) expected in the absence of oscillations from the pp chain reactions in the Sun using the BP-SSM version produced in 2000 (BP2000). The lines shown on the plot represent the reaction that produces the neutrino flux (e.g. pep, hep etc.) and gives the uncertainties in the calculations. The energy thresholds for some solar neutrino experiments are shown at the top of the plot.

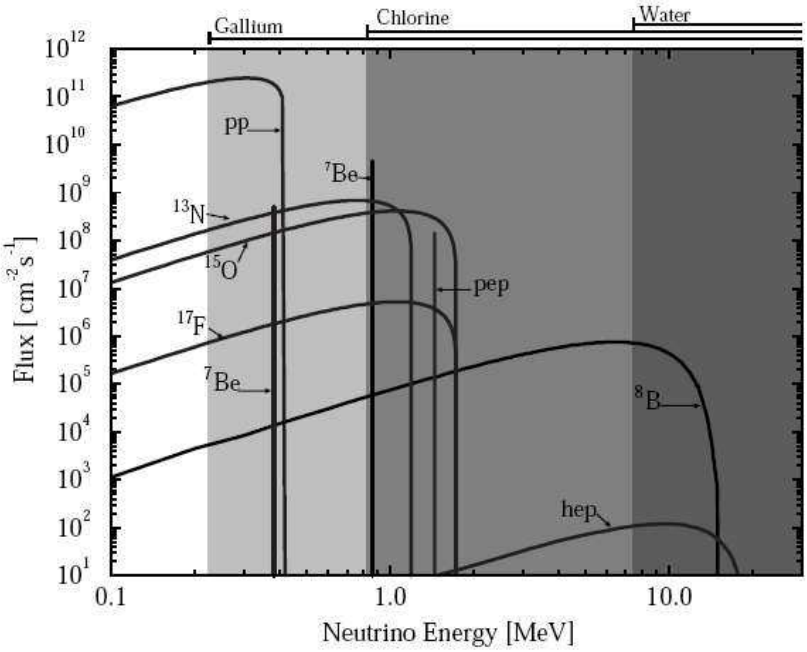

Figure 3: The solar neutrino flux as a function of neutrino energy in the absence of neutrino oscillations, from the pp chain reactions in the Sun using BP2000.

2.2 The Atmospheric Neutrino Anomaly

Atmospheric neutrinos are produced through the decay of kaons (K's) and pions (π's), which are produced as secondary particles by cosmic ray interactions in the upper atmosphere (see Figure 4).

Most of these K's and π's will decay according to the reaction shown in Equation 2, if their energy is low enough ($\sim 2\,\mathrm{GeV}$), then it is likely that the neutrinos they produce will arrive at Earth.

$$P + n \rightarrow \pi^{\pm} + ...\pi^{\pm} \rightarrow \mu^{\pm} + \nu_{\mu} + \bar{\nu_{\mu}}\mu^{\pm} \rightarrow e^{\pm} + \nu_{e}(\bar{\nu_{e}}) + \nu_{\mu}(\bar{\nu_{\mu}}) \qquad (2)$$

The absolute neutrino flux is difficult to calculate since it requires the knowledge of the original cosmic ray flux and consequently results in large uncertainties of around 20%. Nevertheless, the ratio of muon neutrino over

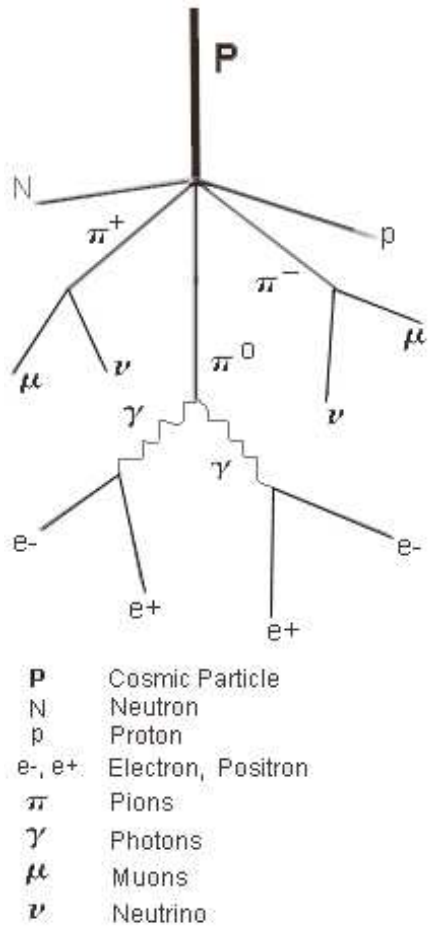

Figure 4: Cosmic rays incident on the upper atmosphere produce showers through which neutrinos are produced [13].

electron neutrino fluxes can be calculated with much greater precision. We can see from Equation 3 that two muon neutrinos or anti muon neutrinos are produced for every electron or anti-electron neutrino and therefore, the ratio in the absence of oscillations is expected to be ~ 2:

$$R = \frac{N(\nu_\mu) + N(\bar{\nu_\mu})}{N(\nu_e) + N(\bar{\nu_e})} = 2. \tag{3}$$

The theoretical error on this ratio is of the order of 5%, see Reference [14]. However, a smaller ratio than expected is detected from numerous experiments. This depleted ratio is believed to be dominated by $\nu_\mu \rightarrow \nu_\tau$ oscillations.

Atmospheric neutrino oscillations were investigated at Super-Kamiokande [15], now the far detector of T2K, which showed a suppression in the atmospheric muon neutrino flux, consistent with atmospheric neutrino oscillations. This was later confirmed by the K2K [16] (a forerunner of T2K) and MINOS [17] experiments.

2.3 Oscillations in a Vacuum

2.3.1 The Two Flavour Model

A neutrino produced at the source at a time $t = 0$ will evolve following the Schrödinger equation. So that after a time t and a distance travelled L, there is a non-zero probability of finding the neutrino in a different flavour eigenstate. For the case of two flavour oscillations the mixing matrix U is:

$$U = \begin{pmatrix} \cos\theta & \sin\theta \\ -\sin\theta & \cos\theta \end{pmatrix} \tag{4}$$

where θ represents the mixing angle between the two flavours to be considered and parameterises the strength of the coupling between the two flavours.

The probability of a neutrino oscillating from a neutrino of flavour α to a neutrino of flavour β, in a vacuum, occurs according to the formula:

$$P(\nu_\alpha \rightarrow \nu_\beta) = \sin^2 2\theta \sin^2(\frac{1.27\Delta m^2(\mathrm{eV}^2)L(\mathrm{km})}{E(\mathrm{GeV})}) \tag{5}$$

where $\Delta m^2 = m^2_{1\alpha} - m^2_{2\beta}$ (1 and 2 indicate the mass eigenstates), E and L are the neutrino energy and the distance from where the neutrino is produced to its detection point, respectively. While Δm^2 and θ are the physical parameters that we want to measure, E and L depend on the experiment performed.

Whilst this two flavour model has been a good approximation, as we move to higher precisions to answer the current pertinent questions, the three flavour model must be considered. Neutrinos have three mass states (ν_1, ν_2, ν_3) and their mixing is described by three independent mixing angles $(\theta_{12}, \theta_{23}, \theta_{13})$, two independent signed mass-squared differences $(\Delta m^2_{12}, \Delta m^2_{23})$ and one *CP*-violating phase angle (δ).

2.3.2 The Three Flavour Model

In the case of three flavour neutrino mixing, we can consider the weak eigenstates ν_α (where $\alpha = e, \mu, \tau$) as linear combinations of the mass eigenstates ν_i (where $i = 1, 2, 3$). They combine to form the elements $U_{\alpha i}$ of the standard 3x3 unitarity matrix for Dirac neutrinos U. The commonly used representation of U is:

$$U = \begin{pmatrix} c_{12}c_{13} & s_{12}c_{13} & s_{13}e^{-i\delta} \\ -s_{12}c_{23} - c_{12}s_{23}s_{13}e^{i\delta} & c_{12}c_{23} - s_{12}s_{23}s_{13}e^{i\delta} & s_{23}c_{13} \\ s_{12}s_{23} - c_{12}c_{23}s_{13}e^{i\delta} & -c_{12}s_{23} - s_{12}c_{23}s_{13}e^{i\delta} & c_{23}c_{13} \end{pmatrix} \tag{6}$$

where $c_{ij} = \cos\theta_{ij}$ and $s_{ij} = \sin\theta_{ij}$ $(i, j = 1, 2, 3$ are the generation labels

and θ_{ij} = the mixing angle) and δ is the CP violating phase. A total of three angles (θ_{ij}) and a phase (δ) are free parameters in the case of the three flavour model.

Currently, we only have limits on the value of θ_{13} and do not know whether θ_{23} mixing is maximal, in addition to not knowing the value of δ.

A neutrino of state $|\nu_\alpha\rangle$ at time $t = 0$ will evolve according to the Schrödinger equation and after $t > 0$ it will then be in a state as Equation 7:

$$|\nu_\alpha(t > 0)\rangle = \sum_i e^{-iE_i t} U^*_{\alpha i} |\nu_i\rangle = \sum_\beta \sum_i U_{\beta i} e^{-iE_i t} U^*_{\alpha i} |\nu_i\rangle \tag{7}$$

where $U_{\alpha i}$ are the elements of a unitarity matrix, $U^*_{\alpha i}$ represents its conjugate transpose i.e. $U^*U = UU^* = I_n$ and E = energy.

Therefore, after some algebra, the probability of finding the neutrino of flavour state α in a different flavour state β after a distance travelled $L \simeq t$ is non-zero and is given by Equation 8:

$$P(\nu_\alpha \to \nu_\beta) = |\langle \nu_\beta(t) | \nu_\alpha \rangle|^2 = |\sum_i U_{\beta i} e^{-iE_i t} U^*_{\alpha i}|^2. \tag{8}$$

Thus the probability of oscillation among all neutrino flavours becomes Equation 9:

$$P(\nu_\alpha \to \nu_\beta) = \sum_i |U_{\beta i}|^2 |U_{\alpha i}|^2 + 2Re \sum_{j>i} U_{\beta i} U^*_{\beta j} U^*_{\alpha i} U_{\alpha j} exp(-i \frac{\Delta m^2_{jk} L}{2E}). \tag{9}$$

2.4 Oscillations in Matter

Matter effects can increase the probability of neutrino oscillations since the indices of refraction in matter for $\nu_\mu \neq \nu_e$. Neutrino scattering from electrons,

protons and neutrons increases, while the incoherent elastic and the quasi-elastic scattering, in which the states of the initial particles change in the process does not effect the oscillations. The interplay between non flavour changing neutrino interactions and neutrino mixing, results in an oscillation probability which is quite different from that in a vacuum. First considered by Mikheyev, Smirnov and Wolfenstein [18] this is known as the MSW effect. All neutrino flavours can interact via neutral current interactions propagated via exchange of the Z boson, whilst only electron neutrinos can undergo charge current interactions via exchange of the W boson.

These matter effects are relevant to solar neutrinos and those travelling through the Earth i.e. upward going neutrinos (although obviously the matter effects from the Earth are much less prevalent than the Sun since the Earth is much less dense). The matter effect is negligible in T2K, as the distance between the neutrino source and Super-K is 'only' 295 km. Nonetheless for completeness the oscillation probability is included here(10).

$$P(\nu_\alpha \rightarrow \nu_\beta) = \sum_i |U_{\beta i}|^2 |U_{\alpha i}|^2 + 2Re \sum_{j>i} U_{\beta i} U^*_{\beta j} U^*_{\alpha i} U_{\alpha j} \exp(-i \frac{\Delta m^2_{ji} L}{2E}) \quad (10)$$

where Δm^2_{ij} are the effective neutrino mass differences in matter.

2.5 The Experimental Landscape

Super-Kamiokande was the first experiment to observe atmospheric $\nu_\mu \rightarrow \nu_\tau$ oscillations in 1998 through the observation of ν_μ disappearance and made initial measurements of $\sin^2 2\theta$ and Δm^2 of 1 and $2.4 \times 10^{-3}\,\mathrm{eV}^2$, respectively.

The first observations of the solar neutrino deficit due to $\nu_e \rightarrow \nu_x$ where $x = \mu$ or τ oscillations were made at SNO in 2001-02 and were confirmed to be

due to oscillations by KamLAND in 2002 (in collaboration with other neutrino oscillation experiments). A combination of the KamLAND results and the global fit for solar neutrino fluxes found that the best fit for solar neutrino oscillation parameters using the two flavour neutrino oscillation approximation to be $\theta_{12} = 37°, \Delta m^2_{21} = 7.6 \times 10^{-5}\,\mathrm{eV}^2$ [12].

KamLAND was one of the first reactor–based neutrino oscillation experiments. Such experiments measure the survival probability—or disappearance—of neutrinos produced in fission reactions in nuclear reactors. The energy of the neutrinos produced will be roughly equal at a value depending upon the type of fuel and the degree to which it is burning. This survival probability is given by Equation 11:

$$P(\nu_e \rightarrow \nu_e) = 1 - (\sin^2 2\theta_{13} \sin^2 \frac{\Delta m^2_{32}}{4E_\nu} L - \cos^4 \theta_{13} \sin^2 \theta_{12} \sin^2 \frac{\Delta m^2_{21}}{4E_\nu} L) \quad (11)$$

Hence reactor experiments can be sensitive to both the atmospheric and solar (e.g. θ_{12}) neutrino oscillation terms, depending upon the baseline of the experiment (where a short baseline enables the atmospheric terms to be measured). In fact the current best limit on the value of θ_{13} was made by the CHOOZ [19] reactor experiment in France in around 2000. While the CHOOZ experiment found no evidence of $\overline{\nu}_e$ disappearance at the 90%CL for $\Delta m^2 > 7 \times 10^{-4}$ at maximum mixing and $\sin^2 2\theta = 0.1$ (using the simple two flavour model), it found a limit of $\sin^2 2\theta_{13} < 0.1$ for the best fit of Δm^2 from atmospheric neutrino oscillations.

K2K was the first accelerator based neutrino oscillation experiment. It uses Super-Kamiokande (the same far detector as T2K) as the far detector 250 km away from the neutrino production site in KEK Japan. More recently,

Δm^2_{21}	$\simeq 7.6 \pm 0.35 \times 10^{-5}\,\mathrm{eV}^2$
Δm^2_{32}	$2.43 \pm 0.13 \times 10^{-3}\,\mathrm{eV}^2$ at 68% C.L.
Δm^2_{31}	$+2.46^{+0.47}_{-0.42}, c - 2.37^{+0.43}_{-0.46} \times 10^{-3}\,\mathrm{eV}^2$ 19% at3σ
$\sin^2 2\theta_{\mu\mu} = \sin^2 2\theta_{23} \cdot \cos^4 2\theta_{13}$	$> 0.89 \pm 0.11$
$\sin^2 2\theta_{13}$	< 0.05 at 3σ
$\sin^2 \theta_{23}$	$< 0.45^{+0.16}_{-0.09}$ 35%
$\sin^2 2\theta_{13}$	< 0.12 at 90% C.L.
$\sin^2 \theta_{12}$	$< 0.32^{+0.08}_{-0.06}$ 25% at 3σ

Table 1: Experimental constraints to oscillation parameters.

the MINOS experiment produces a $\nu_\mu/\overline{\nu}_\mu$ beam at Fermilab in the USA, with the far detector in the Soudan mine 735 km away. MINOS is looking for ν_μ and $\overline{\nu}_\mu$ disappearance and ν_e appearance. The latest preliminary results from MINOS as of July 2010 can be seen in Figure 5 for ν_μ disappearance, Figure 6 for $\overline{\nu}_\mu$ disappearance and Figure 7 for sterile neutrino searches. Since all active neutrino flavors participate in the neutral-current interaction, while sterile neutrinos do not, MINOS can look for evidence of sterile neutrinos by comparing the rates of neutral-current interactions in the near and far detectors but—like MiniBooNE, a Fermilab based experiment aiming to observe neutrino oscillations from a muon neutrino beam using a mineral oil filled detector [20]—they have found no evidence for this.

These experiments, collectively, have led to many constraints, see Table 1.

T2K is now perfectly placed to build on the knowledge and expertise of these previous experiments.

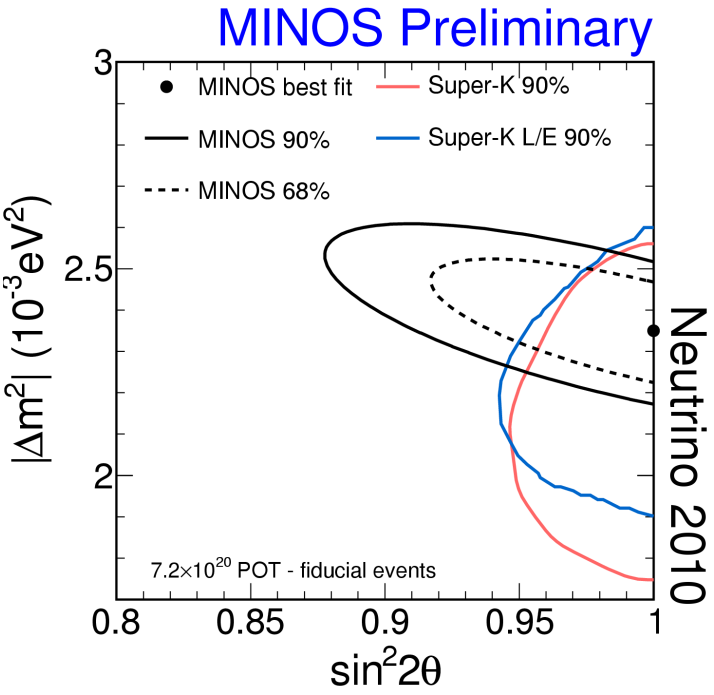

Figure 5: Confidence Interval contours in the fit of the MINOS Far Detector data to the hypothesis of two-flavour oscillations [21]
. The black solid (dashed) curves give the 90% (68%) contours. The best fit point (constrained to lie within the physical region) is $\Delta m^2 = (2.35^{+0.11}_{-0.08}) \times 10^{-3}$ eV^2 and $\sin^2(2\theta) = 1.00$ ($\sin^2(2\theta) > 0.91$ at 90% CL). Also shown are recent preliminary results from the Super-Kamiokande experiment.

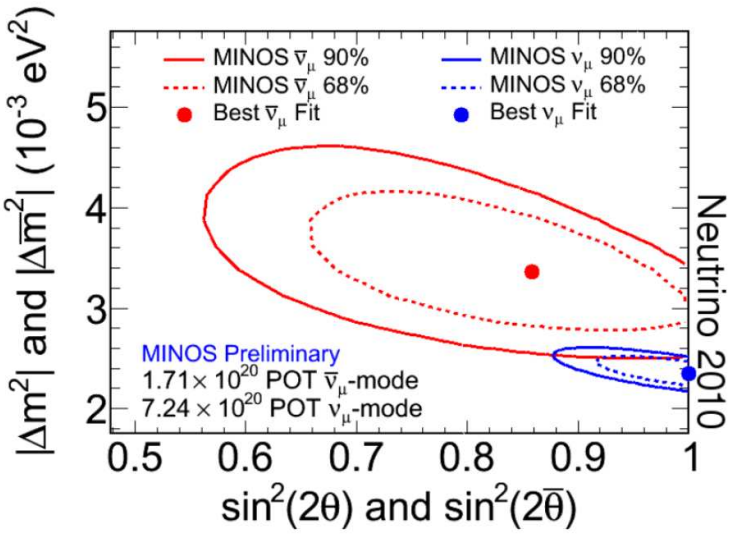

Figure 6: Confidence Interval contours in the fit of the MINOS Far Detector anti-neutrino data (red) to the hypothesis of two-flavour oscillations [21]. The solid (dashed) curves give the 90% (68%) contours. The best fit point is $\Delta m^2 = (3.36\pm0.45\ (\text{stat.})\ \pm0.06\ (\text{syst.})\ )\times10^{-3}\,\text{eV}^2$ and $\sin^2(2\theta) = 0.86\pm0.11$ (stat.) ±0.01 (syst.). Also shown are preliminary contours from the MINOS neutrino analysis.

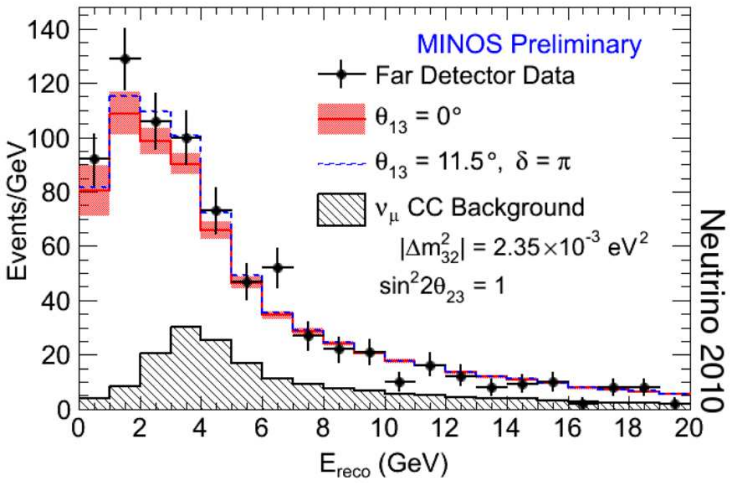

Figure 7: This plot shows the measured rate of neutral-current interactions in the MINOS far detector as a function of reconstructed energy along with the expected rates with and without electron neutrino appearance [21]. The rates for the expectation were determined using the reconstructed energy spectrum from the near detector along with the Monte Carlo simulation of the far detector and the expectations account for the muon neutrino disappearance observed in the charged-current result. The predicted background from charged-current interactions of muon neutrinos at the far detector is also shown. The data is consistent with oscillations only occurring between the active neutrino flavours.

3 The T2K Experiment

The T2K experiment is a long base-line neutrino oscillation experiment, looking for sub-dominant $\nu_\mu \rightarrow \nu_e$ oscillations. An intense ν_μ beam is produced at a purpose built proton synchrotron at the J-PARC facility in Tokai on Japan's East coast. This beam is then directed to a suite of near detectors 280 m from the beginning of the beam where it can be detected and characterised, and is then detected again 295 km away on Japan's West coast at the large water Cherenkov detector 'Super-Kamiokande' (Super-K). The peak neutrino energy is around 600 MeV. Changes in the composition of the beam which signify neutrino oscillations are detected at Super-K.

T2K will aim to understand ν_μ disappearance better in addition to having discovery potential for sub-dominant $\nu_\mu \rightarrow \nu_e$ oscillations.

3.1 T2K Goals

The primary aims of the T2K experiment are as follows:

- to narrow down the current limit on the value of θ_{13} and possibly observe electron neutrino appearance,
- to find whether θ_{23} is maximal, which is crucial to constrain neutrino mass models and
- can investigate *CP* violation in neutrino oscillations. If $\theta_{13} \neq 0$ then this enables *CP* violation and the *CP* violating phase δ from the three flavour oscillation matrix can be investigated.

Two important processes that will be investigated at T2K are the disappearance of ν_μ and the appearance of ν_e from the ν_μ beam produced at J-PARC. The probability for the disappearance of ν_μ is given by:

$$1 - P(\nu_\mu \to \nu_\mu) = 1 - \left(\sin^2 2\theta_{23} \cos^4 2\theta_{13} \sin^2 \left(\frac{1.27 \Delta m^2_{23} (\mathrm{eV}^2)}{\frac{E\,(\mathrm{GeV})}{L\,(\mathrm{km})}} \right) \right), \quad (12)$$

and the probability for the appearance of ν_e is given by:

$$P(\nu_\mu \to \nu_e) = \sin^2 2\theta_{13} \sin^2 2\theta_{23} \sin^2 \left(\frac{1.27 \Delta m^2_{23}\,(\mathrm{eV}^2)}{\frac{E\,(\mathrm{GeV})}{L\,(\mathrm{km})}} \right). \quad (13)$$

Defining the effective mixing angles as:

$$\sin^2 2\theta_{\mu\mu} \equiv \sin^2 2\theta_{23} \cdot \cos^4 2\theta_{13} \quad (14)$$

and

$$\sin^2 2\theta_{\mu e} \equiv \sin^2 2\theta_{13} \cdot \sin^2 2\theta_{23} \quad (15)$$

the probabilities reduce to:

$$P(\nu_\mu \to \nu_\mu) = 1 - \left(\sin^2 2\theta_{\mu\mu} \sin^2 \left(\frac{1.27 \Delta m^2_{23}\,(\mathrm{eV}^2)}{\frac{E\,(\mathrm{GeV})}{L\,(\mathrm{km})}} \right) \right) \quad (16)$$

and

$$P(\nu_\mu \to \nu_e) = \sin^2 2\theta_{\mu e} \sin^2 \left(\frac{1.27 \Delta m^2_{23}\,(\mathrm{eV}^2)}{\frac{E\,(\mathrm{GeV})}{L\,(\mathrm{km})}} \right) \quad (17)$$

As we considered in Section 2.5, ν_μ disappearance experiments have led to constraints on many of these parameters, and since atmospheric neutrino data indicates almost full mixing with $\theta_{23} \simeq \frac{\pi}{4}$ and since θ_{13} is so small, the probabilities further reduce to:

$$P(\nu_\mu \to \nu_\mu) = 1 - \left(\sin^2 2\theta_{23} \sin^2 \left(\frac{1.27 \Delta m^2_{23} \, (\mathrm{eV}^2)}{\frac{E \, (\mathrm{GeV})}{L \, (\mathrm{km})}} \right) \right) \tag{18}$$

$$P(\nu_\mu \to \nu_e) = \frac{1}{2} \sin^2 2\theta_{13} \sin^2 \left(\frac{1.27 \Delta m^2_{23} \, (\mathrm{eV}^2)}{\frac{E \, (\mathrm{GeV})}{L \, (\mathrm{km})}} \right) \tag{19}$$

Hence, to a good approximation, we can see that the disappearance of ν_μ leads to the determination of θ_{23} and Δm^2_{23}, and the appearance measurement can be used to measure θ_{13}. Measurements of ν_μ disappearance have already been made using atmospheric neutrinos at Super-K, K2K and accelerator neutrinos at MINOS, but will be improved by T2K and the appearance of ν_e can be observed for the first time.

3.2 The Physics of T2K

As we have seen in Section 3.1, the primary physics goals of T2K are to: improve the current limits on the value of θ_{13} by discovering ν_e appearance, and to constrain neutrino mass models through investigation of Δm^2_{23} and θ_{23} by measuring ν_μ disappearance.

T2K will improve the current best limit on θ_{13}—as set by the CHOOZ experiment—by an order of magnitude. The CHOOZ excluded region (shaded) and the T2K expected sensitivity (red line) can be seen in Figure 8. To achieve this, T2K needs to have only a 10% systematic error, as can also be seen in Figure 8. T2K will sit along the blue line in the plot looking right, towards the excluded region for θ_{13}.

Figure 9 shows signal charge current quasi-elastic (CCQE) events at Super-K. These are typically single muon or electron events from neutrino interactions in the water, the accompanying proton cannot be observed since it is below

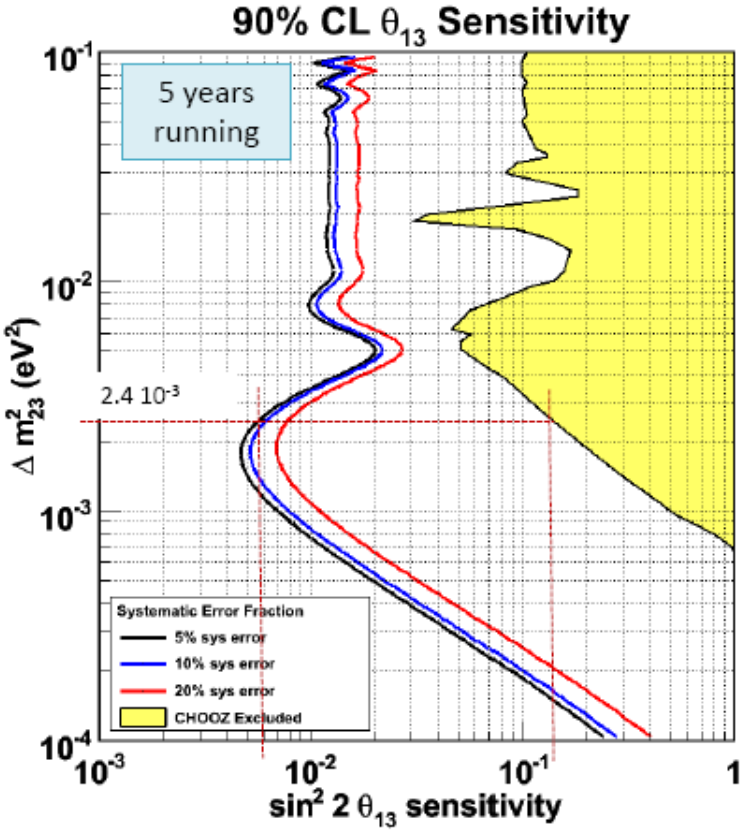

Figure 8: T2K sensitivity to θ_{13} at the 90% confidence level as a function of Δm^2_{23}. The beam is assumed to be running at 750kW for 5 years, using the 22.5 kton fiducial volume SK detector. 5%, 10% and 20% systematic error fractions are plotted. The yellow region has already been excluded to 90% confidence level by the CHOOZ reactor experiment. The following oscillation parameters are assumed: $\sin^2 2\theta_{12} = 0.8704$, $\sin^2 2\theta_{23} = 1.0$, $\Delta m^2_{12} = 7.6 \times 10^{-5}\,\mathrm{eV}^2$, $\delta_{CP} = 0$, normal hierarchy.

the Cherenkov threshold. Such CCQE events are the main signal for T2K as they allow the neutrino energy to be reconstructed (this is described in more detail in Section 3.5).

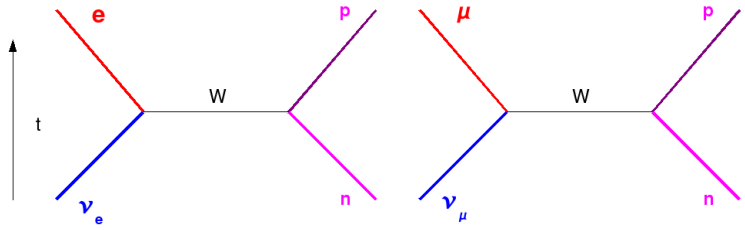

Figure 9: CCQE signal events at T2K.

T2K expects to observe roughly 100 ν_e appearance events after 8×10^{21} protons on target (POT) at 30 GeV, which is around 5 years of data taking (assuming $\sin^2 2\theta_{13} = 0.1$). Approximately 20% of these events will be background events. Such background events can be split fundamentally into two categories, each accounting for 50% of the total background. These are: the intrinsic ν_e contamination of the beam and $NC\pi^0$ events which can be misidentified as electrons from electron neutrinos. For ν_e appearance measurements a common example of this π^0 background can be seen in Figure 10.

Around 1300 ν_μ disappearance events are expected to be observed at T2K for the same exposure. The major backgrounds for ν_μ disappearance measurements are from $NC\pi, CC\pi$ single pion production events that can be misidentified as muons from muon neutrinos, as can be seen from Figure 11.

From Figure 12 we can see that since the value of $\sin^2 2\theta_{23}$ defines the probability of oscillation, it is essential to focus our detection capabilities at the oscillation maximum and also that at this oscillation maximum the expected signal at T2K is far greater than the background over 5 years data taking or 8×10^{21} POT at 30 GeV. This is achieved through the use of an off-axis beam

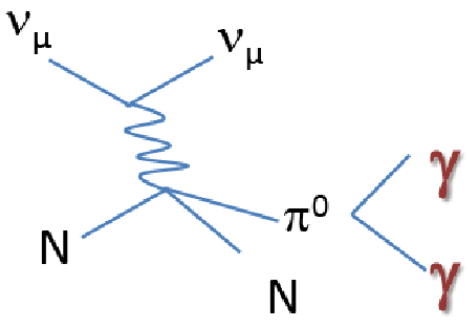

Figure 10: Example $NC\pi^0$ background event to the ν_e appearance measurement.

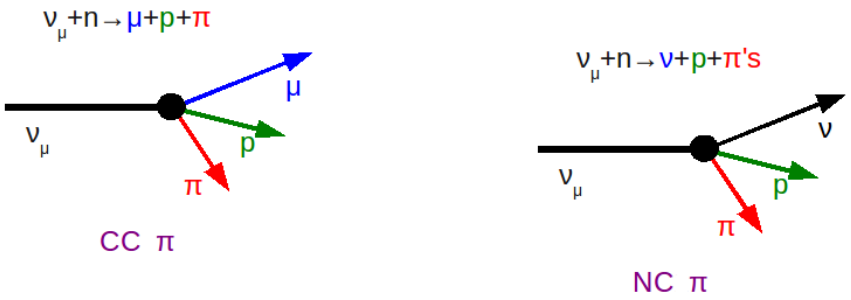

Figure 11: Example $NC\pi$ (left) and $CC\pi$ (right) background events to the ν_μ disappearance measurement. The dominant background to ν_μ disappearance is from CC-1π events.

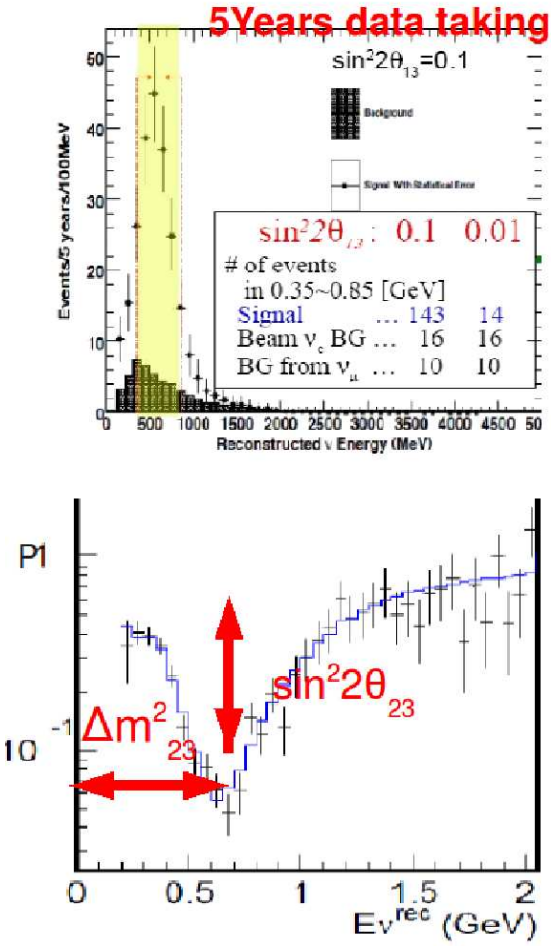

Figure 12: Signal versus background for the ν_e appearance measurement at T2K over 8×10^{21} POT at 30 GeV at the oscillation maxima and the dependence of $\sin^2 2\theta_{23}$ on the probability of oscillation, showing the importance of observing the oscillation at its maximum [22].

geometry of 2.5°.

The T2K neutrino beam is essential to the success of the experiment. It is necessary for the flux intensity to be greatest at an energy of 600–700 MeV (the oscillation maximum) this is calculated from the known oscillation parameters and the T2K baseline of 295 km. We must also minimise the high energy tail and the electron neutrino contamination in the beam.

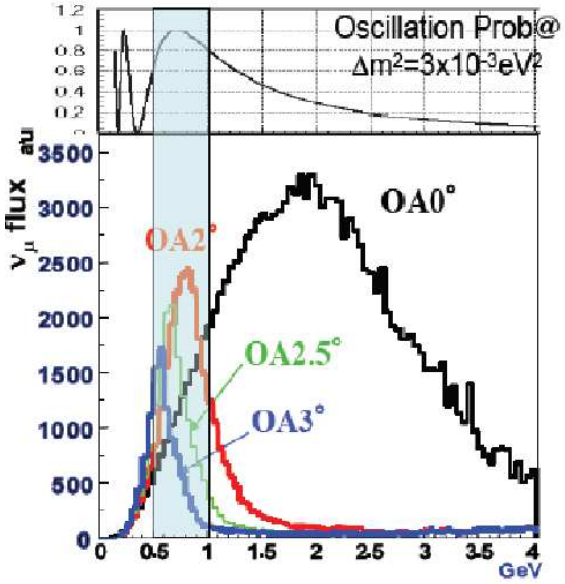

Figure 13: The neutrino flux against the neutrino energy for beam angles between 0° and 3°. The first oscillation maximum is highlighted to show the peak of the spectrum. We can see that a beam at 2.5° is the most highly focused around the oscillation maximum, that the flux is highly peaked and that there is very little high energy tail.

The 2.5° off-axis geometry provides a (quasi) mono-energetic beam tuned to the first oscillation maximum (600–700 MeV), increasing the flux and drastically cutting the high energy tail responsible for inelastic interactions which are background to the CCQE events (see Figure 13). The ν_e contamination of the beam is also minimised around the peak, producing a beam composition of around 95% ν_μ, 4% $\overline{\nu}_\mu$ and less than 1% ν_e.

T2K will be the most sensitive experiment to date to measure the unknown parameters of neutrino oscillations. The experimental set-up from the beam to the detectors is explained in the next section.

3.3 Experimental Overview of the T2K Experiment

T2K produces an intense ν_μ beam at J-PARC—in Tokai—where it is detected and characterised 280 m from its start and directed 295 km to the far detector Super-Kamiokande, which will detect the oscillated beam. At J-PARC, a high power proton synchrotron is used to create an intense—0.75 MW—proton beam, which is then collided with a graphite target to produce charged (mainly positively) pions. These are then selected and focused into a narrow beam and directed through a helium filled decay volume, which results in a beam of muon neutrinos. Any remaining protons, pions and muons will be captured by the beam dump.

An off-axis beam geometry at an angle of 2.5° is used (see Section 3.2), thereby creating a narrow beam with very little high energy tail (which would create a lot of background), hence increasing the flux of neutrinos at the oscillation maximum, giving a more sharply peaked energy spectrum and reducing the intrinsic beam ν_e contamination. There are two near detectors (INGRID on-axis and ND280 off-axis) 280 metres from the start of the beam at J-PARC, which is used to characterise the beam near its origin. The partly oscillated beam is finally detected by the far water Cherenkov detector 'Super-Kamiokande'.

The ND280 off-axis detector and in particular the ECals are one of the primary concern of the UK group. The three sets of ECals are the P0D ECal (PECal) and tracker ECals (TECal)—surrounding the inner detector of the

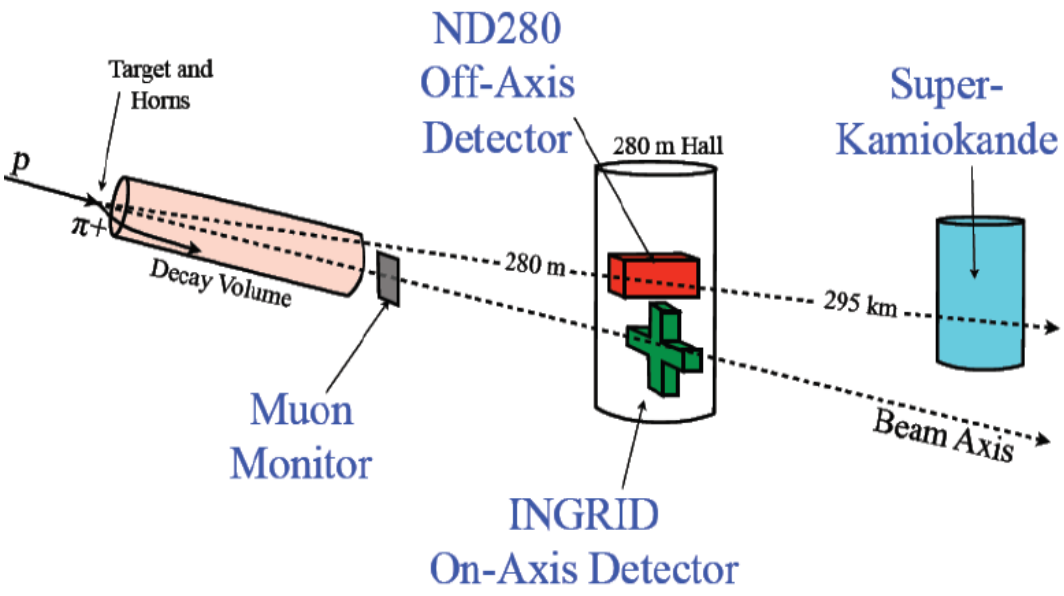

Figure 14: An overview of the T2K experiment, showing the beam and the detectors involved.

ND280, and the downstream ECal (DSECal)—acting as an end cap at the downstream end of ND280. The primary function of the ECals is to identify muons and electrons and hence determine the ν_e contamination of the beam, and to measure the photon pairs from single π^0's produced by neutrino interactions in the inner detectors. A schematic of this set-up can be seen in Figure 14.

The proton synchrotron at J-PARC uses dual purpose (dipole and quadrupole) super-conducting magnets to bend the proton beam in a small radius (necessary due to the lack of space at J-PARC). The beam is then directed to the target station and collides with a helium cooled graphite target to produce charged pions of equivalent energy to that of the incoming protons. These pions are then focused (by a horn) and enter a 100 m helium filled decay volume where a large proportion will decay into muon neutrinos. Any remaining protons and pions will be captured by the beam dump. The direction of the

beam will be determined on a spill-by-spill basis (one spill is equal to six pulses of the beam—which are accelerated together in the synchrotron—and occurs every 3.5 s) by muon sensors that are positioned behind the beam dump. The ν_μ beam created is the highest power pulsed neutrino beam in existence, it is currently producing a 90 kW beam of 3.2×10^{19} protons on target and will increase to 0.75 MW after 5 years. This will create the maximum possible neutrino flux and increase the statistical sensitivity of T2K, which is imperative to an experiment which is looking for sub-dominant oscillations. An 'off-axis beam geometry' will be used as previously described.

There are many experimental issues which need to be considered in order to achieve such high precision measurements as required at T2K. First, in order to measure ν_μ disappearance accurately, the complete "unoscillated" beam spectrum must be known. To achieve this the beam will be characterised at the near detector and any near/far corrections to the oscillation spectrum will be taken into account. The energy resolution for muons in the near and far detectors must also be known, in addition to the non quasi-elastic contamination of the measured muon spectrum. When measuring electron neutrino appearance, the primary experimental concerns are the high level of background and the statistical limitations on all but the largest currently allowed values of θ_{13} (this can be minimised by maximising the neutrino flux). The near detectors are therefore also required to measure energy/angle distributions of NC events in order that the expected flux of such events at Super-Kamiokande can be estimated.

3.4 The T2K Near Detector - ND280

3.4.1 The INGRID Interactive Neutrino Grid

The Interactive Neutrino Grid (INGRID) on-axis neutrino monitor sits in the on-axis position in the beam line to detect the exact position of the horn focused neutrino beam (see Figure 15). The off-axis angle must be monitored to $<$ 1mrad (i.e. 2% shift in the neutrino peak energy). INGRID is sensitive to these tiny variations in the beam position and enables T2K to determine fluctuations around the 2.5° off-axis detection position—which are due to tiny fluctuations in the beam position—to the required accuracy of $<$ 1mrad. INGRID is able to make at least daily and often hourly calculations of the beam position to help to minimise the systematic errors of T2K.

INGRID has 16 modules arranged in a cross shape, with each module made up of 11 layers of scintillator interleaved with iron plates, as can be seen from Figure 16. The full INGRID detector was installed in the ND280 pit and commissioned in summer 2009 and was the first of the near detectors to observe a neutrino candidate event, shown in Figure 17.

3.4.2 The ND280, Off-axis Near Detector

The ND280 off-axis detector consists of a suite of eight sub-detectors, located in the same pit as the INGRID, but in the off-axis position - in line with Super-Kamiokande. The remaining seven detectors are the Pi0 detector (P0D), the Time Projection Chambers (TPCs) and Fine Grain Detectors (FGDs), which collectively are known as the 'tracker' or 'barrel' and the Tracker, P0D and Downstream Electromagnetic Calorimeters (TECals, PECals and DSECals, respectively). These detectors are then surrounded by a magnet—referred to as the UA1 magnet, as it was previously used in the UA1 experiment [23],

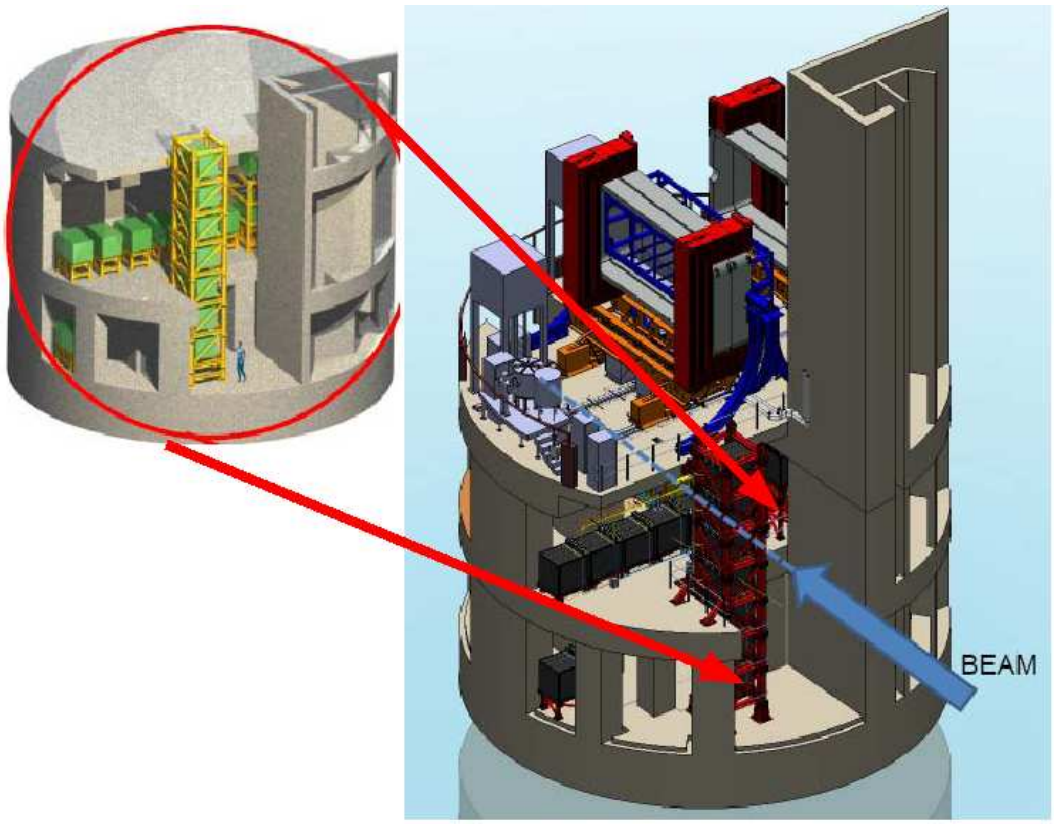

Figure 15: Schematic showing the on-axis position of the INGRID interactive neutrino monitor, in position in the ND280 pit.

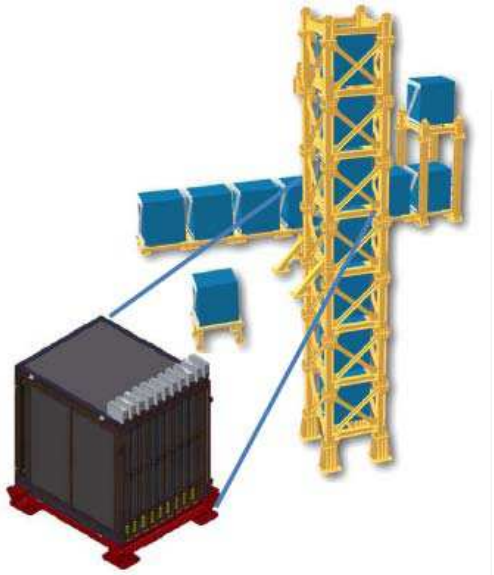

Figure 16: The on-axis INGRID interactive neutrino monitor. The 16 modules arranged into a cross and the 11 scintillator and iron layers of each module can be seen.

which produces a 0.2 T magnetic field and has gaps in which the Side Muon Range Detector (SMRD) is fitted. A pictorial representation of the ND280 off-axis detector is shown in Figure 18.

In order to achieve the target precision which we require on θ_{23}, and Δm^2_{23}, T2K demands an uncertainty on the non-QE/QE ratio which is less than 10% and for this to be accomplished we need ND280 to have excellent particle identification (PID) capabilities and minimal systematic errors. The cross section measurements made at the near detector are essential to measure the backgrounds at Super-K, i.e. NCπ, CCπ for ν_μ disappearance and $NC\pi^0$ for ν_e appearance. In addition ND280 will provide the most extensive measurements of sub-GeV neutrino cross sections on carbon and oxygen to date. ND280 can identify charged particles: pions, muons, electrons and protons, and has the ability to detect photons—which can help identify the background from π^0's[10, 11]—and can help to determine the ν_e contamination of the beam.

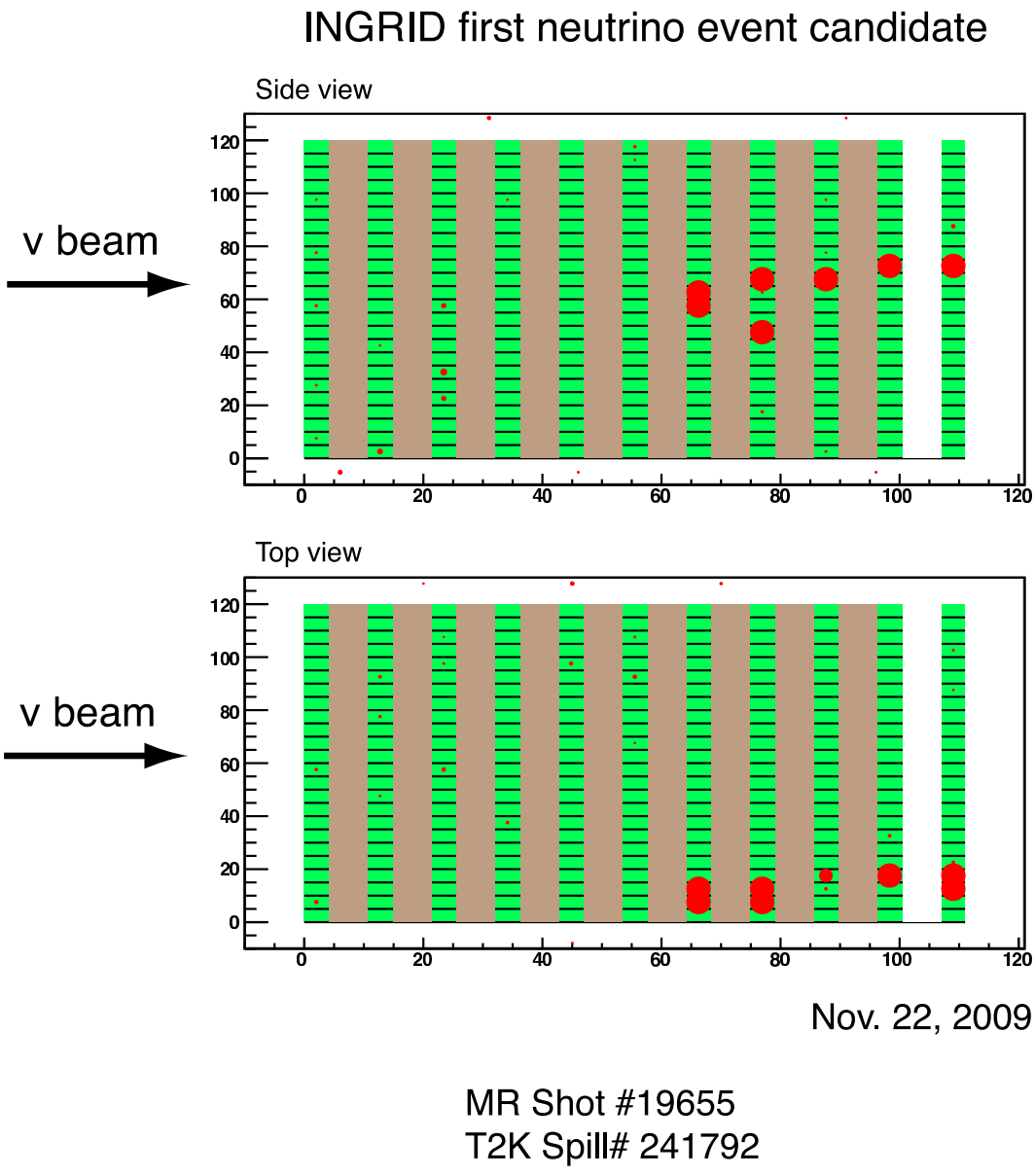

Figure 17: An event display of the first T2K neutrino event candidate, observed by the INGRID detector at 20:25 on Nov. 22nd 2009.

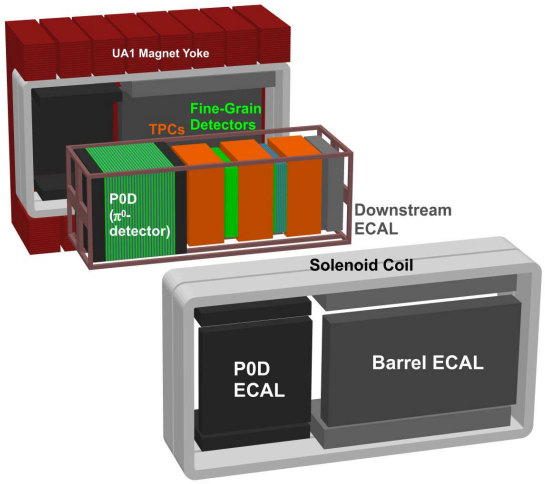

Figure 18: The ND280 suite of detectors showing the Pi0 detector (P0D), the Time Projection Chambers (TPCs) and Fine Grain Detectors (FGDs), which collectively are known as the tracker or barrel, the Tracker, P0D and Downstream Electromagnetic Calorimeters (TECals, PECals and DSECals respectively) and the Side Muon Range Detector (SMRD)—positioned in gaps in the UA1 magnet.

The full details of the ND280 off-axis detectors can be found below.

The far detector—Super-Kamiokande (Super-K)—is a 50,000 ton pure water detector. Located 1000 m underground in the Kamioka mine, it is the largest subterranean detector at $\sim 50\,\mathrm{m} \times 40\,\mathrm{m} \times 40\,\mathrm{m}$. It is situated 295 km from the J-PARC facility and provides many advantages for the T2K experiment. It has operated successfully for many years and has a well understood energy resolution and response to electrons, pions and muons at T2K's energies, making it excellent at distinguishing between ν_μ and ν_e and the background π^0 events. Further information can be found in Section 3.5.

3.4.3 The Pi0 Detector - P0D of ND280

The rate of neutral current π^0 production will be measured by the P0D which is located in the central upstream section of the ND280 off-axis detector. It con-

sists of 40 x-y brass and scintillator tracking planes interspersed with water volumes for measuring the reaction rate in Oxygen (mass ratio—Carbon:Oxygen 1.8:0.9ton). The P0D will have sections of water target; since Super-K is a water Cherenkov detector, it is imperative to know how many events will appear as single ring events and hence appear in the CCQE sample in water. The scintillator is made up of triangular scintillator bars arranged top to bottom to make a rectangular sheet, read out by wavelength shifting (WLS) fibres threaded through the centre of the bars (see Figure 19). The P0D was installed and commissioned in late 2009 (see Figure 20).

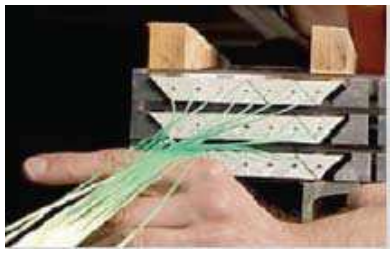

Figure 19: The layer structure to the P0D detector showing the triangular scintillator bars, tier arrangement and the readout WLS fibres.

3.4.4 The Tracker - Time Projection Chamber(TPC) and Fine Grain Detector (FGD) of ND280

The tracker is located in the central downstream section of the detector and consists of the TPCs and FGDs. They are optimised to measure charged particle momenta and to perform particle identification (PID) particularly of muons and pions produced by charged current interactions. There are three TPCs and two FGDs, which will give the most accurate 3-momentum of charged particles produced in charge current interactions in the FGD detector, and they will identify pions, muons and electrons and determine the sign of such charged particles. The TPC will determine the muon energy spectrum from CCQE

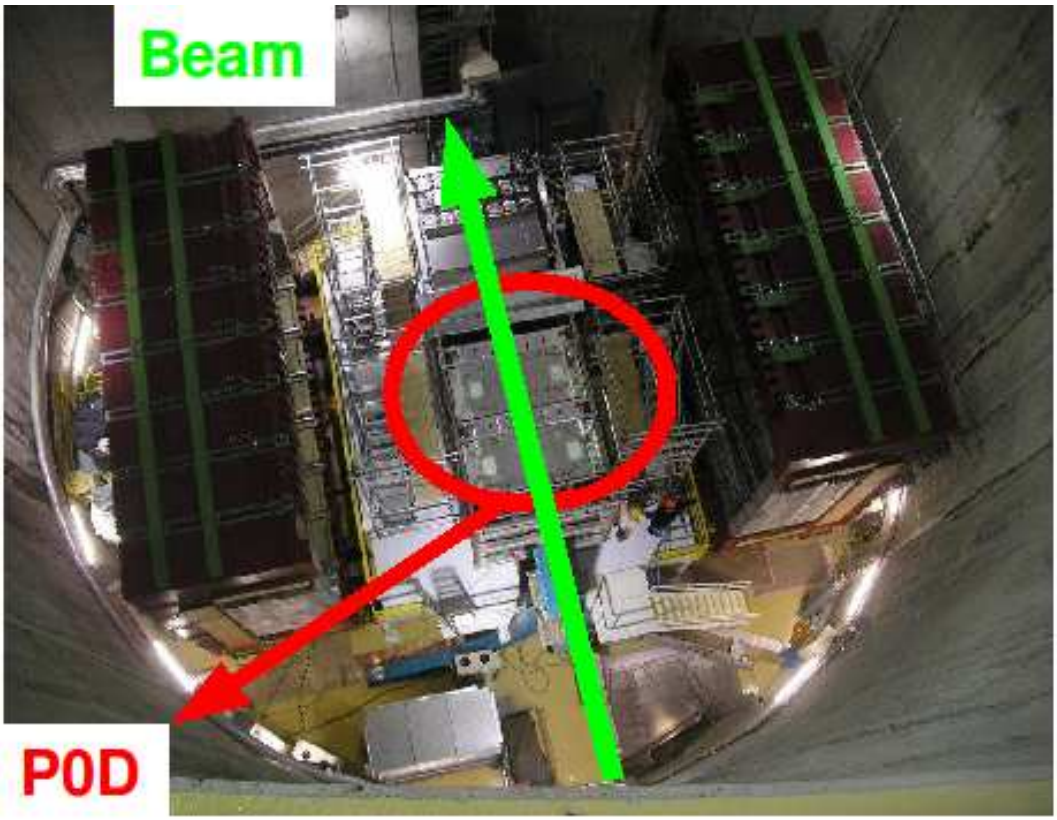

Figure 20: The P0D detector in position in the ND280 pit, viewed from above.

events in the FGDs in addition to the non-QE contamination of these events, needed to improve the disappearance measurement. The TPC is the first detector to use large-scale implementation of bulk micromegas detectors [24]—(32 modules, 124K channels) (see Figure 21), to give high resolution tracking. A charge/momentum measurement gives: σ_p/p of approximately 10 % at the 5 σ level.

Figure 21: The TPC showing the large scale implementation of bulk micromegas.

FGD 1 has 1cm^2 scintillator bars arranged in alternating layers of parallel bars, each layer perpendicular to the next, fine enough to measure recoil photons. FGD 2 has both scintillator bars and water—to aid the cross section measurements at Super-K. The FGD weighs 1.3 tons. The FGDs and TPCs were installed in the ND280 pit between October and January 2009-2010.

These detectors are held inside the basket (a metal frame which holds the inner detectors) and are surrounded on five sides by the 13 modules of the ECal.

3.4.5 The Side Muon Range Detector (SMRD) of ND280

Surrounding the ECal, P0D and Tracker (TPC and FGD) is the UA1 magnet producing a 0.2 Tesla magnetic field. The SMRD is made up of scintillator planes inserted in the gaps of the magnet yoke. Each scintillator plane is read out by a WLS fibre, which can be seen in Figures 22 and 23. It will detect muons in addition to identifying muons originating outside the detector. The SMRD was installed and commissioned in October 2009.

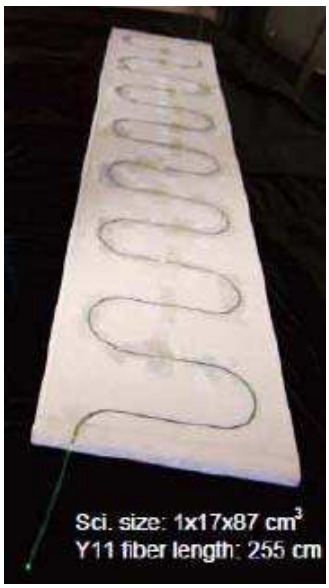

Figure 22: An SMRD plane showing the WLS readout.

3.4.6 The Electromagnetic Calorimeters and in particular the Downstream Electromagnetic Calorimeter of ND280

The ECal consists of 13 sub-modules; the Tracker ECal (TECal), P0D ECal (PECal) surround the tracker and P0D respectively and the DSECal. The TECal and PECal consist of 6 modules each; the left and right - top, side and bottom modules, whilst the DSECal is one module and sits downstream of the tracker. The TECals and PECals surround the tracker on four sides but are

Figure 23: The SMRD being fitted within the gaps of the UA1 magnet.

split along the beam line since the magnet has to open to allow maintenance, see Figure 24.

The functions of the ECal are to measure the energy of electrons and photons from hit and charge information to distinguish muons and electrons. The energy measurement can be used in conjunction with the TPCs to perform an energy over momentum—E/p measurement and hence determine the electron neutrino contamination of the beam, in addition to measuring single π^0's produced by neutrino interactions in the FGDs. The ECal is one of the main contribution of the UK group to the near detector and hence it is the focus of my work and described in further detail in the following text.

The six modules of the TECal, surrounding the tracker on 4 sides, the left top, side and bottom TECals and the right top, side and bottom TECals. The top and bottom modules are 3.84 m x 1.52 m x 0.5 m, whilst the side modules are 3.84 m x 2.28 m x 0.5 m. All modules are made up of 4 cm x 1 cm plastic scintillator bars with a small hole through the centre of each, through which

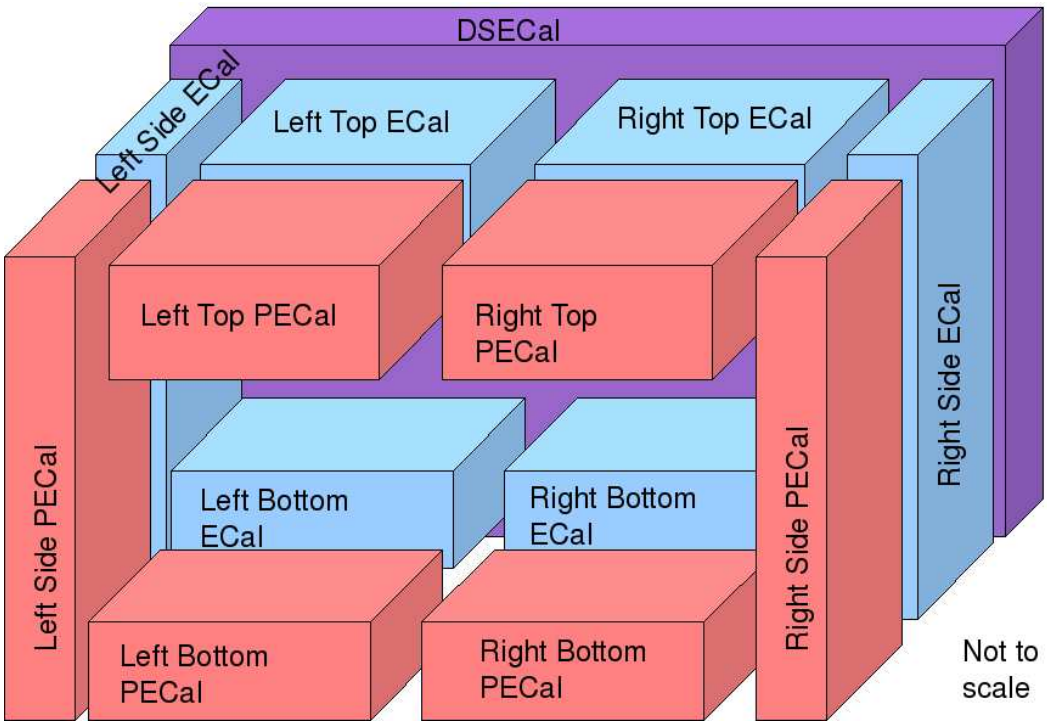

Figure 24: A diagram to show the orientation of the TECal, PECal and DSECal modules that surround the tracker and P0D.

a WLS fibre is threaded (see Figure 25).

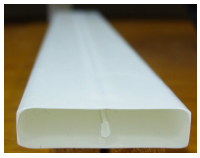

Figure 25: One of the 4 cm x 1 cm scintillator bars of the TECal and DSECal modules, the bar is readout by a WLS fibre which has been threaded through the hole in the centre of the bar.

The bars are organised in layers, and in each layer the bars of that layer are perpendicular to the next. Every alternate layer has double ended readout (an MPPC attached to each end of the fibre) and single ended readout, with an MPPC at only one end of the bar/fibre with a reflective mirror at the other end of the bar. The top and bottom modules have 30 layers either 96 or 38 bars long, depending upon the orientation of the layer, meaning there are 15 layers 3.84 m in length and 15 layers 1.52 m in length. The side modules also have 30 layers 96 or 58 bars in length according to the orientation of the layer. A 1.75 mm thick layer of lead sits between each layer of scintillator bars—for all modules—and increases the chance that electron and photon events shower in the ECals. The performance of each of the bars and layers is tested as each is built, using a purpose built 2D scanner with a 3 mCi ^{137}Cs source (see Figure 26). All of the TECal modules will be installed in the pit and commissioned during the summer of 2010.

The PECal is designed to detect photons and minimally ionising particles (MIPs) escaping from the P0D. There are 6 PECal modules surrounding the P0D, again the left and right, top, bottom and side modules. Each of the PECal modules consists of 6 layers. The top and bottom PECal modules consist of 38 bars per layer, again, each is organised perpendicular to the next; the total dimensions are 2.34 m x 1.4 m x 0.5 m. The side PECal modules are

arranged in 6 layers of 69 bars per layer, each layer arranged perpendicular to the next to give side PECal modules of dimension 2.34 m x 2.6 m x 0.5 m. The layers of all PECal modules are separated by 4mm thick lead sheets and have single ended readout, with one MPPC at the most downstream end of the bar. The 6 PECal modules will be installed in summer 2010.

The DSECal, which was the first of the modules to be built, is 2 m × 2 m × 0.5 m and sits as an endcap to the ND280 detector downstream of the neutrino beam. It is made up of 1700 2 m long scintillator bars, arranged in layers 50 bars wide. Each layer has an alternating x-y orientation as for the TECal, and there are 34 layers in total. The building procedure was the same for all ECal modules and is explained here for the DSECal. The 50 bars which make up a layer are arranged side by side and glued together using a well understood Araldite epoxy adhesive which does not affect the detector performance. In Figure 27 the process of building the layer in this way can be seen.

Figure 26: The 2D scanner in action testing one of the layers of the DSECal, sitting inside the bulkhead.

A sheet of 1 mm thick lead is then attached to the top of the layer using the same Araldite epoxy adhesive. The lead is in fact in 2 sheets 1 m × 2 m in area, as it is necessary that the lead is as flat as possible and it is impossible to

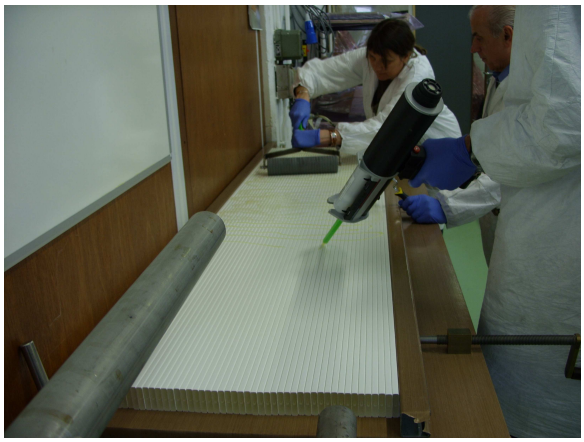

Figure 27: One of the 2m x 2m layers of the DSECal being constructed, the bars are laid out and the glue applied to the ends so that they can be stuck in place side by side.

produce such large sheets without significant skewing, due to the nature of the manufacturing process which produces these thin sheets. The lead is applied to the layer using a vacuum pump lifter to ensure that it remains flat and the complete layer is left to dry for around 8 hours. The purpose of the lead is to increase the amount of interactions from beam particles, thereby maximising the detectors sensitivity to the composition of the beam. The first completed layer with the lead attached can be seen in Figure 28.

Figure 28: The first completed layer of the DSECal.

Each completed layer is placed on top of the next at an orientation of 90°, inside the bulk head (a metal box which holds each of the layers in place and to which the multi-pixel photon counters and readout electronics are attached). Upon the insertion of each new layer, the layer is tested by a 2D scanner (built at Queen Mary University of London), which positions a 3 mCu ^{137}Cs source 1 cm from the layer at 5 cm × 5 cm intervals to ensure that all components of the layer are behaving as they should (see Figure 26). The light output in photoelectrons (pe) as a function of the position of the source along the bar is plotted and examined (see Figure 29).

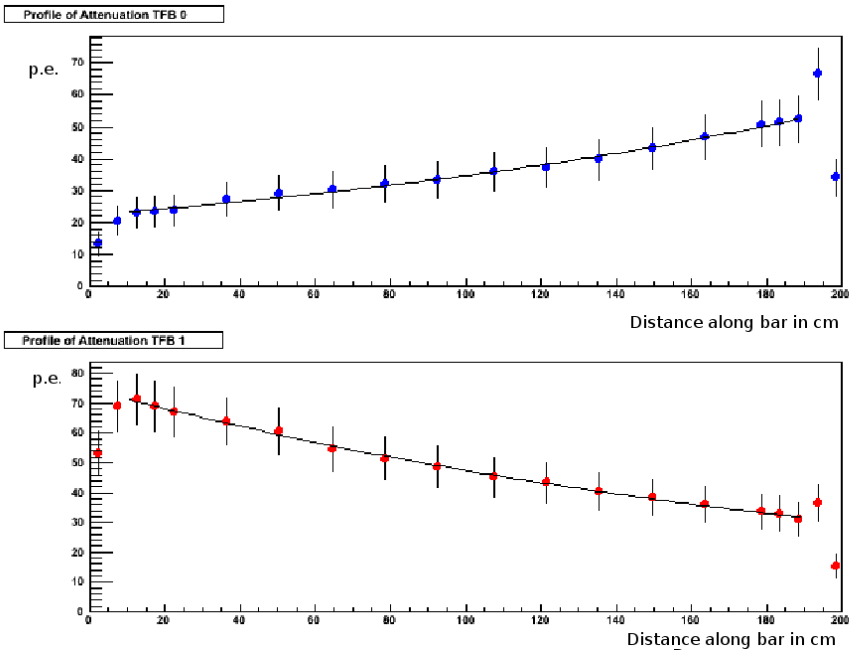

Figure 29: Attenuation plot with distance along the bar on x and light yield in pe on y, for layer 15 bar 1 using 2D scan data. The two plots are for each of the MPPC readouts of the same bar, hence the gradients are in opposing directions. NB, this does not constitute an attenuation correction for the bars, as the method of data taking and the source are not representative of the conditions at T2K. It is simply to test that the layer is behaving within expectations. Also the errors are highly correlated and so the error bar appear small.

The DSECal was the first of the ECal modules to be built, commissioned

and installed in the ND280 pit (see Figure 30). It underwent extensive testing, having three rounds of commissioning, cosmic tests and test beam time, in order to understand the detector fully. Due to funding constraints it is the only module which can be tested in this thorough way, but since all of the ECal modules are similar, the lessons learnt with the DSECal can be transferred to the other ECal modules. This extensive process of testing and calibration has been the focus of much of my work and is described in detail in the following chapters.

Figure 30: The completed DSECal being put onto the crane at J-PARC, ready to be installed in the pit.

The geometry and dimensions of all 13 ECal modules can be seen in Table 2.

3.5 The T2K Far Detector—Super-Kamiokande

T2K's far detector sits 295 km from the start of the beam to detect changes in the beam's make up due to neutrino oscillations. It is a 50 kton ultra-pure water Cherenkov detector, situated 1000 m underground in the Kamioka mine on the West coast of Japan. It consists of a cylindrical stainless steel tank

Region	Modules	Size(m^2)	Layers	Bars/Layer	Lead(mm)
Downstream	1	2 x 2 x 0.5	34	50	1.75
Barrel					
Top/Bottom	4	3.84 x 1.52 x 0.5	30	96/38	1.75
Side	4	3.84 x 2.28 x 0.5	30	96/58	1.75
P0D					
Top/Bottom	4	2.34 x 1.4 x 0.5	6	38	4
Side	2	2.34 x 2.6 x 0.5	6	69	4

Table 2: The geometry of each of the modules of the ECal.

41.4 m (135.8 ft) tall and 39.3 m (128.9 ft) in diameter. The tank's volume is divided by a stainless steel superstructure into an inner detector (ID) region 33.8 m (110.9 ft) in diameter and 36.2 m (118.8 ft) in height and an outer detector (OD) holding the remaining volume. The inner and outer detectors are optically separated by a black-sheet barrier. See Figure 31 for a pictorial representation of the detector.

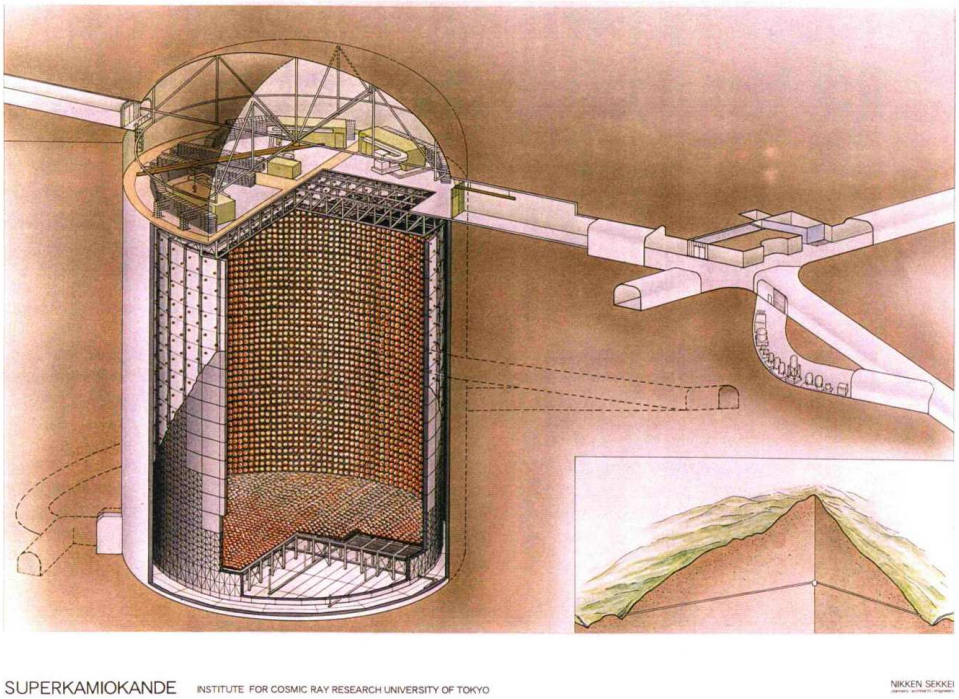

Figure 31: The Super-Kamiokande detector.

Neutrinos are detected as they interact with the electrons or nuclei in the water, producing charged particles in the form of their leptonic counterparts. These particles travel faster than the speed of light in water (which is 1.3 times slower than in air) creating a cone of photons emitted along the path of the particle. This process is known as Cherenkov radiation. These rings are then detected in the inner detector by 11,146 20 inch (50.8 cm) photomultiplier tubes and in the outer detector by 1885 8 inch (20.3 cm) PMTs. A view inside the Super-K detector is shown in Figure 32.

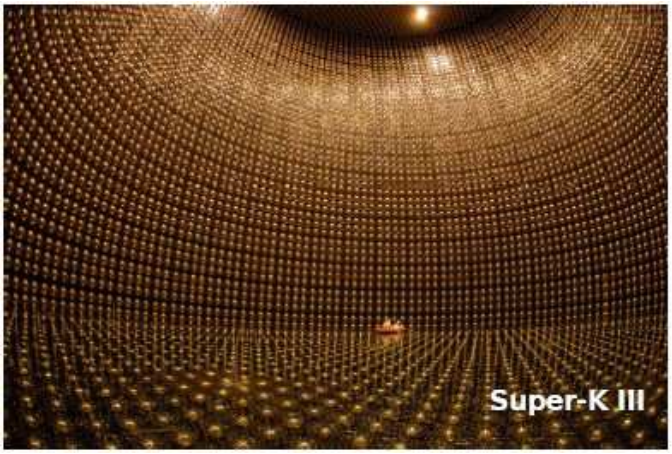

Figure 32: The inside of the Super-Kamiokande detector, showing the photomultiplier tubes inside the inner detector and the water level very low. A boat with people inspecting the PMTs can be seen.

Super-Kamiokande can distinguish between muon and electron neutrinos through the nature of the rings which they create. When a muon neutrino interacts it produces a single muon, which then produces concentric rings of photons as it travels through the water, producing a clear "sharp" ring pattern on the wall of Super-Kamiokande. An electron neutrino interaction, on the other hand, produces an electron which subsequently showers to produce more electrons, all of which then produce Cherenkov showers which overlap to produce a fuzzy ring on the wall of the detector. This process is shown

pictorially in Figure 33.

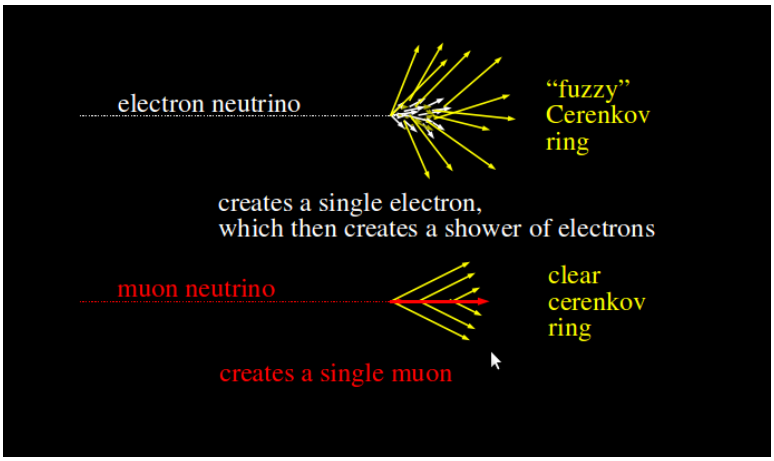

Figure 33: Cherenkov radiation—depicted in yellow—is emitted by an electron—in white—which showers to produce further electrons, which each produce Cherenkov light. The muon—in red—produces a clean ring of Cherenkov light.

The position, orientation and direction of the rings leeds us to determine that the signal in question is from the neutrino beam and the shape of the rings allows us to count the number of muon and electron neutrinos which have reached Super-Kamiokande, thus determining those which have disappeared and those which have appeared. In Figure 34, we can see an example comparison between the electron and muon neutrino rings. The ring on the left is considerably more fuzzy as it was created by an electron neutrino, whilst the ring on the right (that of a ν_μ) is significantly clearer.

Super-Kamiokande has been operated successfully for many years, but underwent significant upgrades to its electronics in the summer of 2008. Among other improvements, we now have stable and dead-time-less data acquisition (DAQ), thereby improving the tagging efficiency of decay electrons. The software has also been upgraded in light of the new DAQ in preparation for data taking at the T2K experiment.

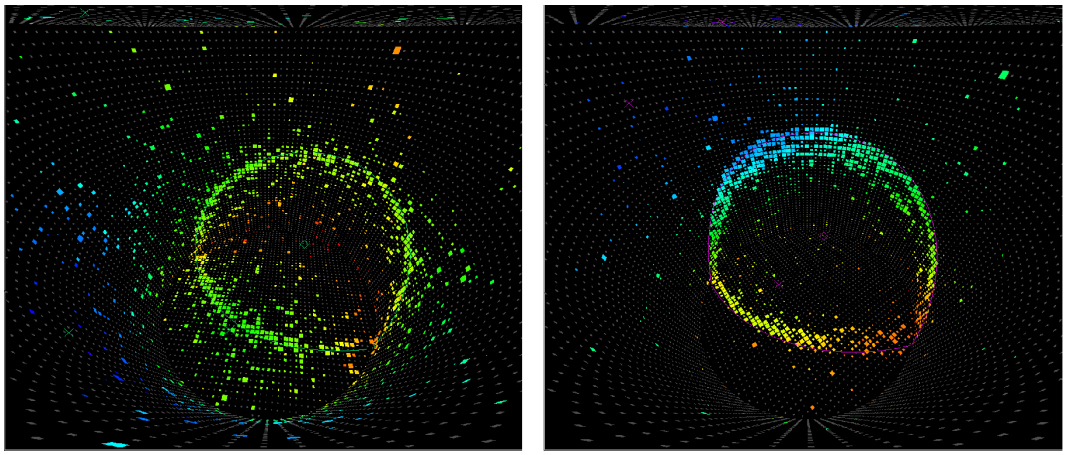

Figure 34: Cherenkov rings produced by neutrinos passing through the water at Super-Kamiokande. The ring on the left has a fuzzy ring made by an electron neutrino interacting in the water to produce an electron which then showers to produce further electrons, each of which produces a ring of Cherenkov light. These overlapping rings can be seen in the event display. The ring pattern on the right was created by a muon neutrino interacting in the water to produce a single muon,, small in size which then produces a relatively clean ring.

4 The Multi Pixel Photon Counters (MPPCs) of ND280

Photomultipliers—and more recently photon counters—are an essential part of many particle physics experiments. They are particularly sensitive to low fluxes and even single photons, and through their combination of reasonably low noise and high gain, they can be used for particle identification of some of the most illusive particles.

ND280 does not use traditional photomultiplier tubes (PMT's) since they are affected by magnetic fields and so instead, it uses multi-pixel photon counters or 'MPPCs' which were designed specifically for the T2K experiment and manufactured by Hamamatsu Photonics in Japan (see Figure 35).

These MPPCs are a type of silicon photomultiplier (the family of Si-

Figure 35: Hamamatsu multi-pixel photon counter. The grey central square is the 1.3mm^2 667 pixels and the MPPC is read out through the two pins.

PM's [25]) consisting of 667 avalanche photodiode (APD) [26] pixels of $50 \times 50\mu\,\mathrm{m}^2$, in size, arranged in a 1.3 mm square and coated in ceramic. Each APD pixel has the ability to output a pulse signal upon the detection of a single photon. The APD operates in Geiger mode with an applied voltage of a few volts above the breakdown voltage (V_{bd}). A Geiger avalanche is induced upon the production of a photoelectron and is then quenched by a resistor integral to each APD. The output charge for each APD are independent of the quantity of photoelectrons produced within the pixel, and can be written as:

$$Q = C(V - V_{bd}) \tag{20}$$

where V is the applied voltage and C is the pixel capacitance. The number of pixels which underwent a Geiger avalanche is proportional to the number of injected photons, when the number of photons is small compared with the number of pixels, thereby affording the MPPC excellent photon counting efficiency. The output given by the MPPC as a whole is the sum of the outputs of all of the APD pixels.

These devices are ideal for the conditions at the T2K off-axis near detector site. They can operate at room temperature and are unaffected by magnetic fields such as the 0.2 T field produced by the UA1 magnet surrounding ND280.

They have the ability to detect single photons and can operate at a low bias voltage below 100 V (at ND280 they will work under an operating voltage of typically 70 V), they produce high gain and unrivalled time resolution and are also low cost. Their photon detection efficiency at 550 nm from the light source is $> 15\%$, the dark noise rate is recorded to be < 1.35 Mcps for a threshold of 0.5 photoelectrons (pe) and < 0.135 Mcps for a threshold of 1.2 pe at 25°C, which is acceptable for T2K. The small size of each MPPC and their ability to be read out by simple circuits make them ideal for the needs of the ND280 sub-detectors. T2K will use around 60,000 MPPCs and will be the first experiment to use MPPCs on such a large scale. Scintillation signals from particles traversing the detectors are read out by the MPPCs via 1 mm diameter Kuraray Y11(200)MS wavelength shifting fibres [27].

The specifications of the Hamamatsu MPPCs make them ideal for the ND280 sub-detectors. It is essential that they are well tested and their quality assured, so to this end, we performed extensive testing of the devices which are used in the ECals; the procedures followed and the results obtained can be found in Section 4.2 below.

4.1 The ND280 Sub Detectors Using MPPCs—In Particular the ECal and DSECal

The Hamamatsu MPPCs specifically designed for use in the T2K experiment are used in both the INGRID on-axis detector and many of the sub-detectors of ND280, the SMRD, P0D, FGD and the P0D, tracker and ECal modules. The ECals were built by the UK T2K collaboration and as such the MPPCs used in the 13 ECal detector modules were assembled and tested in the UK. The 50 bars of each of the 34 layers of the DSECal (1700 bars total) have

MPPC readouts at each end (3400 MPPCs are used in total). The 6 barrel ECal modules have alternating double and single ended bar readouts—with the longer bars running parallel to the tracker having double ended readout and the shorter bars running perpendicular having single ended readout—at the end furthest from the tracker, and single ended readout in the bottom-most ends of the perpendicular bars of the side modules. The 6 P0D ECal modules have single ended readout with the MPPC affixed at the downstream end of all of the bars, which run along the beam axis.

The MPPCs need to be assembled into a setup which can be installed into the relevant ECal detector. This assembly is as follows: first a small sponge is attached to the back face of the MPPC to enable it to be safely and securely inserted into a small tubular grey plastic shroud with the face of the MPPC inside the shroud and the readout pins protruding through small holes in its closed end. The open end of this shroud will be connected to the WLS fibres protruding from the centre of the scintillator bars (or planes in the case of the SMRD) of the detector in use, forming a light tight connection, enabling the photons carried through the WLS to be detected by the MPPC. The protruding pins of the MPPC are then connected to a simple printed circuit board (PCB) with a coaxial cable connected to it which carries the signal from the MPPC to the electronics readout boards. To protect and track the assembled MPPC units, a larger all-encompassing shroud is fitted around the whole setup and a bar code with the MPPCs' unique manufacturer's number is attached (see Figure 36). Once the post-assembly testing and quality assurance (QA) is complete, the coaxial cables are also fitted with labels at both ends, carrying the MPPC manufacturer's number and the position in the detector in which it will be used.

Figure 36: A fully assembled MPPC. The outer protective shroud bearing the unique manufacturer's number and bar-code of the MPPC can be seen on the left. The two pins of the MPPC protruding from the smaller shroud can be seen in the centre of the frame connected to the PCB. The coaxial cable connecting the MPPC to the electronics readout boards is connected to the PCB.

The front end readout electronics for the MPPCs needs to be within the magnet for practical reasons and must therefore be able to operate well in a magnetic field. We also require that the RMS noise is not greater than 0.2 photoelectrons. If the readout noise is low enough, the gain can be monitored in situ using the amplitude of the single pe dark count rate signal. The gain measurement is very important in understanding and regulating the temperature of the MPPCs and electronics, which is essential to T2K. The value 0.2 is actually a factor of 2 better than required, but allows for much improved accuracy in the gain measurement. The MPPCs will be used to read out the scintillation bars of the various sub-detectors, some of which will be over 4 m long; therefore, to calibrate the detectors' response and to trigger on certain types of events—e.g. cosmic muons—the electronics readouts must also have a clock module which can tell the time at which an event was received. The time stamp resolution must be less than 3 ns to achieve optimum track reconstruction in ND280. A bias voltage trimming resolution of 20 mV is also necessary, since we need to be able to adjust the gain with 2% precision to account for intra-device variations. For typical $V_{OP} - V_{bd}$ values of 1 V, where V_{OP} is

operating voltage and V_{bd} is breakdown voltage, we find the gain around 10^6—the operating voltage and gain are closely related. The front end electronics readouts are selected with these requirements in mind.

Trip-t front end boards or TFBs, fulfil all the requirements for the MPPC readout needs of T2K. Each TFB takes 4 Trip-t chips—(originally designed at Fermilab for light photon counter readout for the D0 experiment [28]). Each Trip-t chip has 32 channels, each with a preamplifier, an amplifier and a discriminator (see Figure 37).

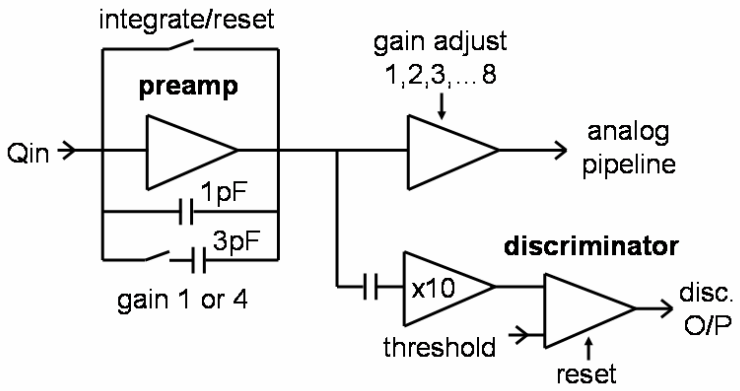

Figure 37: Schematic of one Trip-t front end channel.

The MPPCs of T2K will receive a range of signal strengths which must be capable of being read out by the TFBs simultaneously while resolving the time stamp information. This is done by dividing the input signal between the low and high gain channels. This, therefore, means that one Trip-t chip can read out 16 MPPCs, this can be seen in Figure 38, where the coaxial cable coming from the MPPC delivers the signal to two Trip-t chips.

The TFB has an on-board field programmable gate array (FPGA) which performs the time stamping, configuration, calibration, analogue data readout, sequencing and digitisation, cosmic trigger and slow control operations. The

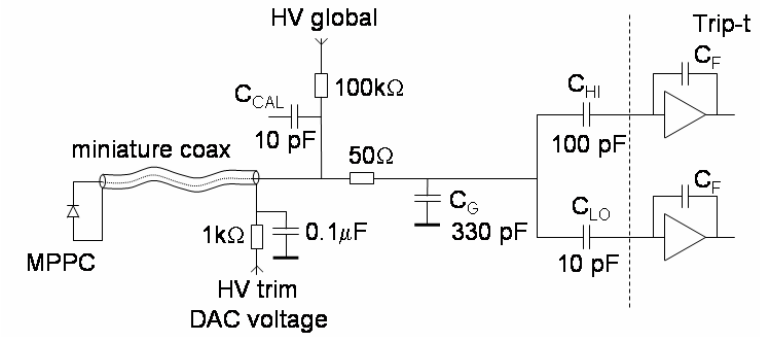

Figure 38: Schematic of one MPPC/Trip-t interface showing the charge splitting between the low and high gain channels and MPPC bias scheme.

TFB is instrumented with the 4 Trip-t 32 channel chips and the 16 coaxial cable connectors to connect the MPPCs to those channels, power connectors, data and trigger modules and charge injection switches. Annotated photographs of the front and back of the TFB showing the full instrumentation can be found in Figures 39 and 40 respectively and more information regarding their instrumentation can be found in Reference [29].

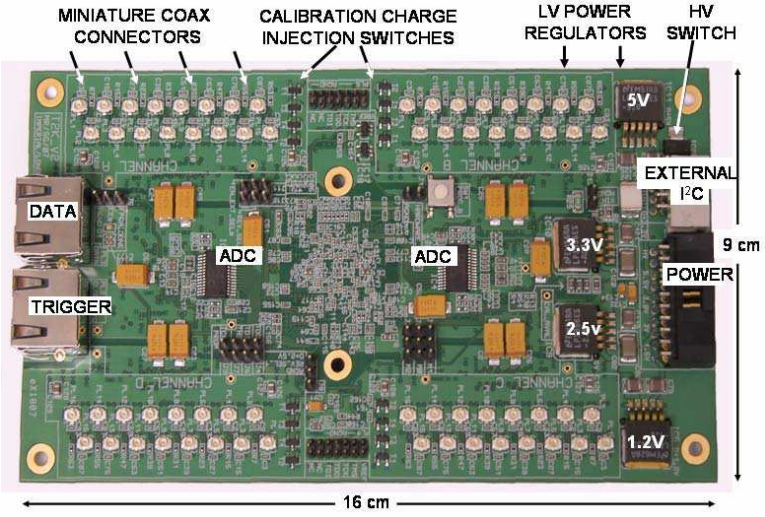

Figure 39: Photograph of the top surface of a TFB.

The TFBs are then processed by read out merger modules (RMMs) which

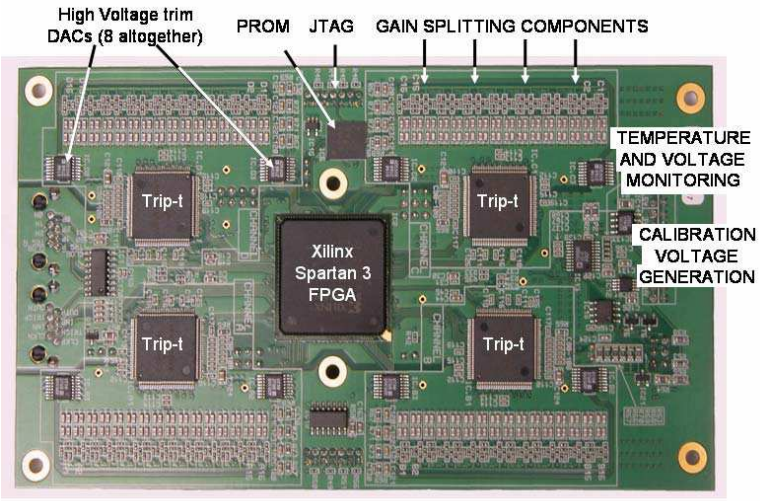

Figure 40: Photograph of the bottom surface of a TFB.

can readout up to 48 TFBs each. The RMM communicates between the TFB and data acquisition system (DAQ) using MIDAS data acquisition software (Maximum Integrated Data Acquisition System) [30]. With the data in computer readable format, the suite of software designed by the T2K ND280 experiment as described in Chapter 5, can be used to understand it.

4.2 Assembly, Testing and QA of MPPC's

Each MPPC is individually tested at Hamamatsu Photonics before being sent to be assembled and tested for installation in the T2K detectors. The MPPCs to be used in the 13 ECal modules were assembled and tested in the UK, and about half of those to be used in the barrel and P0D ECal modules were assembled (and tested to ensure that they have the expected behaviour and correct polarity and also to check the interconnections) at Queen Mary University of London. I was part of the team responsible for this.

The MPPC is first tested prior to assembly. Wearing gloves at all times the

active area is inspected for dirt, dust, smears etc and if not completely clean, is cleaned using isopropanol and a continuous fibre cloth. The pins of the MPPC are then touched onto a testing unit to ensure that the readout is 0.7 V; the positive and negative pins can be distinguished thanks to a small hole in the face of the MPPC on the side of the negative pin. The MPPC is now ready for assembly. First the pins are inserted through a round foam spring which is positioned against the back face of the MPPC. This helps to cushion the MPPC against knocks and allows it to be more easily inserted inside the inner grey plastic shroud, as described earlier. The PCB and coaxial cable are then attached and the MPPC is then once again tested on the voltage testing unit to ensure that everything has been attached correctly. The identifying bar-code is then stuck to the outer protective shroud, which is then put in position over the assembled MPPC.

In the first round of tests (for the 3400 MPPCs to be used for the DSECal) at Imperial College London, all MPPCs were tested and it was found that less than 1% were faulty; for this reason 12.5% of the MPPCs for the barrel and P0D ECals were set aside for testing.

MPPC testing and assembly was performed in a clean room regulated to 22° C. We performed the testing using a specially designed setup that can simultaneously test 64 assembled MPPCs. The setup consists of a light-tight box containing LEDs which transmit light along WLS fibres identical to those used in the ECal; the ends of these fibres are then connected to identical optical connectors as those used in the DSECal. The MPPCs can then be connected to these from outside the box. The intensity of light at each fibre end is measured in advance and used as correction factors for the measurement of the photon detection efficiency (PDE) of the connected MPPC. There is one permanently

affixed "golden MPPC" whose PDE and other functionality has been examined and tested at Sheffield University and is used as a reference MPPC for PDE calibration and monitoring. The 63 MPPCs to be tested were then affixed to the remaining 63 optical connectors and the coaxial cables attached to them connected to a Trip-t front end board, the same as those used in the ECals. This system is encased within another light tight box which opens to enable the MPPCs to be connected and disconnected. This testing setup can be seen in Figure 41.

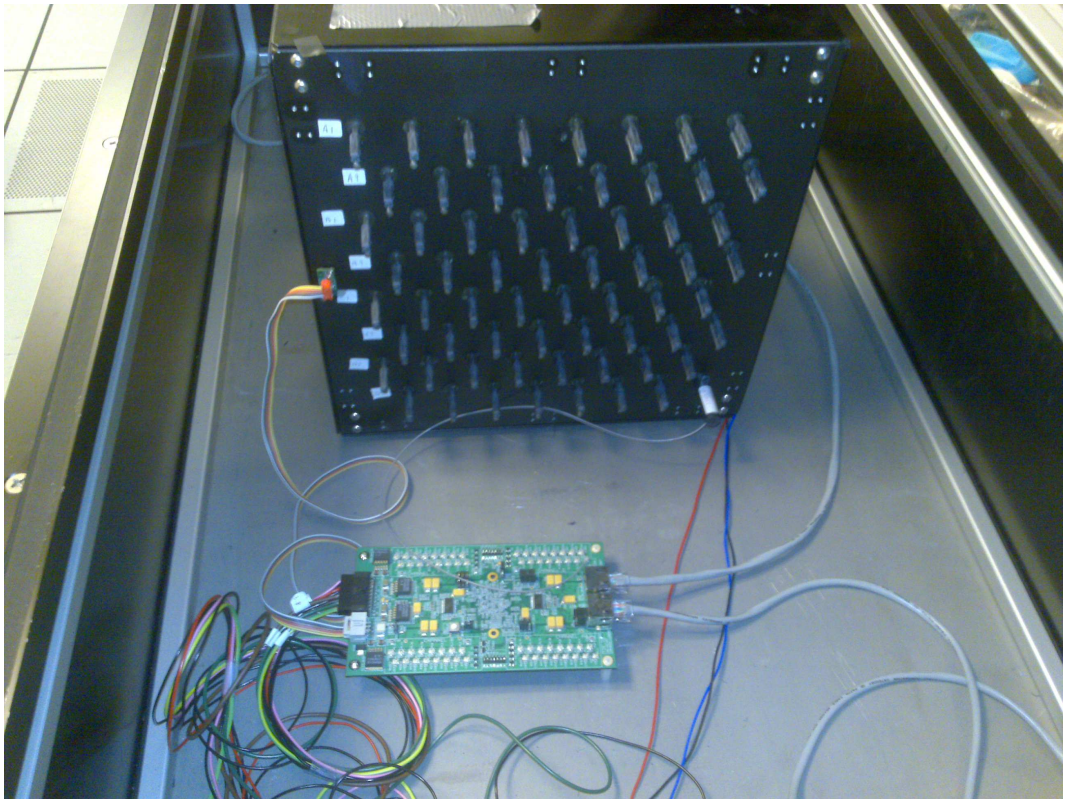

Figure 41: The light tight box containing the LED and WLS fibres with optical readouts protruding are shown here. The golden MPPC - bottom right—is connected to the TripT front end board and the whole system is contained in a light tight (when closed) crate. The cables which can be seen attached to the TFB are the readout cables carrying the information to the PC.

The TFB is connected to a PC which reads out the board using the MIDAS

data acquisition software (Maximum Integrated Data Acquisition System) [30], as used by ND280. A schematic of the test system can be seen in Figure 42.

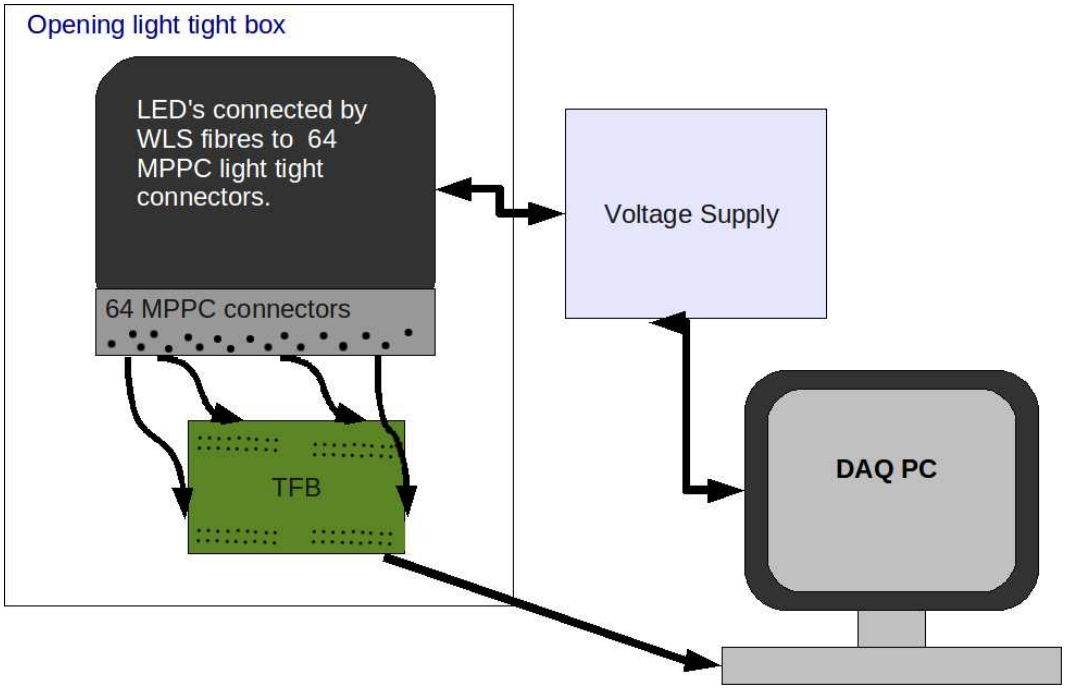

Figure 42: Schematic of the testing setup.

The first part of the testing procedure—to ensure that each device is "alive"—is to ensure that an ADC (analogue to digital converter) signal of 1 peak per photoelectron is observed by each device over approximately 3000 events. We obtain the baseline voltage and calibration voltage (bias voltage at which all MPPCs are below the breakdown voltage i.e. the point at which there is 0 gain) and determine the average voltage. This is the voltage at which photoelectron peaks are visible for each device. The MPPC gain can be determined easily as the separation between photoelectron peaks in the ADC spectrum is large, due to the high gain of the devices. The gain changes linearly with the voltage V as in Equation 4 and in Figure 49. The temperature inside the test system is obtained at the start and end of this preliminary test

- if it differs, the test must be run again, as this can mean that the voltages obtained are incorrect.

The ADC count histograms for the 64 MPPCs, including the golden MPPC (described above), are examined by eye to ensure that the pe peaks are visible and well defined. Figure 43 shows a test where three of the MPPCs (at positions A:10, B:8 and B,14) appear inactive, while the rest show a good ADC count spectrum. In this case, the offending MPPCs were mounted the wrong way round during assembly.

Once we are certain that all devices are operating, they can be rigorously tested (if one fails the test it is checked retest and if it fails again set aside and not used). A series of pedestal runs is taken to determine the dark noise rate and the bias voltage of the MPPCs when the LED is not switched on. The dark noise rate is calculated by measuring the number of events observed by the MPPC when the LED is off and dividing the number of events by the measuring time. We can assume that the number of true dark noise events, in the absence of cross talk (the process where one pixel causes an avalanche in a nearby pixel) and after-pulses (where one pulse causes another subsequent pulse) between neighbouring APDs, follow Poissonian statistics, allowing the number of true dark events n to be estimated from the fraction of pedestal events among the total events P(0), as:

$$n = -\ln(P(0)). \tag{21}$$

Dividing n by the gate width, the dark noise rate is calculated. Figure 44 shows the dark noise rate of the golden MPPC. This is an ideal and well understood spectrum.

Figure 45 shows a working MPPC whose dark noise spectrum agrees well

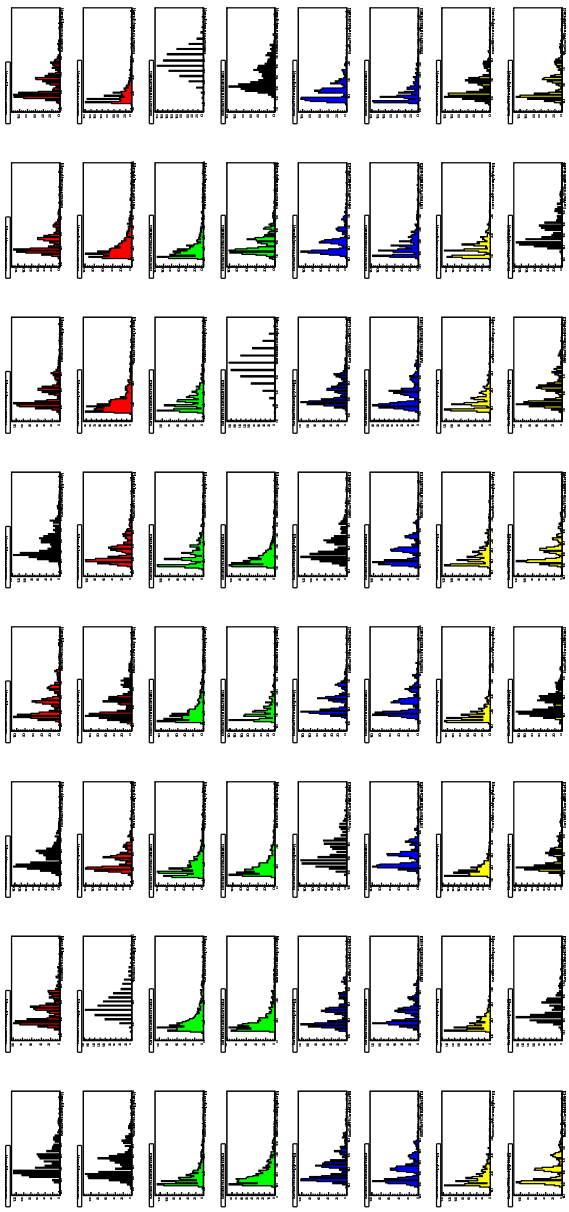

Figure 43: The plots are arranged so that every 2 rows run consecutively through inputs A to D coloured red, green, blue and yellow respectively on the TFB readout. They are numbered right to left from 1-16. The golden MPPC is in position D16 (at the bottom right of the canvas). In this example it can be seen that three MPPCs appear non-operational - those in positions A10, B8 and B14 in the green blocks. In this case, the MPPC had been assembled the wrong way round, with the negative pin in the positive position. All other MPPCs are operating as expected at this level of testing.

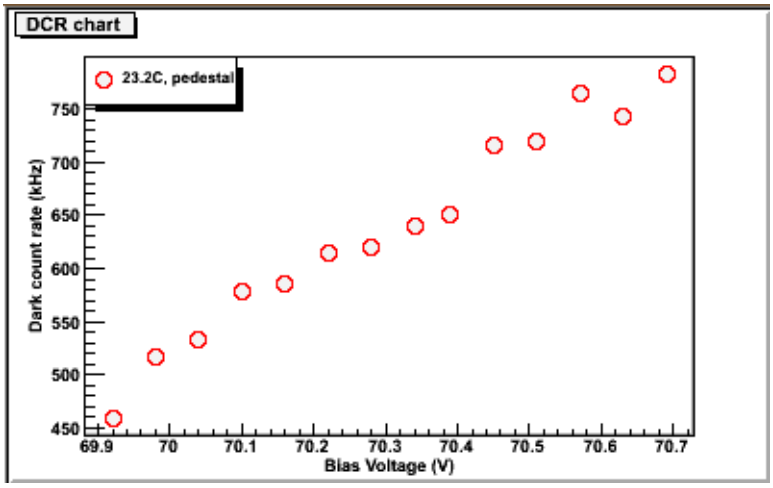

Figure 44: Dark count rate against bias voltage pedestal plot for the golden MPPC.

with the golden MPPC.

A second set of runs is taken where the LED is turned on, and by comparison of these signal events with the pedestal runs and Poissonian statistics as above, we can determine the cross talk, after-pulse and PDE of the MPPC. The after-pulse and cross talk probability is about 0.2 at an over voltage of 1.5V, an acceptable level for ND280, which we know well from previous tests [27]. Therefore we are mainly testing the PDE of the MPPC. Figures 46, 48 and 47 show example after-pulse spectra for the golden MPPC and the good and bad MPPCs examined above, respectively; again we can see that the two are in good agreement with a positive linear shape to both, with no obvious inconsistencies for the bad MPPC at this stage.

The primary relationship of interest, however, in any such comparison is the gain vs bias voltage for the MPPC along with its pedestal. This is done through the study of the dark rate and after-pulse fraction obtained from the previous plots, as described above. It allows us to judge how well the pedestal and signal data agree. For gain there should be an almost overlapping positive

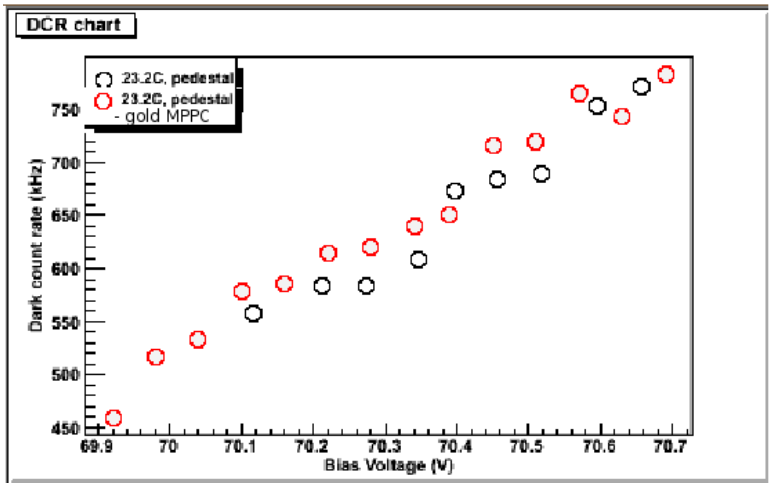

Figure 45: Example dark count rate against bias voltage pedestal plot for a working MPPC: also showing the gold MPPC; for reference, this MPPC is number TG5609.

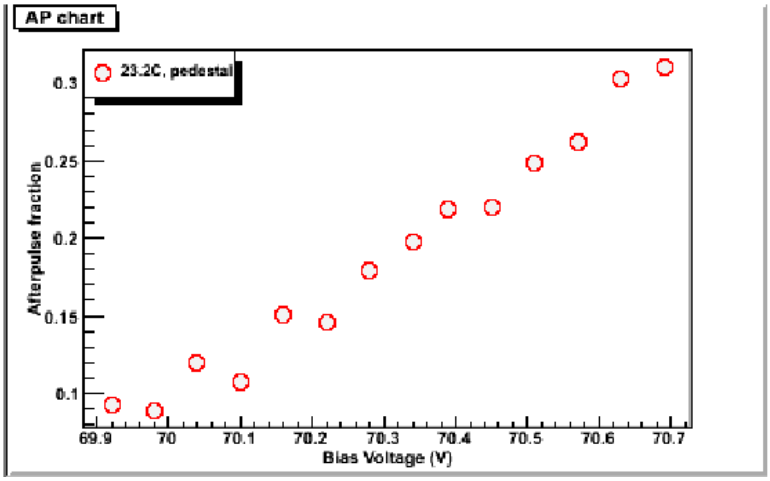

Figure 46: After-pulse fraction against bias voltage pedestal plot for the golden MPPC.

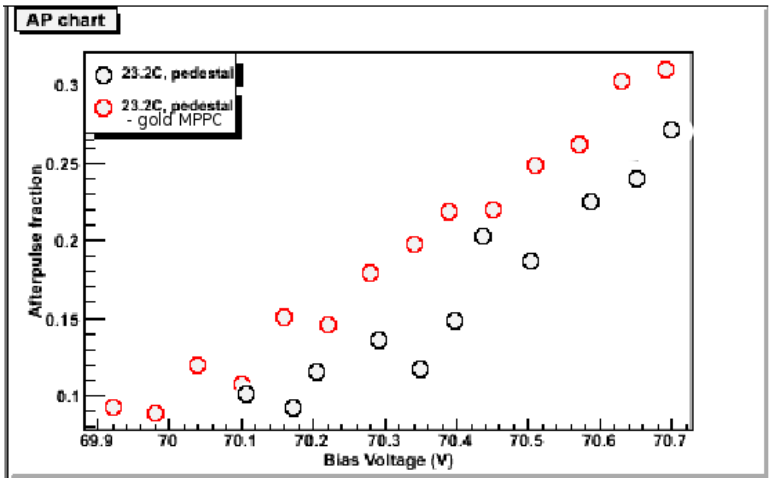

Figure 47: Example after-pulse fraction against bias voltage pedestal plot for a working MPPC, which compares well with the golden MPPC, also shown; for reference, this MPPC is number TG5609.

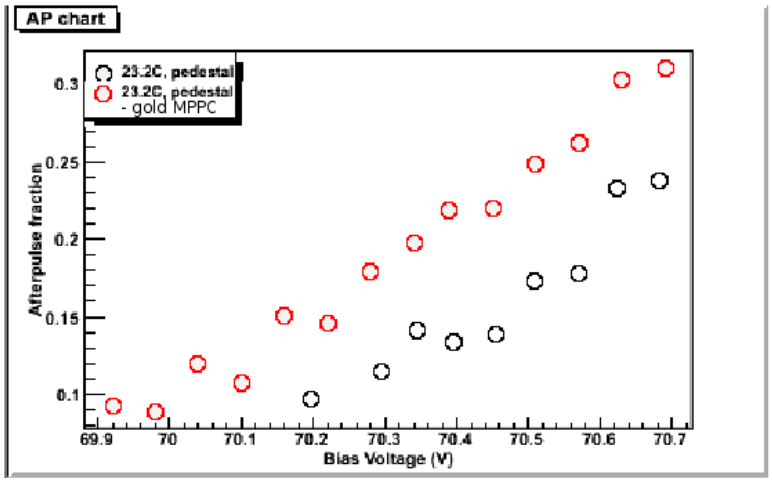

Figure 48: Example after-pulse fraction against bias voltage pedestal plot for a bad MPPC; it compares well with the golden MPPC—also shown—at this stage; for reference, this MPPC is number TF4090.

linear relationship with many data points for comparison. In Figure 49, we can see that the results are highly correlated for the pedestal and data runs (when the LED was on). There are many points for comparison and the temperature was the same for both the pedestal and data runs as required.

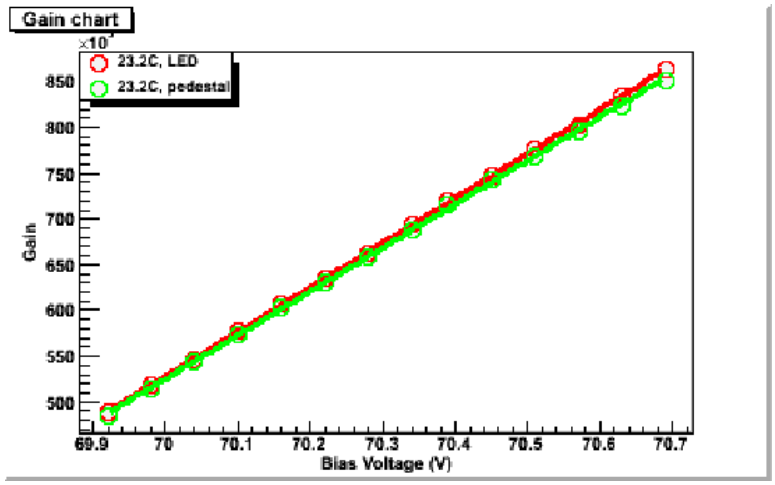

Figure 49: Gain versus bias voltage for the golden MPPC. The red line shows the pedestal data, while the green represents the run with the LED on. The temperature for each set of runs was $23.2°C$.

Figure 50 shows a good MPPC which passed the test well; it compares very well with the golden MPPC and fulfills all the test requirements.

Figure 51 shows a bad MPPC which failed the test: the data and pedestal runs do not compare well, thus failing test requirements. Such MPPCs will be examined to ensure that there is nothing wrong with their assembly and then re-tested. If they fail again they are rejected.

Finally, we consider the photon detection efficiency (PDE) histograms for each MPPC: plotting the PDE as a function of bias voltage. An approximately linear relationship should be observed with increasing bias voltage creating increased PDE. This can be observed, in both the golden MPPC and our example good MPPC (TG5609) (see Figures 52 and 53).

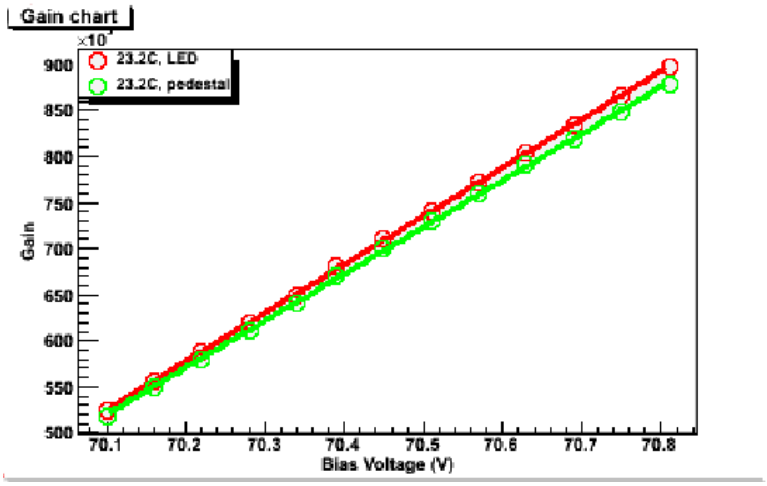

Figure 50: Gain versus bias voltage for a working MPPC; for reference, this MPPC is number TG5609. The red line shows the pedestal data, while the green represents the run with the LED on. The temperature for each set of runs was 23.2°C.

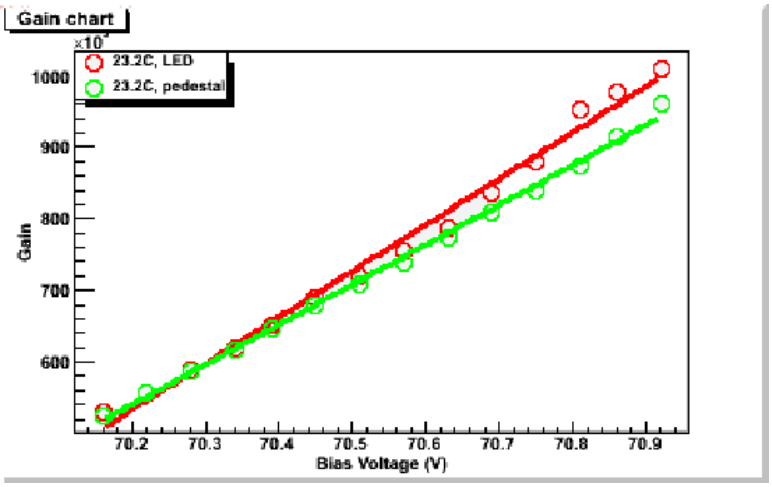

Figure 51: Gain versus bias voltage for an MPPC which failed testing; for reference, this MPPC is number TF4090. The red line shows the pedestal data, while the green represents the run with the LED on. The temperature for each set of runs was 23.2°C.

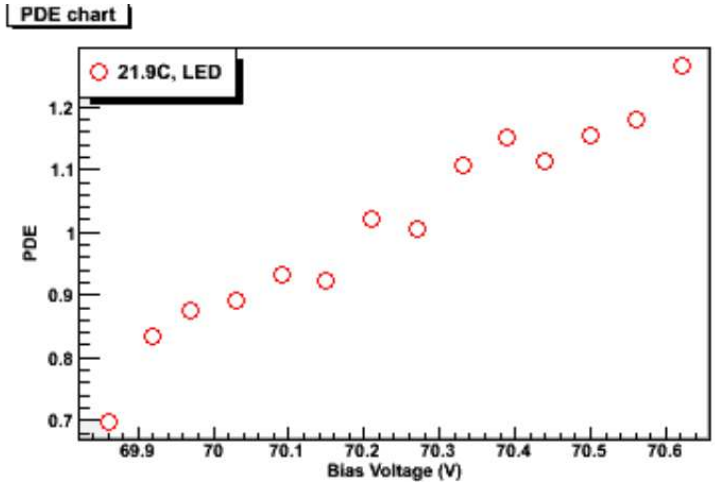

Figure 52: PDE versus bias voltage for the golden MPPC. A nice relationship can be seen with PDE increasing with bias voltage.

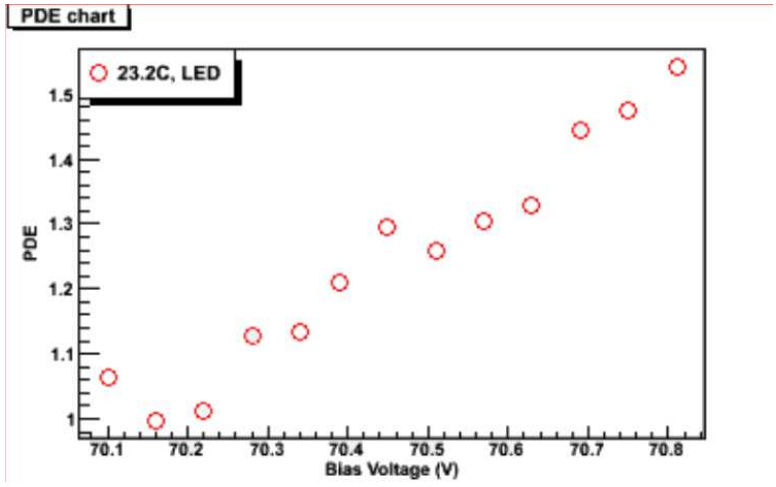

Figure 53: PDE versus bias voltage for a working MPPC; for reference, this MPPC is number TG5609. A nice relationship can be seen with PDE increasing with bias voltage.

In some cases, the relationship between bias voltage and PDE was not linear and therefore the MPPC failed the test: an example is shown in Figure 54.

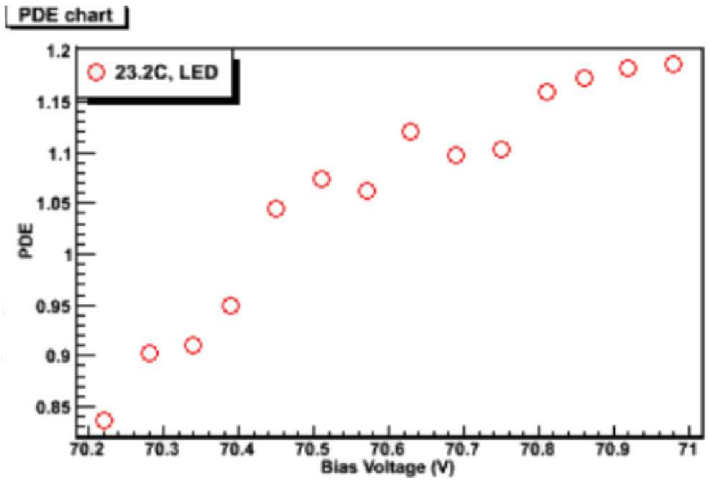

Figure 54: PDE versus bias voltage for a bad MPPC; for reference, this MPPC is number TG0211. In this case, PDE increases greatly with bias voltage at first, then at a much slower rate with higher voltages. This MPPC was therefore rejected.

4.3 Conclusions from Testing and QA of MPPCs

The ND280 detector uses multi-pixel photon counters, MPPCs, which were specifically designed by Hamamatsu Photonics to the needs of T2K. They are small in size, unaffected by the magnetic field and have the ability to detect a single photon, through 667 APD pixels, in a 1.3 mm^2 area. They are tested initially by the manufacturers in Japan and then again by the ND280 collaboration.

I helped to assemble and test the MPPCs to be used in the barrel and P0D ECals. The tests are designed to ensure that the MPPC is not only working but working within the levels required by T2K. Their after-pulse fractions and gain against bias voltage for both pedestal runs—with the LED off—and data runs—with the LED on—are compared. The photon detection efficiency of

each device is also examined. Around 10,000 MPPCs were assembled at Queen Mary University of London and approximately 1200 of these were tested. Less than 0.4% of those tested were found to be miss-assembled after the initial test and later corrected; less than 0.5% were found to be faulty after the main analysis test.

5 The T2K ND280 Software Suite

The T2K ND280 group has developed an ND280 dedicated suite of software, written—mainly—in C++ with an modular package structure. Each aspect of the experimental analysis from Monte Carlo (MC) production to the reading of data, reconstruction and analysis is organised into packages, or groups of packages, which can manage the tasks. The ND280 software is documented in its entirety in the ND280 Workbook. The Workbook is an online resource which I produced to enable everyone working on T2K ND280 to be able to get started with ease and use the software from the word 'go'; it also has information for experienced members of T2K working on, with or developing the ND280 software suite, and many software and analysis tutorials. The process of package management and release management is managed through CMT [31] in combination with CVS [32]. CMT, CVS, the ND280 package structure (as of July 2010) and purpose of said packages, along with data management and access, and the T2K ND280 Workbook are described in this chapter. A pictorial overview of the ND280 software suite and the way it interacts can be seen in the diagram in Figure 55.

5.1 The T2K ND280 Software Packages

The T2K ND280 software suite is organised into a set of over thirty software packages and their respective sub-packages. These packages fall into seven categories: there are ten framework packages, three simulation and three database packages, seven calibration packages, eight reconstruction packages, one analysis, one utility and one documentation package. The purpose, implementation and use of each package is described in the following subsections. Most of the package names begin with the letters "oa" for "off/on-axis'.

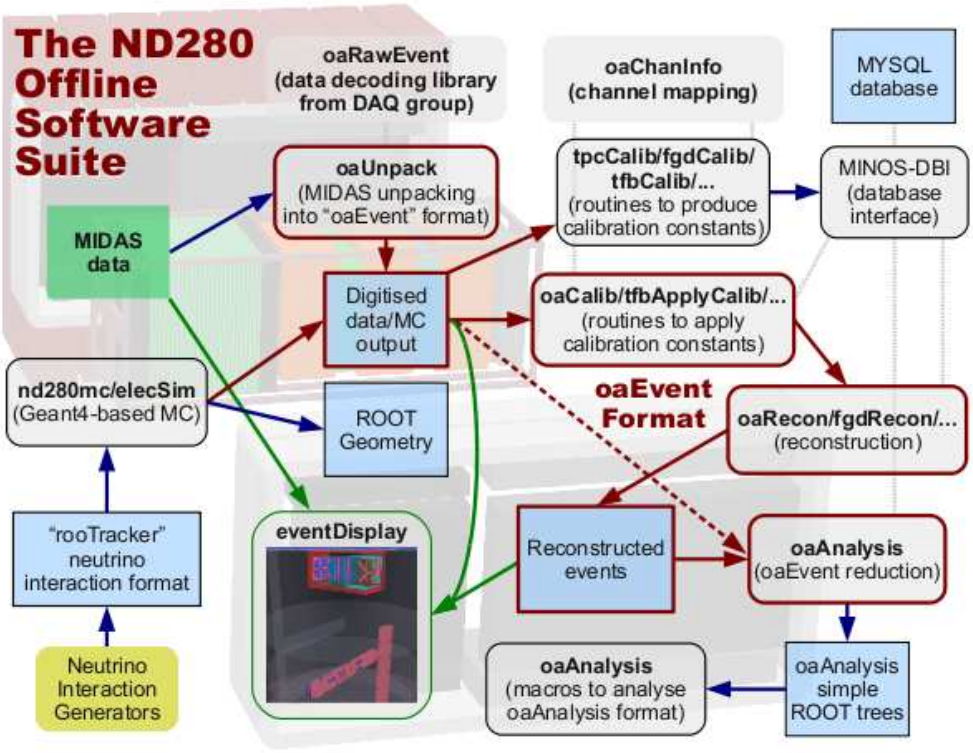

Figure 55: A quick pictorial overview of the ND280 software suite and the way it interacts.

5.1.1 The Framework Software Packages

The 11 ND280 software framework packages provide the low-level framework for ND280 software, such as handling input and output (I/O) and interfacing with the databases. Most of the other ND280 packages depend on these framework packages. They are oaEvent, oaRawEvent, oaUtility, oaGeomInfo, oaCalibrationDatabase, oaRuntimeParameters, oaUnpack, nd280Control and testBase.

The oaEvent package provides the main, basic I/O library of functions for the T2K ND280 offline software. It defines the event format and is required by any package expecting to read or write events. The I/O framework is provided by ROOT [33], which is used to save TND280Event objects (ROOT TTrees with a single branch containing events) and the detector geometry.

The oaRawEvent package provides the software necessary to read MIDAS [30] data acquisition files and to process the data they contain. This is distributed between two packages: oaEvent and this package. oaEvent provides the core functionality to read the files and return the data they contain as unstructured arrays, whereas the purpose of oaRawEvent is to provide access classes which interpret these arrays and expose the logical structure. oaRawEvent contains information specific to the online data packing scheme. The classes of this package are designed with the aim of "opaque encapsulation", so that users will be immune to any DAQ development work resulting in changes to the layout.

The oaUtility package contains a collection of utility routines which are very useful and commonly used. It is one of the core libraries and should collect all of the routines which are generally useful, but are not specifically related to event or data base I/O.

The oaGeomInfo package is a library containing a collection of useful routines which are related to the geometry of the ND280 detectors, including INGRID. These are then used by the simulation packages and the reconstruction framework of packages. oaGeomInfo separates these utilities into separate classes for each of the ND280 detectors and provides information on scintillator geometry.

The oaCalibrationDatabase package is a temporary database for storing calibration constants. The database is used by the reconstruction packages to read in initial calibration constants, for the development and testing of the reconstruction software.

The oaRuntimeParameters package is a package which provides access to the runtime parameters, which are stored in text files.

The oaUnpack package manages the conversion from raw data files (in MIDAS format) and its ND280/ROOT format, offline equivalent. In addition to this, it provides early operations to the data, such as filtering of the event stream by trigger type, such as cosmic muons or beam.

The nd280Control package is a "front end" package, providing a program called runND280, which runs all the ND280 software packages which need to be run as requested in a configuration file. The system works on a modular basis, with different modules carrying out different tasks. A job is designed as a series of modules, run step-by-step to produce the requested output. This allows nd280Control to generate the pure ROOT analysis output files from the neutrino Monte Carlo. In short, rather than implementing each stage of the software one-by-one, nd280Control runs the full chain from the specified package names and the input files to be used.

5.1.2 The Simulation Software Packages

The three simulation packages are nd280mc, elecSim and (loosely speaking) oaCherryPicker. These packages provide the simulation of the ND280 detector.

The nd280mc package is the ND280 off-axis detector simulation Monte Carlo package. The particle transport is performed using GEANT 4 [34] and has a flexible geometry which can be changed at run time to meet the requirements of the user. This only simulates the energy as it is deposited in the detector. It does not simulate the electronics response which is performed by the elecSim package.

elecSim performs the ND280 off-axis electronics simulation. This library and program contains several classes simulating different types of electronics. This takes care turning raw MC "hits" into digitised electronics output which represent "calibrated" detector hits.

The oaCherryPicker package provides methods to take an input file and output a sub-selection of the events in that file, depending on criteria set by the user.

5.1.3 The Database Packages

The three database packages—oaSlowControlDatabase, oaOfflineDatabase and MINOSDBI—are the database and database interface packages, where any and all constants of the near detectors are stored in addition to pedestal data, for example.

oaSlowControlDatabase gives access to the slow control variables and data stored in the slow control MySQL database (slow control is the term for the control of equipment such as high voltage power supplies and temperature readers).

The oaOfflineDatabase package provides access to calibration tables from the Offline Database. The primary interface it offers is to return all the rows from a specified table which satisfy the current "context" (i.e. date and time of the current event).

MINOSDBI is a short-term back-end implementation for the ND280 offline database. It is a direct copy of the MINOS [17] code which in turn interfaces with ROOT's MySQL package.

5.1.4 The Calibration Packages

The six ND280 calibration packages provide the low level data processing and calibration algorithms needed for data analysis. They are: oaCalib, magnetCalib, ecalCalib, tpcCalib, fgdRawData and tfbApplyCalib.

The oaCalib package is the general calibration package for all ND280 sub-detectors. The magnetCalib package provides maps of the magnetic field within the ND280 detector. The tfbApplyCalib package calibrates the TFB readout channels of all sub-detectors using the TFBs.

The ecalCalib package provides routines for the calibration of the ECAL. This package contains two objects: TScintCalibratedHit and TECALCalScintBar, TScintCalibratedHit is a calibrated hit object for the ECAL. TECALCalScintBar applies a correction to the charge recorded on a TScintCalibrated hit and returns a charge in MIP units (2.2 MeV). Equivalently, tpcCalib is responsible for the calibration of the TPC and fgdRawData provides the main elements of the FGD raw data processing.

5.1.5 The Reconstruction Software Packages

Each ND280 sub-detector has its own reconstruction package dealing with reconstructing MC events and data events which have been converted into

ROOT format and calibrated. There is also a package which deals with reconstruction across all sub-detectors combined. It matches the reconstructed tracks from each sub-detector to form combined ND280 tracks; this package is oaRecon. I worked to perform the initial track matching between the TPC and the FGD tracking detectors in addition to matching tracks in either or both these detectors with the ECals. This is done by matching the start and end points of tracks falling within the fiducial volume of these inner detectors, with the end point or start point depending on the direction of the track, with one which begins in the subsequent, or previous, detector. The energy, direction and timing information of such tracks are also considered in order to improve the efficiency of the track matching algorithm. oaRecon is now well advanced and performing well with high efficiency matching tracks between all ND280 sub-detectors.

5.1.6 The Analysis Software Package - oaAnalysis

oaAnalysis can take input files from any of the sub-detector output packages and is responsible for all subsequent analysis tasks. The package is organised into two subsets of files - modules and macros. The modules represent classes which distil the event information into mutually-related chunks. The macros contain analysis scripts which read the analysis output files from the modules. They are written to the needs of end users and can be written in ROOT, PYTHON or Perl. I have worked extensively on the module which allows reconstructed events from the ECal to be utilised in oaAnalysis i.e. TTrackerECalRecon. This module saves output event objects from ecalRecon into ROOT trees, which can be used in analysis. I have also produced numerous analysis macros which perform such tasks as near detector electron neutrino analysis, comparisons between MC and data, and cosmic muon analysis. Many

of these macros will be described in detail in the following chapters.

5.1.7 The Utility Package - eventDisplay

The ND280 event display package, aptly named 'eventDisplay', allows events in the ND280 detector to be viewed. It runs using 'eve' a ROOT pluggin [33]. All sub-detectors can be viewed in 2D or 3D and navigated by the user, so that event may viewed from a variety of angles.

An example event display showing one of the first fully reconstructed cosmic muon events traversing most of the ND280 sub-detectors can be seen in Figure 56.

5.2 T2K ND280 Data Distribution

The data taken at the ND280 site in J-PARC and at the various testbeams (TRIUMF for the FGD and TPC, and CERN for the DSECal) needs to be stored and distributed around the globe. Then this data can be run through the software described earlier in the chapter, converting it into a form ready to be analysed. It is clear that this cannot take place on site using so called "online" machines, since this will take up vital storage and processing time from the data acquisition system. The process of data transfer and backup therefore, becomes an essential part of not only the data management, but the efficiency of the T2K experiment.

All T2K ND280 data is collected via MIDAS [30] data acquisition software. The MIDAS software performs "slow control", which is to control and test the equipment, including high voltage power supplies and temperature. The raw data output is then passed through semi-offline processing, which performs stable low level functions to test the validity of the data—such as hit maps,

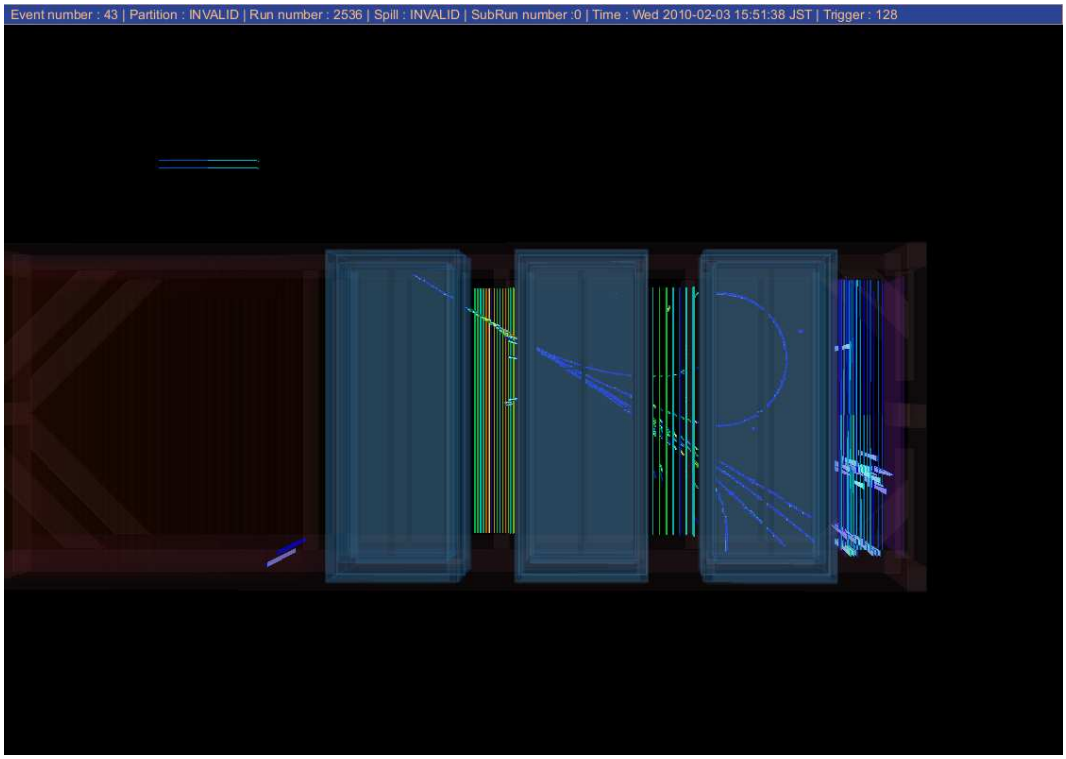

Figure 56: Event display of one of the first fully reconstructed cosmic muons at ND280. The P0D can be seen on the far left in deep purple. A cosmic muon enters the first FGD from the top right and subsequently showers. This electron shower can then be seen traversing FGD2 and TPC2. In TPC3 an electron track bends under the effect of the magnetic field. Finally, on the far right of the event display, the electron shower can be seen in the DSECal.

and low level reconstruction tasks. Experimental data taken at J-PARC is stored at the KEKCC (the computing centre of the KEK science facility in Tsukuba which is linked with J-PARC) primary data store (archive), before being copied to the secondary archive machines at TRIUMF facility in Canada and the Rutherford Appleton Laboratory (RAL) in the UK. Testbeam data on the other hand—the validated raw data—is copied directly to the secondary storage nodes at TRIUMF and RAL, where a backup archival copy is stored. The data is then uploaded to the GRID [35], where it can be accessed. The GRID (known as GridPP in the UK) is a network of computers from around the globe working together to operate on a small portion of a computational task each, which would take a single CPU many hours, often years, to complete. This enables particle physics experiments such as T2K to process large quantities of data faster and more effectively than ever.

A schematic showing the data distribution system at T2K ND280 can be seen in Figure 57.

5.3 The T2K ND280 Workbook

I have been the leader of the documentation task force for much of my time working on T2K. The documentation task force is a group of people (three including myself) set up to ensure the thorough, up-to-date documentation of all software packages including an in-depth overview of the package, a description of its release history and fully documented code. Documentation is a vital part of the successful operation of any suite of software with multiple authors. As the experiment matures and grows, more and more people are developing and using the software, therefore it is important that its full range of features is well understood and can be adequately exploited. This was no

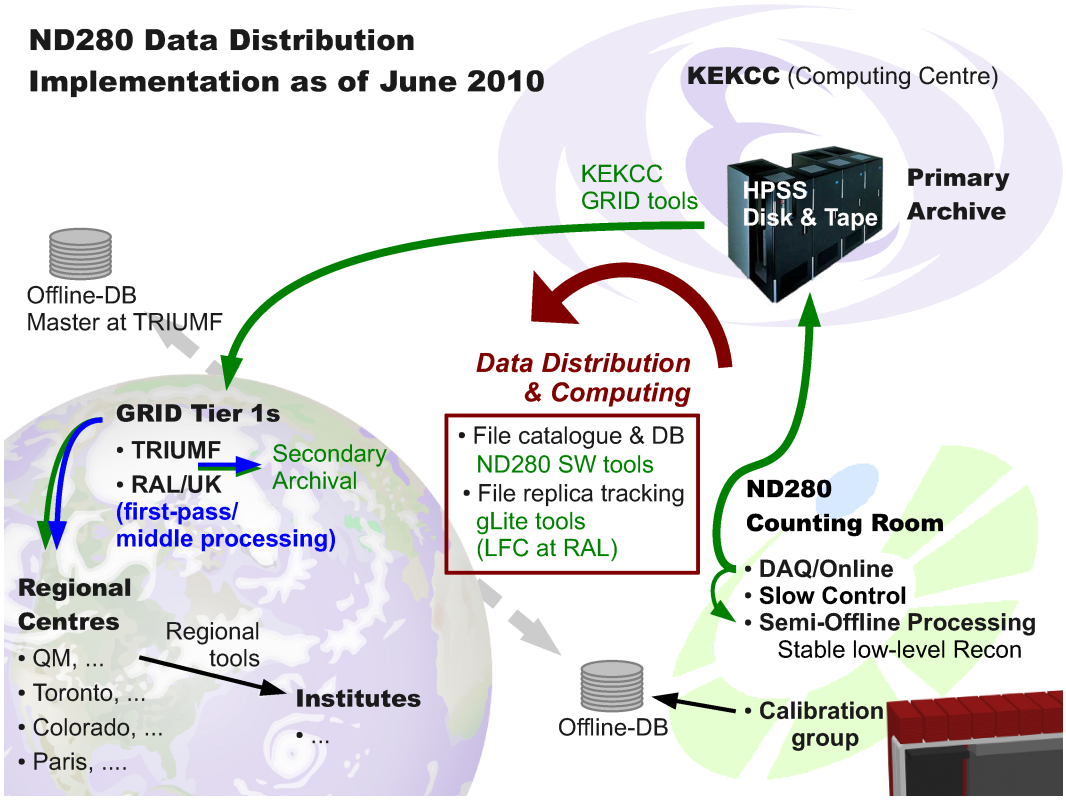

Figure 57: Schematic of the data distribution system of ND280 [36].

small feat and there was a long way to go in the beginning to get things to the required standard. In the first instance, each package and sub-package was examined in detail, noting all areas where improvements were required to the documentation. After this it became quite apparent what the universal package documentation requirements should be. With this in mind, we produced an outline for package documentation containing a set of guidelines for all areas of documentation which should exist (see Appendix A). Many of the initial package overview descriptions were written either solely or in part by the documentation task force. We also ensured that every object of every file was documented and helped extensively in the writing of this documentation.

In my role as documentation task force leader, I was the sole producer of the T2K ND280 Workbook—an online resource to getting started with the T2K ND280 collaboration and to using and developing the software. It can be difficult at first to get set up and working within a large collaboration and very time consuming learning to navigate the necessary software (which you will be using). Therefore, many large particle physics collaborations have such a Workbook. The remit of the T2K Workbook was to plug this information gap. The Workbook contains: pages for new users with advice such as which mailing lists to join and relevant accounts which collaborators should obtain, step-by-step guides to getting the software installed and set up and easy to understand overviews of the different software packages, what they do and how they interact. There are also tutorials on how to run the software for data and Monte Carlo and how to produce analysis scripts to do a unique analysis, in addition to information for developers such as how to write and commit code and documentation to the repository.

The Workbook is available as a separate online resource hosted on the TRI-

UMF server and also through the ND280 and T2K websites. The homepage describes what is covered in the Workbook and on the left side it has a list of quick links to the pages it contains. This list appears on every subsequent page for ease of navigation. There is also a schematic overview of the software and details of when last updated and who to contact with concerns. The home page can be viewed in Figure 58.

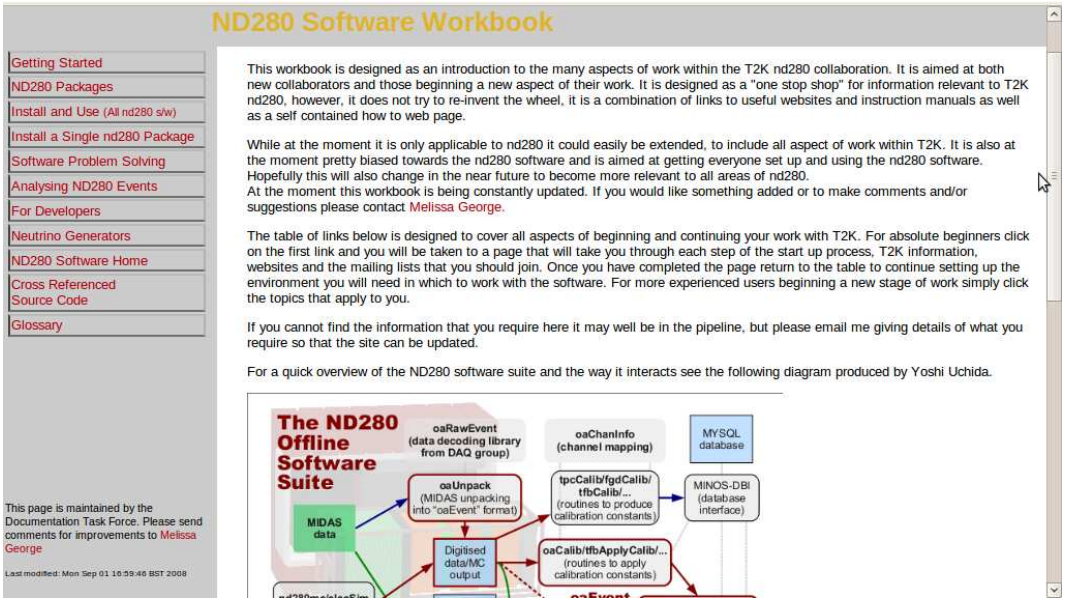

Figure 58: The T2K ND280 Workbook homepage. It includes an overview of its contents, a quick description of the software and table of quick links to pages on the left.

A new user can then navigate the pages in order, being taken through the steps to get set up with ND280 and on to the package descriptions. The software overview page lists all the packages of the software grouped according to how advanced in the software the user is. The first section of the overview page includes those packages with which everyone needs to be familiar—such as nd280Control and eventDisplay—then on to packages for those who have got to grips with the most basic of packages and are ready to understand

the more advanced processes—such as the reconstruction and analysis. This structure continues until it reaches packages which are mainly for developers—such as testBase. The page begins with a description of how the package documentation is laid out. Then each package has a row of: a table of all packages, with links to the stable and development version of the package on the left hand column, and a one paragraph description of its purpose and uses on the right.

Now that the reader is aware of how the software works and what happens where, there is a page taking the user through the downloading, installation and setup of the software. This page requires no previous programming knowledge. Again, it has a tabular structure, with the command line inputs which can be cut and pasted shown in the left hand column, and a description of what these comments do and why you have to do them on the right, teaching the user some of the basic code needed and how to get the software set up. There is a separate set of instructions depending on the user's operating system—to ensure complete understanding. A screen shot of the page can be seen in Figure 59.

The Workbook contains tutorials explaining how to write an event loop, how to use the analysis package running the existing analysis macros and how to develop a user defined macro. These tutorials enable the user to get a handle on how to work within the software and how to begin 'doing physics' fast.

There is then a set of pages for developers with information on how to develop and integrate a new package into the software suite and how to test the package with a system of test programs which can be run before each new release of the software. There is also information on how to: write code within the software suite, to commit it to the repository ands to write documentation.

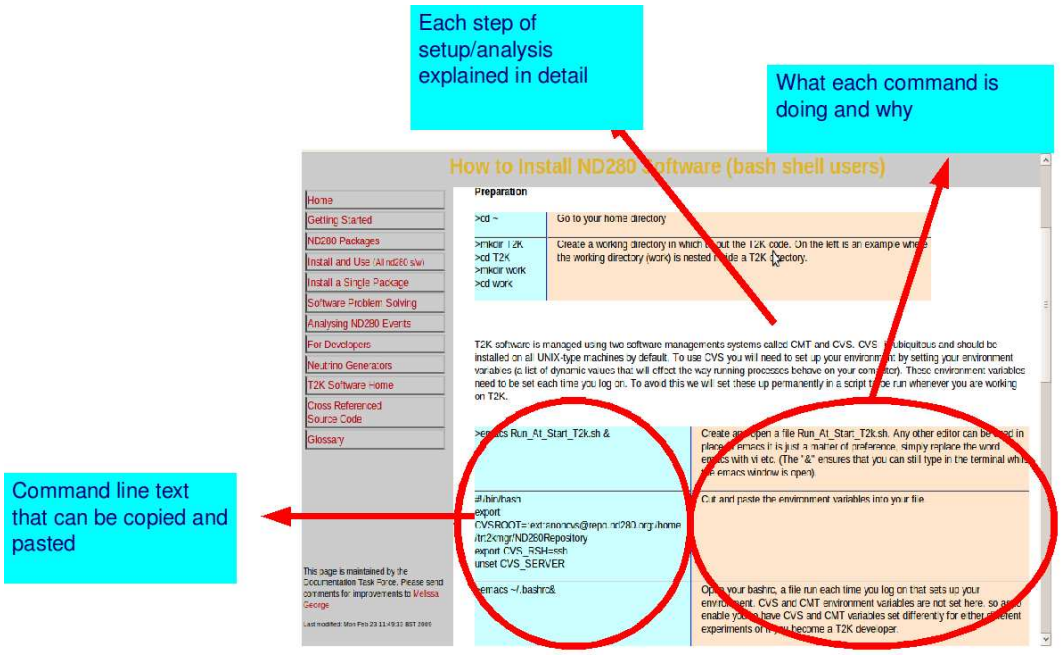

Figure 59: The T2K ND280 Workbook software installation page. Each package has a one paragraph description with links to the software documentation and the table of quick links to pages can be seen on the left.

The Workbook also has pages covering the installation of a specific package or packages, what to do when you have software problems, information on the neutrino generators used in T2K, links to the ND280 software search pages, a glossary of the terms and pseudonyms used in particle physics and T2K, and links to T2K and ND280 documents.

The Workbook has been used by many ND280 collaborators and has become an invaluable resource for the ND280 collaboration.

5.4 Conclusions

The T2K ND280 collaboration has its own suite of software especially designed by those who will use it to perform the necessary tasks of: data acquisition, reconstruction, testing and analysis. The software suite is now quite mature,

but continues to undergo a strict development process as T2K begins data taking.

I am the leader of the documentation task force for the T2K ND280 collaboration and as such, have ensured the accurate documentation of every file and class of every software package and all overview pages for each package. This documentation will soon be produced in printable format.

The T2K ND280 Workbook is an online resource which I produced, and which is used by everyone working on ND280; it is a guide for new users, and includes a set of in depth tutorials into the ND280 software. There is also information for advanced software users and ND280 collaborators, advising on ND280 software development. A Workbook is extremely useful to such mid-large scale particle physics collaborations as T2K, and I continue to receive excellent feedback. A printable version of the Workbook will be produced soon.

The software (and the Workbook in line with it) is now in a well advanced state, but continues to grow and mature as T2K moves into its next phase and begins data taking.

6 T2K ND280 Cosmic Muon Flux

Cosmic muons are very useful to particle physics experiments. They are through going minimally ionising particles which will populate evenly across the detector; they can therefore be used for calibration, helping with particle identification (PID) and for tuning reconstruction tools. It is therefore essential that there exists an accurate cosmic muon flux which can be used to produce Monte Carlo for MC-data comparisons, calibration and software tuning. The T2K ND280 group was in need of such a flux. Cosmic muon data taking for calibration and commissioning of the various ND280 sub-detectors occurred at 4 locations around the world and within different facilities at different heights with respect to sea level. Subtle differences exist in the cosmic muon flux at each of these positions and therefore, to be as accurate as possible, a separate flux was needed for each location. I produced the four fluxes needed by the ND280 group—each is a large event sample (non-normalised) flux produced from primary particles incident on the upper atmosphere propagated to detector level using the CORSIKA extensive air shower simulation package [37]. In this chapter I will describe the production methods for each flux, the flux output and subsequent analysis and the ND280 cosmic MC production and analysis.

6.1 Cosmic Muon Flux Production using CORSIKA

CORSIKA (Cosmic Ray Simulations for KAscade) is an extensive air shower simulation package written and developed by Dieter Heck and Tanguy Pierog of Karlsruhe University and Johannes Knapp of Leeds University. It simulates high energy cosmic particles incident upon the upper atmosphere, their subsequent interactions through any thickness of atmosphere at any given lo-

cation and time of year and the decays of nuclei, hadrons, muons, electrons, and photons in the atmosphere up to energies of some 10^{20} eV. It outputs the type, energy, location, direction and arrival times of all secondary particles up to and including detector level, though the output method must be written by the user. Much of the information pertaining to the propagation of cosmic showers and the secondary particles produced in the detector, can be chosen to be saved or discarded by the user. There is a variety of possible high and low energy hadronic interaction models which can be chosen and over 100 tunable parameters controlling the propagation of the cosmic shower and the secondary particle production—which can be chosen according to the needs of the user's experiment.

CORSIKA was originally developed to perform simulations for the KASCADE experiment [38] at Karlsruhe, Germany and subsequently KASCADE-Grande [39]. It has been regularly updated and upgraded since its initial development. This makes it the perfect choice for use as a production tool for the T2K ND280 cosmic flux - whilst it will produce a lot of superfluous information, it will give the most accurate detector level flux and will be fully reproducible.

6.1.1 The Hadronic Interaction Models and Version of CORSIKA used

I produced the flux using CORSIKA version 6.7. I chose the high energy hadronic interaction model to be QGSJET II (03) [40]—the Quark Gluon String Model with Jets. The program simulates the elastic hadron-nucleon scattering amplitude. This model is well understood and considered to be the most accurate model to date, hence its inclusion here.

For the low energy hadronic interaction model, I used FLUKA (FLUctu-

ating KAscade) [41]. FLUKA is used to calculate the inelastic hadron cross-sections with air, calculating both the interaction and the secondary particles. FLUKA follows high energy particles through matter, however CORSIKA only uses those of its routines which follow low energy hadronic interactions. This package is being updated constantly. It is very thorough, well tested and respected.

Whilst I am not an expert on these models, I was able to be certain of their validity through consultation with experienced colleagues.

6.1.2 The Flux Production Methods used within CORSIKA

The flux for each location was created by simulating protons between 1 and 10^5 GeV with a differential spectral index of -2.7, incident on the upper atmosphere, in accordance with the particle data group book (PDG) (see Figure 60 and Reference [42]). It was felt unnecessary to simulate showers originating from primary particles other than protons, since the second most abundant nuclei incident on the atmosphere is helium— which occurs at a rate 1×10^4 times less than protons—and due to the large amount of CPU required to produce the four cosmic fluxes, which would need to be increased dramatically. Primary protons were simulated incident on the outermost edge of the upper atmosphere aproximately 112 km.

The cosmic tests of each ND280 sub-detector were performed on different timescales, with most requiring cosmic fluxes of many million events. This made flux production time a key issue and meant that certain choices had to be made to maximise the validity and quantity of the output flux, while minimising the CPU time required. Whilst it is possible to simulate the primary protons incident on the upper atmosphere over an azimuth of 0–360 degrees and the full zenith range of 0–90 degrees—i.e. the 2π steradians of sky

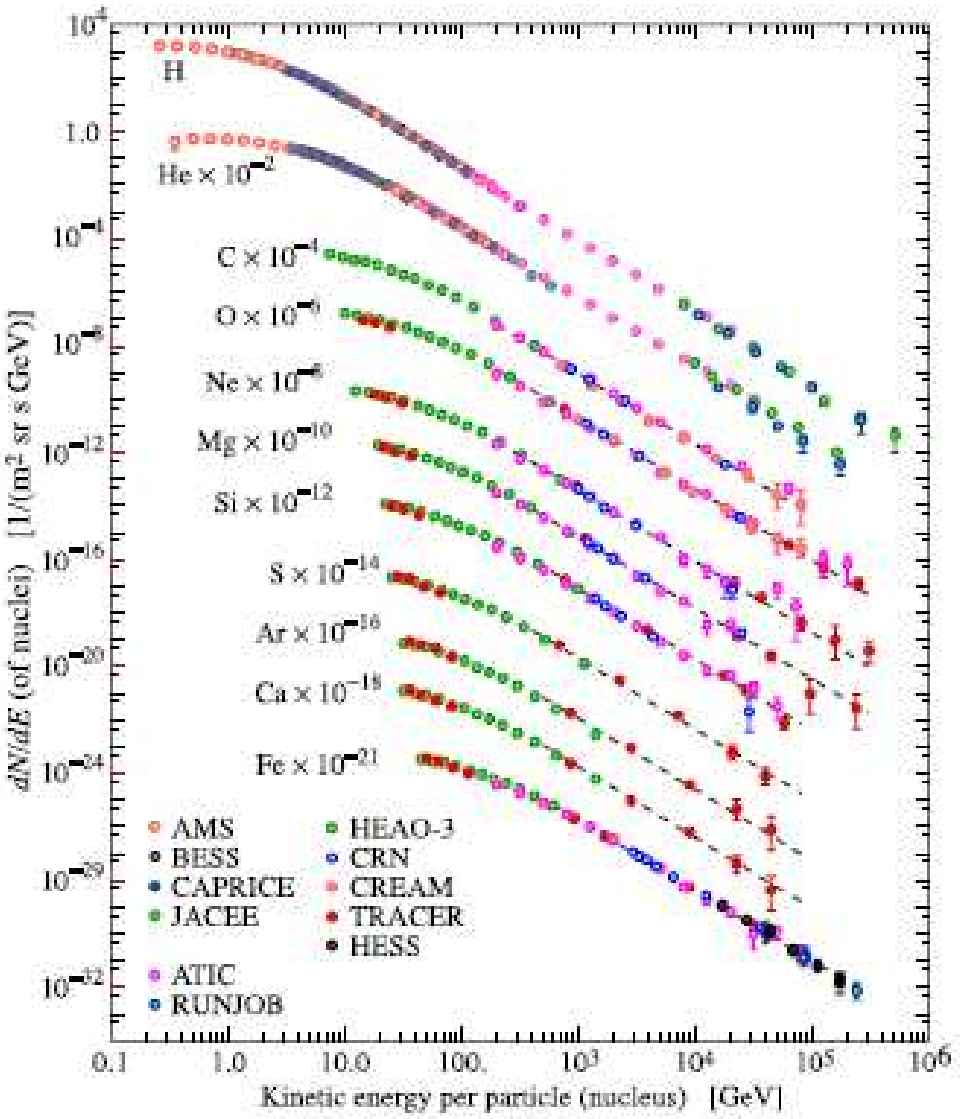

Figure 60: Major components of the primary cosmic radiation according to the PDG [42]. The figure was created by P. Boyle and D. Muller.

overhead— it takes double the processing time which is needed to consider the azimuthal range of 0–360 degrees and a zenith of 0–70 degrees. Since this extra 20% in the zenith produces $< 1\%$ of the total flux of cosmic muons reaching the detector, it was felt that for the calibration and commissioning studies for which the flux was required, the loss of horizontal cosmic rays was worth the gain in time and muon numbers. I later produced a full study of primary protons incident on the upper atmosphere over an azimuth of 0–360 degrees and a zenith of 0–90 degrees—to be used for the cosmic flux in the ND280 pit where cosmic muons with high zenith angles become more important. Both these fluxes are presented here.

CORSIKA maps the path of the incident protons through the atmosphere, the transport and interactions of electrons, positrons and photons, performing the decay of unstable particles, tracking and taking into account ionising energy loss and deflection by multiple scatterings as a result of the Earth's magnetic field. The height above sea level of the detector is also taken into account (simulations of the effect of the buildings surrounding the detector were not considered, as again the increase in time required far outweighed the benefits of so doing). Thus it is essential to produce an independent flux for each of the sub-detector cosmic test locations.

6.1.3 CORSIKA Output

One of the standard file types which the T2K ND280 software can is NUANCE [43]. The main benefit of NUANCE over other data formats in which the cosmic flux could be saved, is that it is human readable, making the files easier to understand and more logical to process. It is also possible to pass such files directly to nd280mc and hence to create ND280 Monte Carlo, easily.

The detector level muons are therefore stored in a NUANCE style file

which records their starting position in m, their direction in $\sin\theta\cos\phi = x$, $\sin\theta\sin\phi = y$ and $\cos\theta = z$ (i.e. spherical polar coordinates) and their energies in MeV. The style of the output is as follows:

```
$ begin
$ nuance ‘‘Event Number’’
$ vertex ‘‘starting position X,  starting pos Y,  starting pos Z’’
$ track  ‘‘13=mu-/-13=mu+,  E MeV,  phiX dir,  phiY dir,  cos theta’’
$ end
```

There is not, as yet, any way to produce such output from CORSIKA directly. I therefore edited the CORSIKA source code to produce the relevant output. These additions have been sent to the authors for possible inclusion in future CORSIKA releases.

6.2 The T2K ND280 Cosmic Muon Data Test Locations and Flux Requirements

Cosmic data taking runs were performed at 4 locations where sub-detector commissioning, calibration, MC-data comparisons and reconstruction tool development took place. The atmospheric thickness, time of year, magnetic field latitude and longitude of each location, as well as the height above sea level of the detector, were specified to ensure the accuracy of the cosmic muon flux produced. Figure 61 shows the effect of the magnetic field on the cosmic flux. It shows the location of primary particles (up to 10 km away from the detector) which go on to produce muons in the detector (where the detector is at the

origin) and shows that there is an off-centre distribution caused by the Earth's magnetic field.

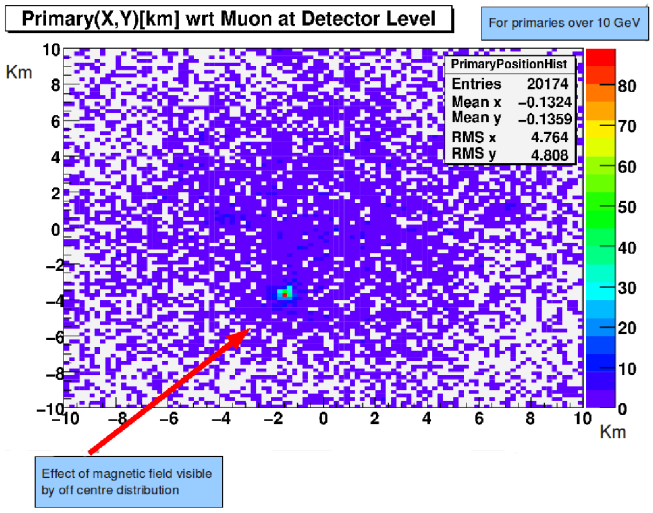

Figure 61: Considering a detector situated at the origin, this plot shows the position of primary particles which go on to produce muons in the detector for protons at a distance of up to 10 km from the detector. It shows that there is a slightly off-centre distribution caused by the magnetic field.

The TPCs and FGDs were commissioned and tested at TRIUMF in Canada. The test took place over several weeks, where several million cosmic muon events were taken. For this reason, a large event sample of cosmic muon flux Monte Carlo was required. It was preferred that this flux was generated directly rather than a smaller flux sample that could then be normalised, to ensure that the flux was as accurate as possible. The test beam at TRIUMF is at latitude: 4914'50.36"N and longitude: 12313'44.99"W and the magnetic field at this location—which was used to produce the flux—was 18.53 microtesla (horizontal component) 51.90 microtesla (vertical component). The detector level was taken as that of the detector hall 10 metres below sea level. The atmospheric model through which the cosmic showers are simulated is that of

US standard atmosphere as parameterised by J.Linsley [44] for mid-April to May, the time of the TPC and FGD cosmic runs. The maximum height of the upper atmosphere at this time is 112.83 km. 26 million muons were produced in the TRIUMF flux.

The Downstream ECal underwent two cosmic tests—the first—primarily for commissioning—was at the Rutherford Appleton Laboratory (RAL) in Oxford, England; the second at CERN in Geneva.

The testing period for the DSECal at RAL was primarily for commissioning and therefore the cosmic data runs taken there produced less usable cosmic events than at the other locations. Therefore the flux produced could also be somewhat smaller than for the other locations. The Earth's magnetic field at RAL is 19.27 microtesla (horizontal component), 14.66 microtesla (vertical component) and the detector level was that of Oxford—129 m above sea level. The closest and most reliable atmospheric model available through CORSIKA, through which the cosmics showers are simulated, was for central Europe (measured above Stuttgart, Germany) in mid January (the time of the cosmics running at RAL). The maximum height of the upper atmosphere is 112.83 km and 28.7 million muons were produced in the final UK RAL flux.

The Downstream ECal underwent extensive testing at CERN using both a testbeam and extensive cosmic muon data taking. The flux produced for the CERN cosmic tests uses the atmospheric model for central Europe (measured above Stuttgart) in mid May. The maximum height of the upper atmosphere is 112.83 km. The Earth's magnetic field at this location is 22.10 microtesla (horizontal component), 41.77 microtesla (vertical component) and the detector level is taken as that of Geneva—375 m above sea level. Many hours of cosmic data were taken at CERN and therefore the flux produced is also of

many millions of events. 23 million muons were produced in the final CERN flux.

The flux produced for J-PARC, Tokai, can be used for the entirety of the ND280 detector and INGRID. The settings are according to the location of the ND280 pit at J-PARC. This flux was produced for US standard atmosphere as parameterised by J.Linsley [44]. The US standard atmosphere was the closest atmospheric model to Japan, nevertheless, since the flux is simulated over a one year period incurring the full range of atmoshperic changes (as cosmic tests will occur regularly at many times throughout the years from now on) this is good enough. The maximum height of the upper atmosphere is 112.83 km. A large event sample was again produced equivalent to a few weeks cosmic running for ND280, thereby ensuring its continued usefulness. The Earth's magnetic field at J-PARC is 30.77 microtesla (horizontal component), 35.02 microtesla (vertical component) and the detector level used is that of the detector hall—1.69 m below sea level. 13 million muons were produced for the Tokai cosmic flux.

The location specific parameters were input to CORSIKA using self produced data cards. These datacards are included in Appendix B, for RAL, CERN, TRIUMF and Tokai, respectively.

6.3 Cosmic Muon Flux Usability and Analysis

The final cosmic flux must undergo a series of validity checks to ensure both its accuracy and that there are no inconsistencies with the known characteristics of a muon flux at ground level. The distributions of primary particles must be examined to ensure that they are behaving as expected according to the CORSIKA inputs selected.

The primary protons which are generated incident on the upper atmosphere should propagate in all directions, thereby producing a distribution of protons with their directions distributed evenly for $-1 < \cos\theta < 1$. I produced a plot of primary proton direction distributions for each flux to ensure that this is the case. Figure 62 shows such a plot for the RAL flux. As we can see, the directions of the primary protons are distributed evenly, as required.

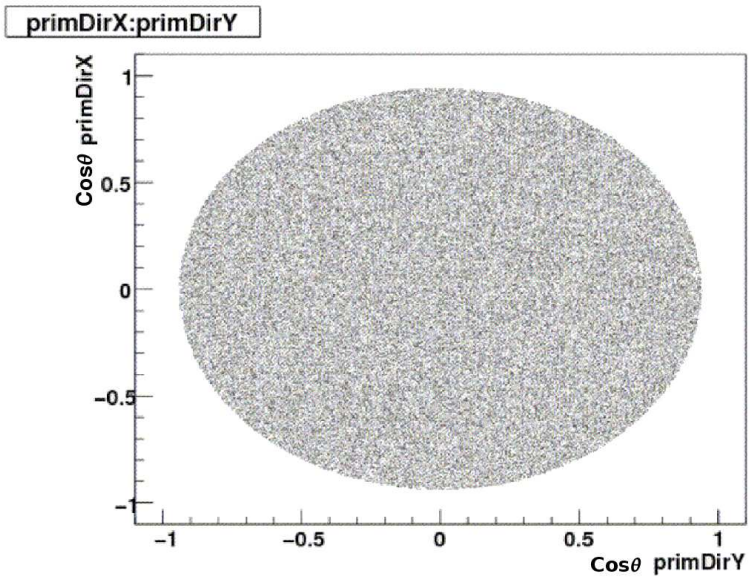

Figure 62: The direction through which the primary protons will propagate from their starting positions, in units of cosθ, where 0,0 is directly downwards vertically and 1,1 and -1,-1 are horizontally.

The directions of the primary protons going on to create muons in the detector are less evenly distributed, with the highest number travelling straight down then decreasing smoothly to the horizon production limit. This can be seen in Figure 63. Low energy protons can be affected by the Earth's magnetic field and so an increase in primary protons producing muons at high zenith angles is observed for primaries between 0 and 10 GeV.

It is also the case that higher energy primary protons travelling at higher

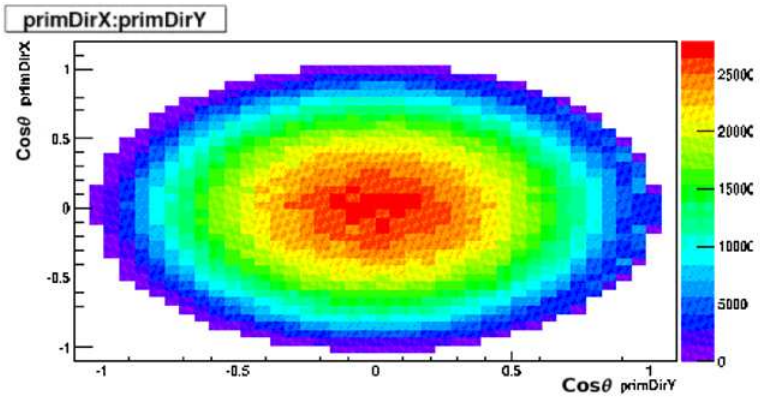

Figure 63: The direction through which the primary protons above 10 GeV going on to make muons will propagate from their starting positions, in units of cos θ, where 0,0 is directly downwards vertically and 1,1 and -1,-1 are horizontally. This plot is for the full 2π steradian flux for Tokai.

angles will often produce higher energy muons. This is demonstrated in Figure 64 again for the RAL cosmic flux. The distribution shown is within expectations.

The subsequent flux of cosmic muons is then considered to ensure its validity, where many quantities are checked and plots of the primary and secondary particles are examined, such as shown here. The energies of the muons must each be above 105 MeV, the rest mass of the muon, since the energies in the flux are total energy. The distribution of muon directions should be evenly distributed, meaning that the RMS of muon direction should be roughly 0. Therefore it is required that $0.99999 > \sqrt{(x^2 + y^2 + z^2)} < 0.00001$ where x, y and z are $\sin\theta\cos\phi$, $\sin\theta\sin\phi$ and $\cos\theta$ respectively.

The ratio of $\mu^+/\mu^- = 1.3$ is a characteristic of the total cosmic muon flux and hence is required by the final validation. However, the full story is a lot more interesting. This ratio depends on the energies of the primaries which produce them and the distance of atmosphere through which they have had to travel to reach the detector. Primary protons arriving at the upper atmosphere

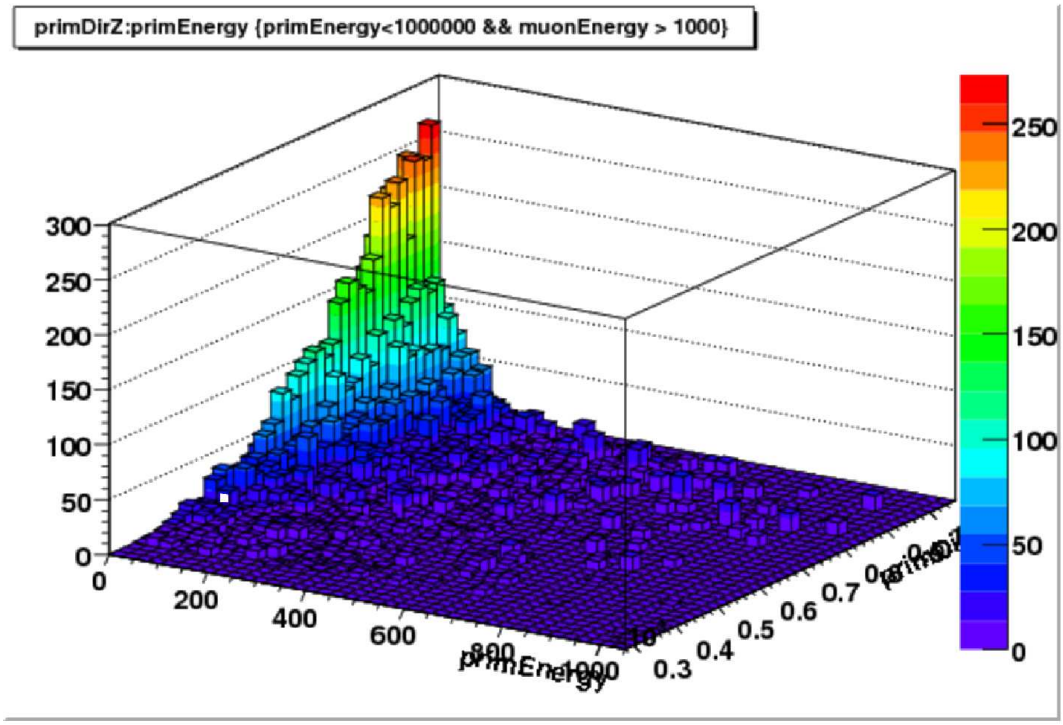

Figure 64: $\cos\theta$ versus energy in GeV for primaries under 1000 GeV which produce muons above 1 GeV at detector level. This plot is for the RAL cosmic flux and shows primaries over 10 GeV.

from almost overhead, at low primary proton energies 1–10 GeV, will produce a μ^+/μ^- ratio of around 2, dropping to around 1.366 for primary protons in the range 10–100 GeV, whilst at higher proton energies of 1×10^3–1×10^4 and 1×10^4–1×10^5 the ratio μ^+/μ^- becomes 1.03 and 0.96 respectively. Likewise, muons arriving in the detector from primary protons produced through a zenith angle of 0–90° and or 0–70° will have the μ^+/μ^- ratio 1.3, whereas primary protons incident on the upper atmosphere between zenith angles of 70-90° will produce a μ^+/μ^- ratio around 1.99.

6.4 T2K ND280 Sub-Detector Cosmic Tests - Using the Flux

The ND280 cosmic flux which I produced was used by many of the ND280 sub-detector groups to tune the reconstruction and analysis software of their detectors and for cosmic data and Monte Carlo comparisons during their cosmic data taking calibration runs. Some of these tests and results are presented here. The DSECal cosmic studies are presented in Chapter 7.

6.4.1 INGRID Cosmic Tests

Cosmic tests were performed by the INGRID sub-detector group at ground level in Tokai for all 16 modules of the INGRID detector. The cosmic flux which I produced for J-PARC was used to compare with the cosmic data, for use in detector calibration and commissioning, and for testing the INGRID reconstruction software.

The cosmic flux was used to tune and test the method by which the INGRID sub-detector group veto hits. Each INGRID module is surrounded by veto planes which are shown in Figure 65. These are used to reduce noise. The

veto cut works so that once a track is reconstructed, the code projects the track position on each veto plane and looks to see if there is a hit within a tolerance of ±2 scintillator plane. If the veto hit has Z < the Z vertex, then the track is said to be vetoed, (see Figure 66). In the future, a time correlation will be added: the veto hit will have to be within ± 50 ns of the reconstructed time of the event.

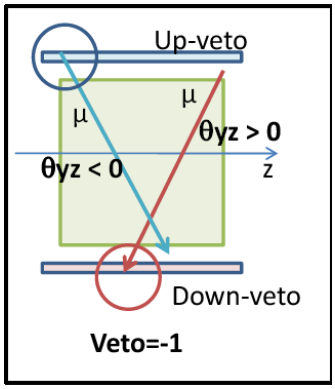

Figure 65: The central green square represents any of the 16 INGRID modules whilst the blue rectangular regions above and below represent the upper and lower veto planes [45].

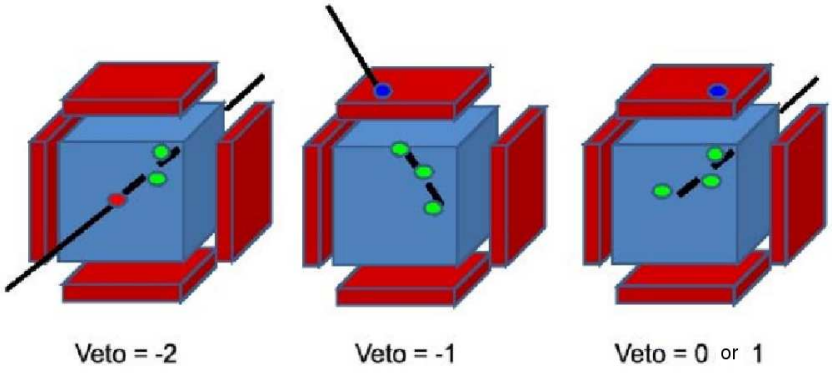

Figure 66: A track is vetoed if in INGRID "veto" < 0, where: veto = −2: hit on the first plane of the module ("front veto"), veto = −1: hit on a veto plane—upstream and compatible in the direction of the reconstructed track, veto = 0: no hits in veto planes, veto = 1: hits in veto planes not compatible with the reconstructed track [45].

The angular distributions of muons in 2 dimensions (see Figure 67) were compared for cosmic MC and data without the pit simulation —including and excluding the veto cut—and were found to agree in all cases (see Figure 68).

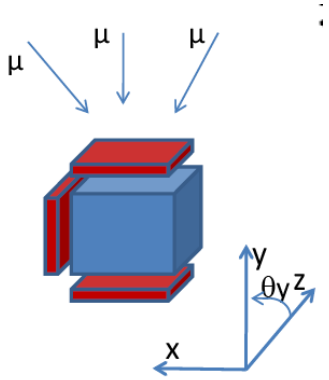

Figure 67: Incoming muons at INGRID are considered in 2D planes in θ_{xy} and θ_{yz} as shown [45].

The INGRID sub-detector group also performed a simple GEANT simulation of the pit—using soil (O + Si), density=1.8 g/cm^3 and pit (concrete), density=2.2 g/cm^3. They found low energy tracks to be suppressed by the pit. Once again they compared the 2D angular distributions of MC and data (with and without veto) and once again found good agreement, as can be seen in Figure 69.

The work of the INGRID group in this area demonstrates the usability and accuracy of the Tokai cosmic flux which I produced.

6.4.2 TPC Cosmic Tests

The cosmic flux was used by the TPC group to tune its reconstruction software to real data and improve the cosmics trigger. Figure 70 shows an early stage in the process, when TPCRecon was reconstructing cosmic MC tracks, but unable to reconstruct cosmic data.

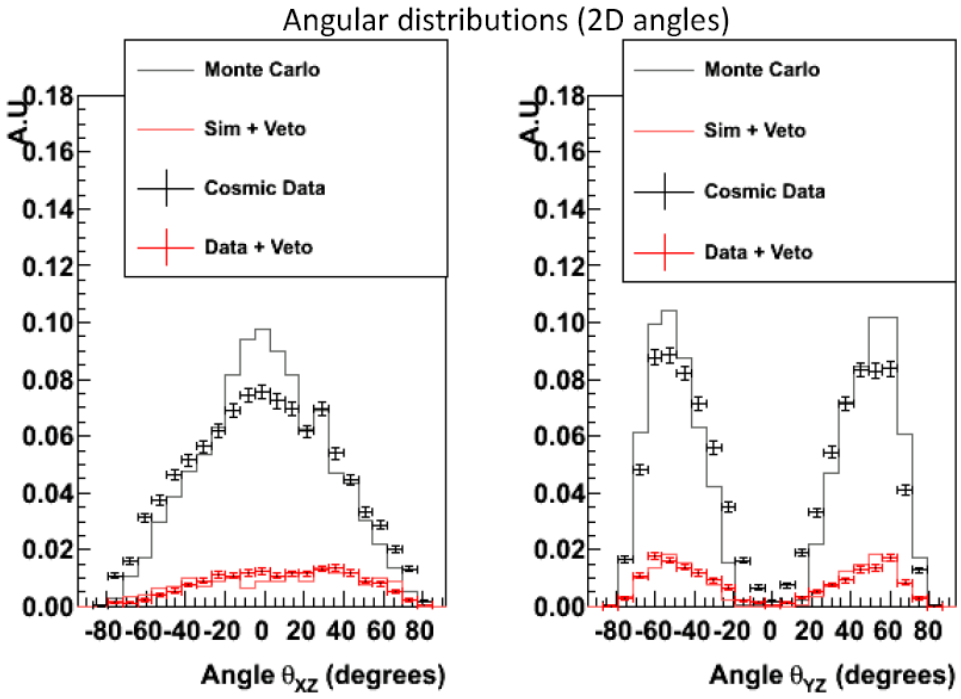

Figure 68: Angular distributions of cosmic muons (not including the simulation of the pit) as seen in INGRID in 2D—with and without veto cut—where continuous lines represent Monte Carlo and crosses represent data. The agreement is seen to be good eneough in all cases [45].

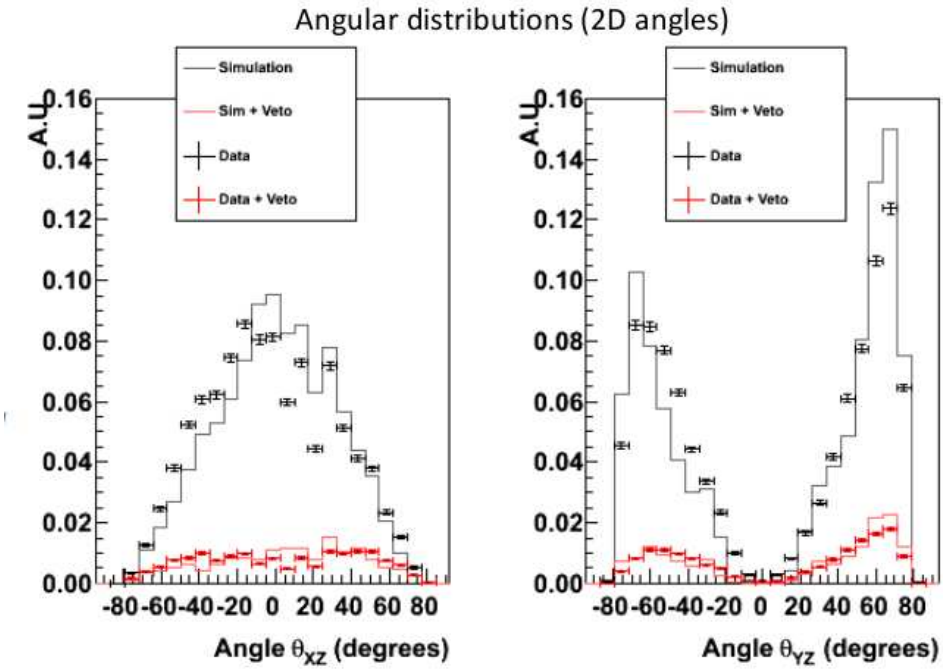

Figure 69: Angular distributions of cosmic muons (including a simple pit simulation) seen in INGRID in 2D—with and without veto cut—where continuous lines represent Monte Carlo and crosses represent data. Angular asymmetries are observed due to low energy cosmic tracks interacting in the pit—the first module is not yet located in the center of the pit. Good agreement is seen in all cases [45].

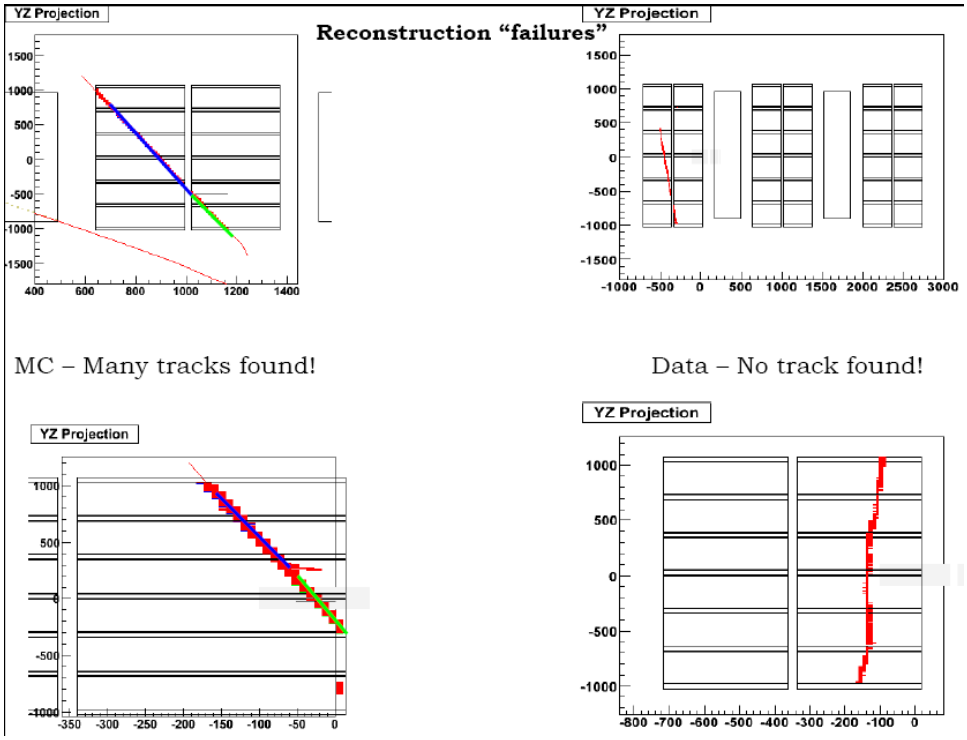

Figure 70: TPCRecon reconstruction comparisons failures between cosmic MC (left) and data (right) [46]. This is an early version of the reconstruction—which is now working well.

Following this study, TPCRecon is now accurately reconstructing cosmic tracks.

6.4.3 MPPC and elecSim Cosmic MC Data Tests

The sub-detector's response and the electronics of ND280 are simulated in the elecSim software package which was explained earlier in Section 5.1.2. The ND280 cosmic flux which I produced was used by collegues at Imperial College London to tune the MPPC response.

Figure 71 shows the charge comparison between cosmic data and MC for the MPPCs, showing calibrated MC and data hits and elecSim hits. They compare well with two visible inconsistencies; the first at 10 pe is yet to be understood, the second at 40 pe is the effect of the range switching in the TFBs (range switching is an effect of the algorithm which determines the way in which the low and high gain ADC values are used together to calculate the charge of a hit).

A 30% difference in dE/dx width between data and MC was observed in Figure 72. For data, scintillator bar light yield is affected by the position of the track in the bar, while the MC assumes a constant photon per MeV/cm/MIP value of 25.0. This is the cause of the difference.

The MPPC response compares well between data and MC, but will continue to be tuned and improved using cosmic data and the cosmic MC which I produced to ensure the best possible accuracy of the elecSim package.

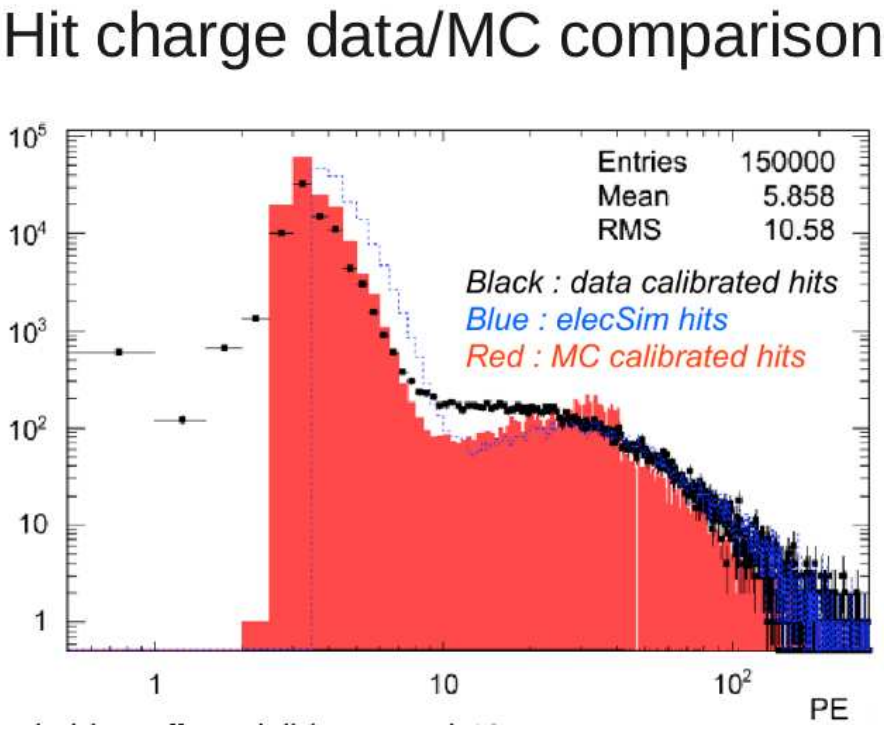

Figure 71: The MPPC determined hit charge of calibrated cosmic MC (red), calibrated cosmic data (black) and elecSim hits (blue), in pe The data compares well but with two inconsistencies, the first yet to be explained at 10 pe, the second at 40 pe shows the effect of the range switching [47].

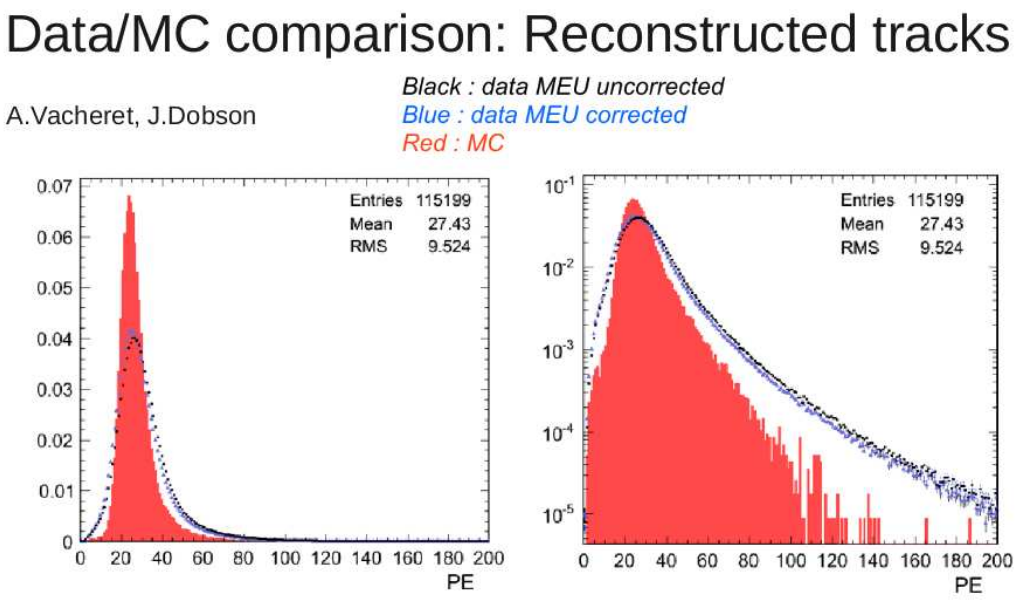

Figure 72: The dE/dx for calibrated cosmic MC (red) and calibrated cosmic data (black), in pe A 30% difference in dE/dx width between data and MC is observed due to the way that the light yield of the bar is treated in MC and data. This plot was produced by [47].

6.5 T2K ND280 Cosmic Flux with Full Zenith Angle Simulation

I produced a further cosmic flux for primary protons incident on the upper atmosphere for the full hemisphere above the detector i.e for an azimuth of 0–360° and a zenith of 0–90°. It takes significantly more computing time to produce a flux covering zenith angles including 70–90°, and it was not necessary for initial sub-detector cosmic testing and calibration. However, for future cosmic tests in the ND280 pit it does become necessary, since these near horizontal muons are the main contributor to sand muons—secondary muons produced in the sand and the walls surrounding the pit.

This 0–90° zenith angle flux was again produced using CORSIKA. The co-ordinates, magnetic field and atmosphere were as for the previous Tokai

flux.

It is interesting—and indeed necessary—to consider the distributions of muons and primary protons in terms of their energies and directions in order to understand the flux fully. The distribution of the directions in x and y through which the primary protons incident on the upper atmosphere which go on to produce muons at detector level, is an example of something that should be plotted and considered. It can be seen that for primaries over 10 GeV, which are not so affected by the Earth's magnetic field, most will be travelling straight down—seen as the origin on Figure 63.

The energy versus direction in z i.e. $\cos\theta$ for primary protons (of the produced flux) should also be examined. This again behaves as expected, with most particles travelling straight down ($\cos\theta = 1$) at lower energies, while higher energy primaries are able to produce detector level muons from more obtuse angles. See Figure 73.

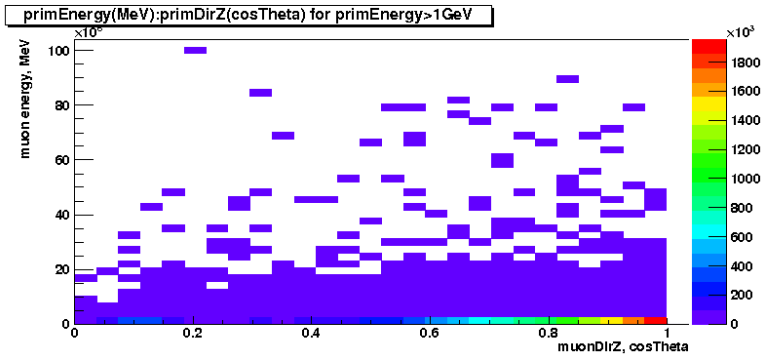

Figure 73: The energy versus direction in Z i.e. $\cos\theta$ for primary protons which go on to create muons at detector level. $\cos\theta = 1$ for protons travelling straight downwards.

The next thing to consider is the final muon flux, irrespective of the parent particles. The directions in x and y through which the cosmic muons travel to reach the detector are seen to be as expected and can be seen in Figure 74.

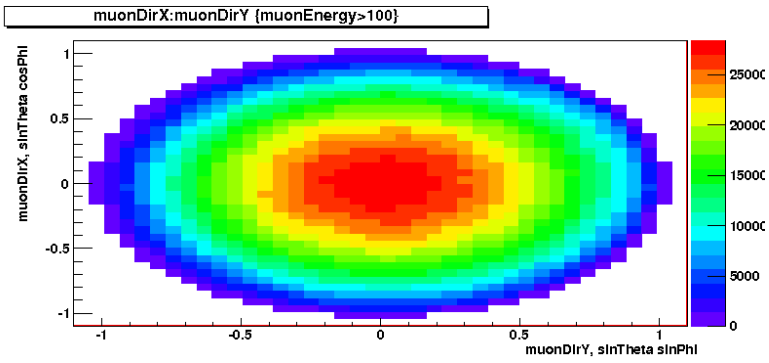

Figure 74: The muon directions in $x = \sin\theta\cos\phi$ and $y = \sin\theta\sin\phi$ for cosmic muons at detector level. The origin shows muons travelling straight downwards.

The muon energy shows a smooth distribution as can be seen in Figure 75.

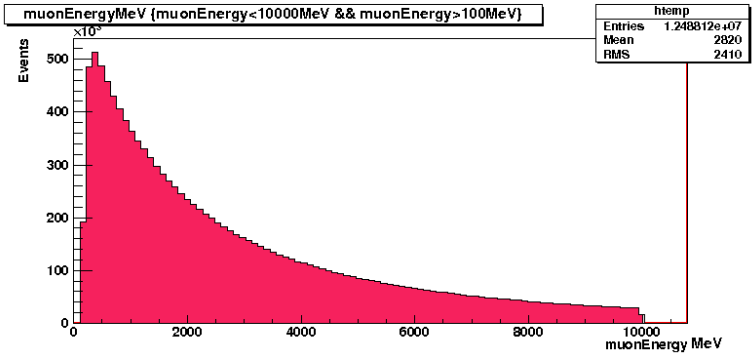

Figure 75: The total energy of cosmic muons in the detector, for muons below 100 GeV.

The overall μ^+/μ^- ratio of the 0–90° zenith angle cosmic flux is 1.3 as expected; however, once again it is interesting to consider the ratio of muons produced from primaries generated in the 70–90° zenith region, where 90° = horizontal. Here I observed a μ^+/μ^- ratio of 1.99. This is due to the increased distance which the muons must travel through the Earth's atmosphere to reach the detector, causing the μ^-'s to be further depleted.

The direction in x and y travelled by the muons produced from primary protons impacting the atmosphere in the region from zenith angles of 70–

90° depends heavily on the energy of the muons. This is due to the Earth's magnetic field having a greater effect on low energy muons. This effect can be easily observed through the comparison of the muon directions at varying energies. Figure 76 shows the travelling directions in x and y of the total flux of cosmic muons in the 70–90° zenith angle region. There are—as expected—more muons arriving from the horizon, but still many arriving from overhead (due to cosmic showers that have propagated through the atmosphere and scattered downwards above the detector). However, there is a definite increase in the number of muons on the right hand side of the plot, i.e. more muons arriving from one side of the sky, as can be seen in Figure 76. This is the effect of the magnetic field and can be demonstrated through consideration of the travelling directions in x and y of muons of different energies.

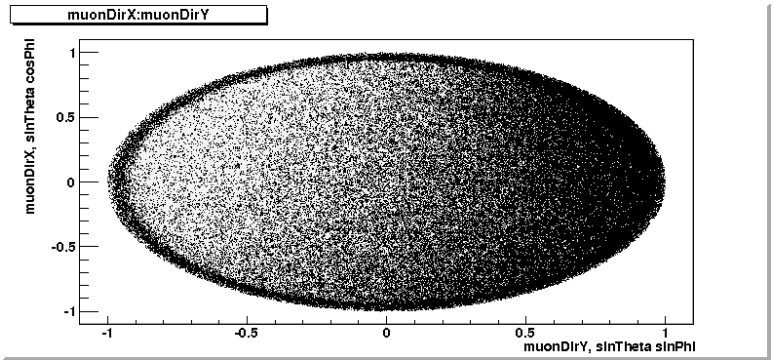

Figure 76: The travelling directions in x and y for all energies of muons—produced from primary protons produced in the zenith angle range from 70–90°, with 90° being horizontal. The directional bias should be noted, along with the fact that muons will still propagate through the atmosphere to an overhead position and travel downwards to detector level from there.

For high energy cosmic muons above 20 GeV, the central region (that of muons arriving from overhead) disappears—since muons are very high energy and therefor tend to travel further without undergoing internal atmospheric scattering, and the directional bias also disappears—since high energy muons

are less affected by the Earth's magnetic field (see Figure 77).

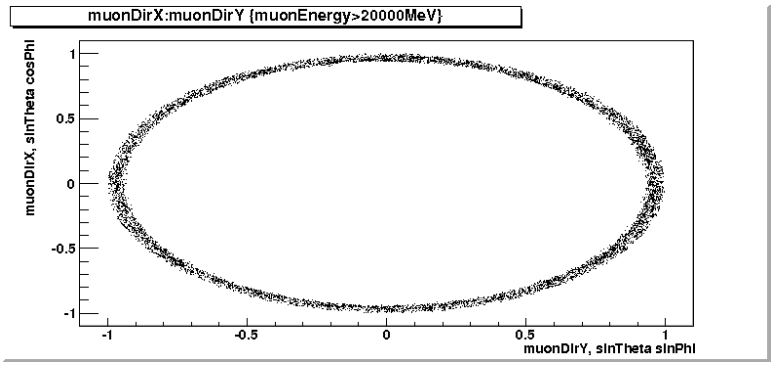

Figure 77: The travelling directions in x and y for muons of energy greater than 20 GeV—produced from primary protons produced in the zenith angle range from 70–90°, with 90° being horizontal. The directional bias can no longer be seen.

At low muon energies below 1 GeV, however, the distribution shows only the directional bias caused by the Earth's magnetic field and the muons arriving from all directions overhead. This is due to these low energy muons being more susceptible to atmospheric and magnetic affects.

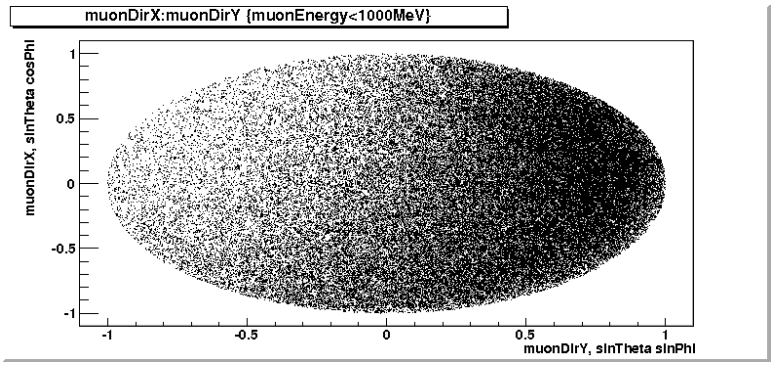

Figure 78: The travelling directions in x and y for muons of energy less than 1 GeV—produced from primary protons produced in the zenith angle range from 70–90°, with 90° being horizontal. The directional bias is clearly evident and the high numbers of horizontally travelling muons are no longer seen, showing the affect of the Earth's atmosphere and magnetic field on these low energy muons.

6.6 Conclusions

I produced the cosmic muon MC flux for the T2K ND280 collaboration, including all its sub-detectors, using CORSIKA. This flux is the official ND280 cosmic flux and was used for the commissioning and calibration of all ND280 sub-detectors to tune the general simulation and reconstruction tools such as the elecSim software package and to tune and test the MPPC linearity response and reconstruction (which is necessary for all ND280 sub-detectors except for the TPC).

I produced five fluxes in total to meet the various needs of the collaboration. A 0–70° cosmic flux was produced for four locations where cosmic muon tests were carried out, namely: RAL (UK), CERN (Switzerland), TRIUMF (Canada) and J-PARC (Japan). The final flux included the full range of zenith angles from 0–90° which takes a lot more CPU time to produce, but becomes necessary for detectors in-situ in the ND280 pit, due to the high zenith angle muon's contribution to sand muons.

The 0–90° cosmic flux which I have produced will be used to produce a large scale cosmic pit MC simulation which will be used for all future studies including ND280 cosmic MC. This will include simulations of the sand muons (which will be produced by the SMRD sub-detector group) and full cosmic triggers for each ND280 sub-detector. This is one of the major goals for the mid to late months of 2010 and will therefore not be ready in time for inclusion here.

It is the current intention of the T2K collaboration that the T2K ND280 flux which I have produced will be used for all near detector cosmic studies for the duration of the T2K experiment.

7 Calibrating the Electromagnetic Calorimeter of ND280

Calibration is an essential part of any particle physics experiment. It is through calibration that detector performance and response is understood, and experimental errors are minimised. The ECals of T2K are each to be calibrated, particularly the DSECal, the first to be built and installed. The DSECal underwent three stages of commissioning and calibration: first, for four weeks at the Rutherford Appleton Laboratory—this was mainly for detector commissioning and to implement the readout software. Cosmic muon data was also taken and while not accurate enough for calibration, since it was taken before commissioning was complete, it was used to tune the readout software and commission the electronics. The second stage was an eight week cosmic muon and testbeam data taking run at CERN in Geneva—it is mainly this data which is used for detector calibration. Finally, the detector was then run in cosmic mode again in Tokai, both before and after installation in the ND280 pit—it was during this time that the problems which had come to light in the earlier calibration tests were corrected and the detector was tested again. In this way the DSECal was installed in the pit, well understood and working well. Unfortunately, due to funding constraints, it is not possible to test any of the other 12 ECal modules in a testbeam. Since all the detectors use the same WLS fibres and similar scintillator bars (though different lengths) as well as the same MPPCs, TFBs and RMMs, many of the lessons learnt with the DSECal can help with the commissioning of the subsequent ECal modules. This makes the CERN testbeam and cosmic running time all the more important.

The rest of this chapter describes the use of the cosmics data for detec-

tor calibration and my role as leader of the UK cosmic muon analysis effort, while providing a more detailed look at the DSECal CERN testbeam cosmics running. In particular, I will describe my work performing the attenuation correction of the DSECal and future ECal modules and comparisons between cosmic MC and data.

7.1 Calibration using Cosmic Muons

Cosmic muons are arguably the best way to calibrate any detector. They (mainly) travel in straight tracks which means that they are easier to reconstruct, they are usually through going—rarely interacting within the detector—and they populate across the whole detector since they come from all directions which means that all parts of the detector can be examined. These are the reasons why cosmic data was used to perform much of the calibration of the DSECal.

I lead the UK cosmic muon analysis effort for the DSECal. A group of more than 15 collaborators—lecturers, postdoctoral researchers and students, whose remit was to use the cosmic data to calibrate the DSECal, to test the ND280 software tools, to tune the reconstruction and analysis tools, and analyse the detector response. My responsibilities were to co-ordinate the work effort of the group, run regular meetings and to present and justify the work of the group to the collaboration as a whole.

The group used the cosmic muon data from the initial RAL tests to commission the DSECal, and the CERN testbeam cosmic data taking runs to calibrate and tune the reconstruction and analysis software. MC and data was used for comparison and testing throughout. The tasks involved are described below.

The hardware cosmic trigger was finalised shortly before the start of the RAL commissioning tests and was needed to be implemented in the code so that it could be taken into account when producing cosmic MC in the software.

Timing corrections between the MPPCs at each end of the bars—comparing the time recorded for a hit in a given bar by the MPPCs at each end and then correcting for inconsistencies—were performed.

The position estimation per bar was greatly improved by the comparison of the estimated position of a cosmic muon hit along a bar from the time and charge information recorded by each of its MPPCs with the fitted position (from track reconstruction) of the hit, then combining this information to improve the overall position resolution. To do this, the average speed of light along the WLS fibres within the bars was calculated to be 174 mm/ns, which enabled the time of each hit recorded at each bar end to be extrapolated back to give a position for the hit giving a position resolution of 22 cm; the charge information was also used giving a resolution of 47 cm. Combining these techniques gave a resolution of 20 cm with negligible bias which was used to improve the 2D and 3D cluster matching in ecalRecon. In this way—amongst others—cosmic muons were used to improve the clustering efficiency and the particle identification (PID), both in the reconstruction software and in the electronics simulation package elecSim.

Hit maps of cosmic muons are very useful in detector testing; they demonstrate hot, dead or swapped channels (MPPCs) and problems with electronics readouts. Hit maps proved especially useful when testing the DSECal using cosmic muon data taken at CERN, as two TFBs were found to be dead. I—and two other members of the cosmic muon analysis group—independently produced hit maps for the DSECal and found 100% concurring results. In

Figure 79 the hatched region on the top right of the plot clearly shows where the broken TFBs (which instrument the Y orientated bars) are not recording any hits. This affects layers 20–34, bars 34-50. A schematic showing the DSECal's orientation and what the bar and layer axis mean in these terms is shown in Figure 80.

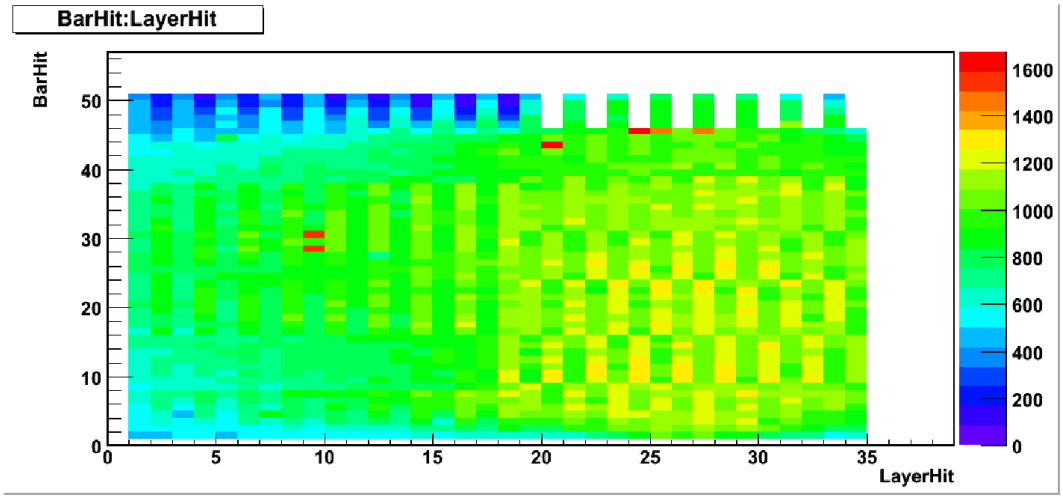

Figure 79: Hit map showing cosmic muon events in the bars (y axis) and layers (x axis) of the DSECal from cosmic data taking at CERN summer 2009. The hatched region of no hits in the top right corner of the plot, shows the position of two broken Trip-t Front End boards. These boards were later replaced on site at J-PARC.

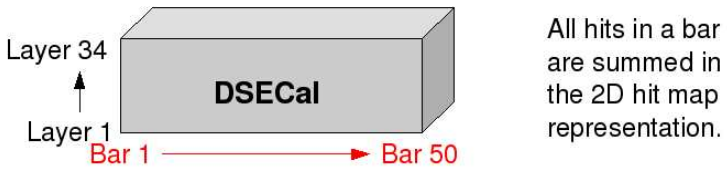

Figure 80: Schematic to show the orientation of the DSECal for the cosmics testing—demonstrating where on the module the bars and layers shown in the hit maps are. The DSECal was facing downwards as shown.

Luckily, as this was the very top left corner of the detector (in upright position), this region was above that recording the testbeam events and so

did not affect data taking. The two broken TFBs were replaced at Tokai and are now working well. Ten dead channels (highlighted by the black circles in Figure 81) and some "hot" (significantly overactive) channels (which can be seen as red or orange squares in Figure 81), were also unanimously observed from the hit maps. Many of the channels that were seen to be hot were corrected by altering their gain or HV trim. 11 channels were finally found to be dead and will be corrected in the future.

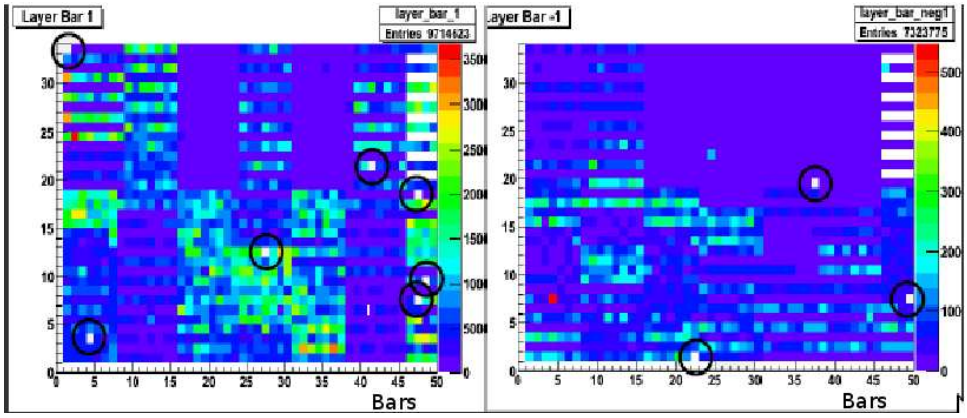

Figure 81: Hit maps showing cosmic muon events by readout end (left and right plot), in the layers (vertical axis) and bars (horizontal axis) of the DSECal from cosmic data taking at CERN summer 2009. The black circles show dead channels while, hot/overactive channels can be seen in red and orange.

Stopping muons often produce Michel electrons, which, as they shower, can be misidentified as electrons from electron neutrinos. These Michel electrons are useful for tagging the muons and decay pions creating them; they are seen in the detector as small, but visible energy deposits near the end of the muon/pion cluster. After investigation, the requirements for ID which are used to tag such events in ecalRecon are: that the energy deposit occurs at a later time than the muon/pion cluster; that the energy deposit are between 2.5 and 40 MeV (as can be seen from Figure 82) and that they have less than 11 hits and be within 80 mm of the parent cluster (as can be seen from Figure 83).

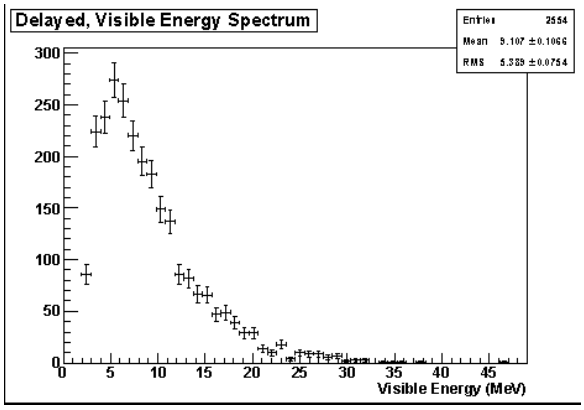

Figure 82: The allowed energies of an energy deposit caused by Michel electrons produced by stopping muons in the DSECal, see Reference [48].

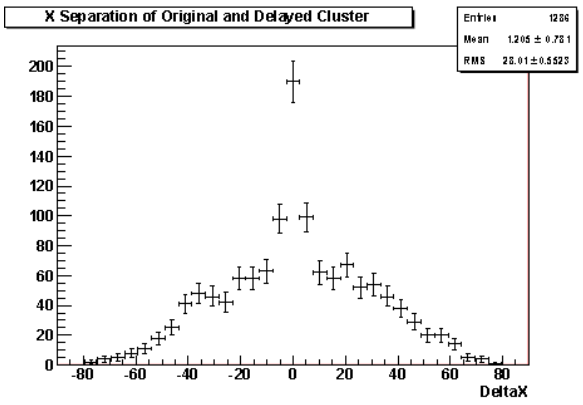

Figure 83: The distance from the parent muon/pion (right) of an energy deposit caused by Michel electrons produced by stopping muons in the DSECal, see Reference [48].

Since the scintillator bars of the DSECal are 2 m long and read out by WLS fibres, the attenuation length of light within these bars is an important factor in the calibration. The attenuation correction constants are needed for each bar and each MPPC in order to improve the accuracy of the detector. Together with G.S.Davies of Lancaster University, I performed the attenuation correction, along with the initial comparison between MC and cosmic muon data, I then performed the final comparsions and analysis. Both of which tasks are described in detail in the following sections.

7.2 Performing the Attenuation Correction for the Bars of the Electromagnetic Calorimeter

7.2.1 Motivation and Purpose

One physical process which affects the energy calibration and needs to be corrected for is the attenuation of light as it travels along each bar. We know that light attenuates along the WLS fibre and, remembering that they are 2 m long in the DSECal, we need to measure the extent of this attenuation. The calorimeter response needs to be understood and light attenuation is one aspect of its response which needs to be corrected in order to achieve inter-calibration of the scintillator bars and a normalised energy response across the DSECal. A position dependence in the calorimeter response is caused by the effects of light attenuation. The attenuation correction can be parameterised by a short and a long attenuation length. The short attenuation length was previously observed to be relevant at distances less than around 60 cm from the MPPC while the long attenuation length was observed to be relevant for the full length of the fibre. The parameterisation of the attenuation correction we used is shown in Equation 7.2.1.

$$R \times (\exp^{(\frac{x}{\lambda_s})}) + N \times (\exp^{(\frac{x}{\lambda_l})}) \tag{22}$$

where λ_s = short attenuation length, λ_l = long attenuation length, R = Ratio and N = Normalisation.

The light attenuation is caused by several factors, including self-absorption and reflection losses in the WLS fibre. By definition, light attenuation is the reduction in intensity of the light signal with respect to the distance the light has travelled between the point of generation and the point at which it is converted into an electric signal. Consequently, the position dependence in the calorimeter response arises from light attenuation effects and from other factors such as the effects of the fibre-to-sensor coupling (where different wavelengths depend on the radial positions).

7.2.2 Event Selection

In order to perform the attenuation correction, it is necessary to work with raw data which has not been through the reconstruction. It is also necessary to select through-going muons which form straight tracks through the detector, so that the position of each hit on a given bar can be adequately estimated. We therefore use data with events triggered on cosmic rays for this purpose. One through-going muon track is selected for each cosmic data event. On occasions, where the event contains more than one muon track, the highest charge track is selected.

The DSECal has 34 layers, each with bars orientated perpendicular to the next, of 50 2 m × 2 m scintillator bars which are readout by an MPPC at each end (double ended read out). The attenuation correction is calculated

for each photosensor of every bar. Each bar is subdivided into 50 4 cm virtual subsections which will be referred to from now on as pixels. The first and third of these pixels are 1 and 3 cm wide respectively and due to the nature of the trcak finding algorithm no hits will fall in either. As the muon track travels through the detector, each of its hits will fall in a particular pixel of each bar which it traverses. The pixel in which a given hit falls is determined according to the position of the hit in the layer above and the layer below the hit in question. Due to the alternating layer orientation structure of the ECals, this can be done by considering the bar number of the layer above and below which received a hit of the selected track and then finding the pixel located between the bar positions:

$$P = (\frac{L_a + L_b}{2}) + 1, \tag{23}$$

where P is the pixel, L_a is the bar number of layer above and L_b is the bar number of layer below.

A muon hit in a given bar will have a distance, from the photosensor in question, equal to the position in centimetres of the centre of the pixel traversed, with an error of $\pm$ 2 cm.

Figure 84 shows the process we used to determine which pixel receives a hit for a given bar of layer x. It shows a through going muon track represented by the dashed blue line, traversing bar 3 of the layer above and bar 7 of the layer below layer x. This results in a hit in the bar in question in pixel 6 (according to Equation 7.2.2), which is equivalent to a position of 19 $\pm$ 2 cm.

We select the highest charge hits in a given event to belong to the same track, in order to get just one muon track per event. It is then clearly necessary

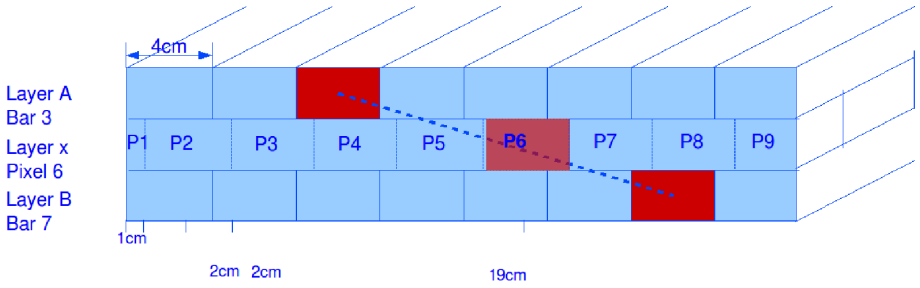

Figure 84: A muon traversing the detector is shown by the blue dashed line and the brick like structure of the ECal is shown. We are interested in the bar of layer x (in the middle of the diagram), the pixel through which the track travels is determined from the bar of the layer above (Layer A) and the bar of the layer below (Layer B), shown in red, which receives the hit. In this case, the hit in the bar in question occurs in pixel 6.

to ensure that all hits of a given track are definitely part of the track and not—for example—a high charge noise hit (since it is the highest charge hits which are selected to form the tracks). This is done by considering the layers 2 and 4 layers above and below the layer of the hit in question in turn, and then checking that the hits of this track all fall within ± 5 bars of the pixel in which the hit was observed. If any hit should fail this condition, then the hit which has the next highest charge and is in the same layer is selected and required to meet the same condition. Should this condition still not be met, then no hits are associated with the track on this layer of the detector for this event (see Figure 85). This method does reduce the statistics by around 30% but improves the purity for associating hits to tracks (which is defined as the fraction of selected hits which are associated to the selected track) by around 40%. In very close to 100% of the tracks finally selected using this method, all hits were associated to the track.

This track finding and hit positioning method is validated by printing the layer bar and pixel number of each hit for a set of selected tracks and either

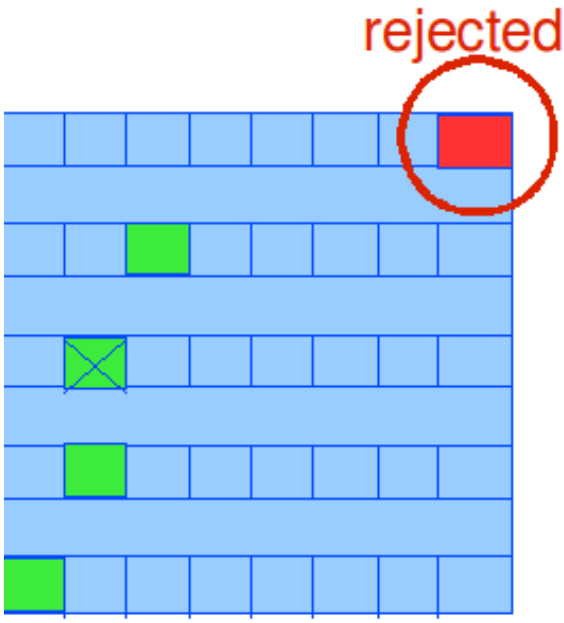

Figure 85: A 2D schematic of the ECal showing 4 hits which are selected to belong to the same track (highlighted) and one hit which is selected as part of the track, but then rejected for being too far away from the other hits, circled. In this case, there will be no hits associated with the track in the topmost layer of the diagram.

ensuring by eye that each hit is falling along a track-like route, or, by comparing the hit positions with the track viewed, in an event display. Figure 86 shows such a process for a certain muon track. The position of each hit matches exactly with that shown in the event display—showing that the method has worked.

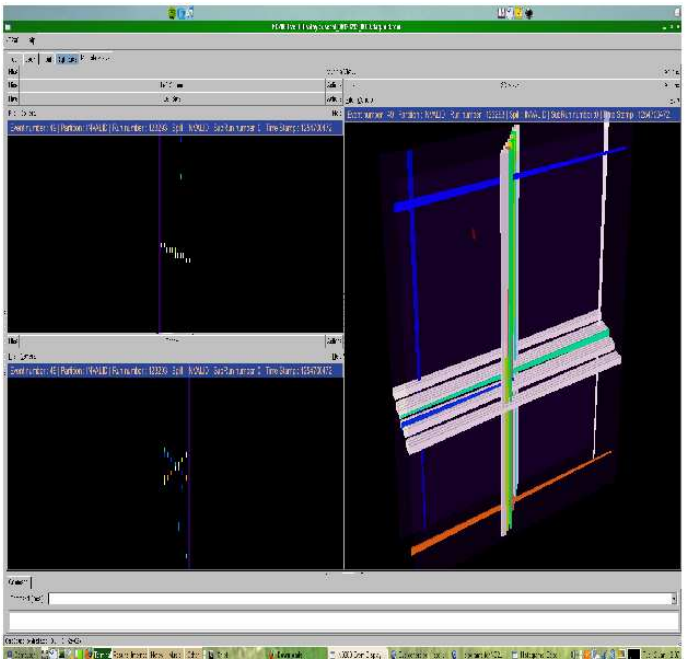

Event Number in ev loop: 49
dsecal_12393_0000.daq.mid
Pixel: 18 L1 B 29
Pixel: 28 L2 B 18
Pixel: 18 L3 B 28
Pixel: 28 L4 B 18
Pixel: 18 L5 B 28
Pixel: 27 L6 B 18
Pixel: 18 L7 B 27
Pixel: 27 L8 B 18
Pixel: 18 L9 B 27
Pixel: 26 L10 B 19
Pixel: 19 L11 B 26
Pixel: 26 L12 B 19
Pixel: 19 L13 B 26
Pixel: 25 L14 B 19
Pixel: 19 L15 B 25

.....

Figure 86: Left: event display showing a single muon passing through the detector—the angle of the track can be clearly seen from the highlighted bars which it traverses. Right: the pixel, bar and layer number of each hit (with blue and black representing the orientation of the layer). This shows an exact match with the event display of the same track.

Finally, the charge is corrected for the path length of the track, since there is a difference in the energy deposited in the detector if the muon travels straight downwards through the centre of a bar, from when it passes the bar while travelling at a higher angle. This correction is implemented in the form of a simple $\cos\theta$ correction, where the absolute value of $\cos\theta$ is multiplied by the charge of the hit, thereby lowering the recorded charge deposited by clipping

muons in the bar in line with what is seen. If a hit has a charge value of less than 10 pe that hit is not included in the track as such hits skewe the charge distributions in an unatural way and are therefore most likely to be noise hits.

7.2.3 Method To Extract The Attenuation Correction Constants

The hit selection algorithm described above was used to select through going cosmic muon tracks in the DSECal and record the layer, bar and path length corrected charge information of their constituent hits. The attenuation correction was first made using the cosmic muon data taken during the DSECal CERN testbeam cosmic running, and later, cosmic data taken at Tokai before the DSECal was installed in the ND280 pit was also used. The CERN data is presented here, while the attenuation correction for the Tokai cosmic data is described and compared with the CERN data in Section 7.3.1. In order to have the highest statistics possible, the full CERN cosmic data set of 300 files each of 15k cosmic ray trigger events was used.

The charge spectrum for each pixel is fit with a convoluted Landau-Gaussian function and the Most Probable Value (MPV) is found from the fit. Some example charge spectra for three pixels of a given bar are shown in Figure 87. As the position of the hit moves further from the MPPC detecting it, the mean calibrated charge in photoelectrons detected decreases. The Landau-Gaussian fit is also shown along with the MPV value. A Landau-Gaussian is used to fit the data since the Landau represents the energy loss distribution in the limit of thin materials, while the Gaussian accounts for the smearing due to the thickness of the material.

The MPV value for each pixel is then plotted as a function of the position of the hit along the bar in centimetres. The position is calculated from the pixel number to an error of ± 2 cm. In this way, an attenuation profile is produced

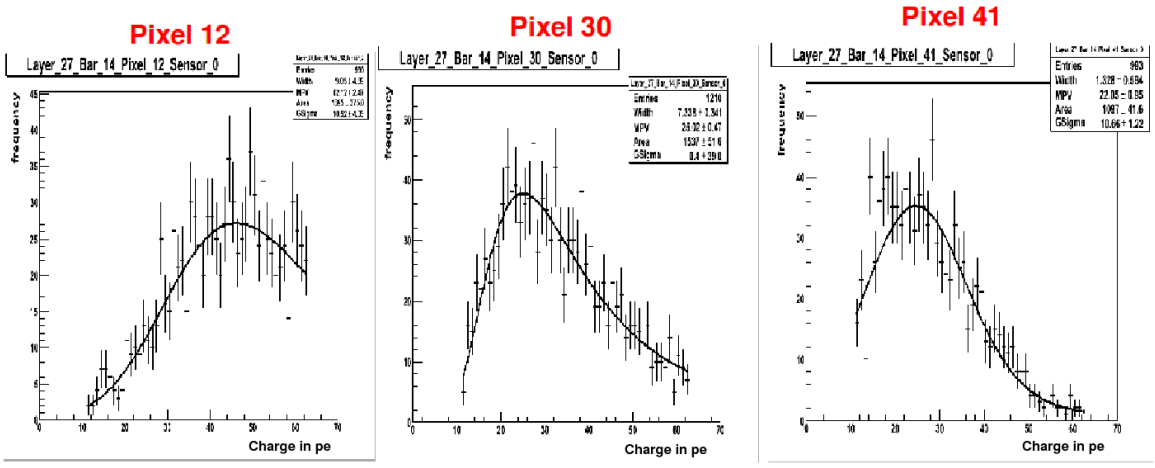

Figure 87: Example charge spectra for layer 27, bar 14 and photosensor/MPPC 0. The plots show pixels 12, 30 and 41 which are at positions 48 to 120 to 164 cm ±2 cm respectively from the MPPC. As the position of the hit moves further from the MPPC detecting it, the mean calibrated charge in photoelectrons detected decreases. In this case the MPV of the calibrated charge moves from 42.1±2.5, to 25.0±0.5, to 22.1±1.0 photoelectrons.

showing the MPV from the charge spectra as a function of position along the scintillator bar. This is found for each bar in each layer. The attenuation profile is fit with a double exponential, as shown in Equation 7.2.1. From this fit the short and long attenuation lengths and their errors along with their ratio and normalisation are determined for each bar. The short attenuation length is required to be between 20 and 70 cm and the long attenuation length is required to be between 100 and 800 cm. These cuts were selected based on the previous 2D scans and our observations that attenuation lengths outside of these ranges tend to appear from profiles where the fit does not match the data.

Figures 88 and 89 are example attenuation profiles, showing layer 27, bar 17 and photosensors 0 and 1 respectively. Only 42 and 46 out of the possible 48 pixels (as pixel 1 and 50 will not receive hits) for MPPC 0 and 1 respectively, that go to make up the bar were included in the plots, as the others failed the

χ^2 test (whoch is described in Section 7.2.4). The attenuation profiles have opposite gradients, as expected, as the MPPCs involved sit at opposing ends of the bar. The double exponential (Equation 7.2.1) is fit in the central region where it follows the data well. At the end of the bars the errors are seen to be much greater and the pe count gains or drops off rapidly. These end effects have not been simulated here as this is quite involved and is not necessary for the attenuation calibration. Similar end effects were also observed in the 2D scan data (see Section 3.4.6) but there were much smaller errors than for real data. The fit that was used to model the end effects for the scan data does not fit well to cosmic data and therefore was not used here. However, a separate study of these end effects could be performed later.

7.2.4 Validity Checks

Due to the nature of the DSECal cosmic trigger (which triggers on half of the detector) and two dead TFBs found during the CERN testbeam and cosmic running, there are some bars for which the statistics are too low to make an accurate attenuation correction. It was also found that the pixels near the ends of the bars and at bars along the edge of the detector received far fewer hits than those in the centre of the detector, meaning that these bars may also not have the statistics needed for an accurate attenuation calibration. For this reason, it is important to produce a set of validity checks that can be used to test the validity of the constants.

The objective of the validity tests is to flag pixels and subsequently bars where the fit does not accurately represent the data, this could be because the statistics are too low or the errors are too large for example. A χ^2 per number of degrees of freedom (NDF) test of the charge (per pixel) and attenuation (along the bar), is performed. The χ^2 tests how the data points deviate from

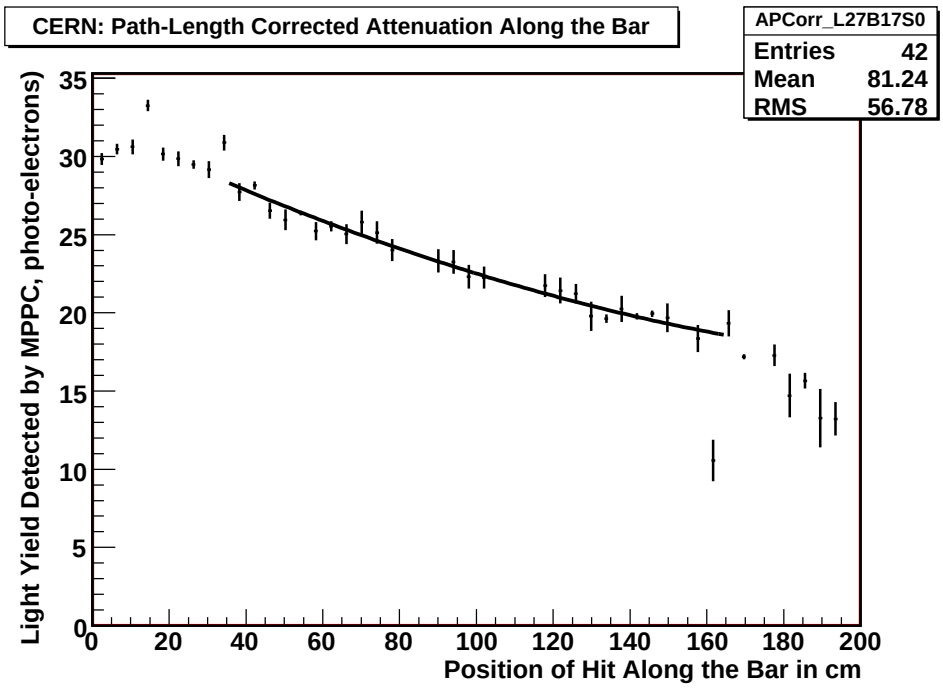

Figure 88: An example attenuation profile of charge spectra MPV for each pixel along a bar plotted as a function of the position of the cosmic ray track along the bar. This profile is for layer 27, bar 17 and photosensor 0 specifically. The fit works well for the central region but fails at the ends where there are lower statistics and the pe count drops. This is a well known effect that should not contribute significantly to the attenuation constants, but can be modelled later if desired.

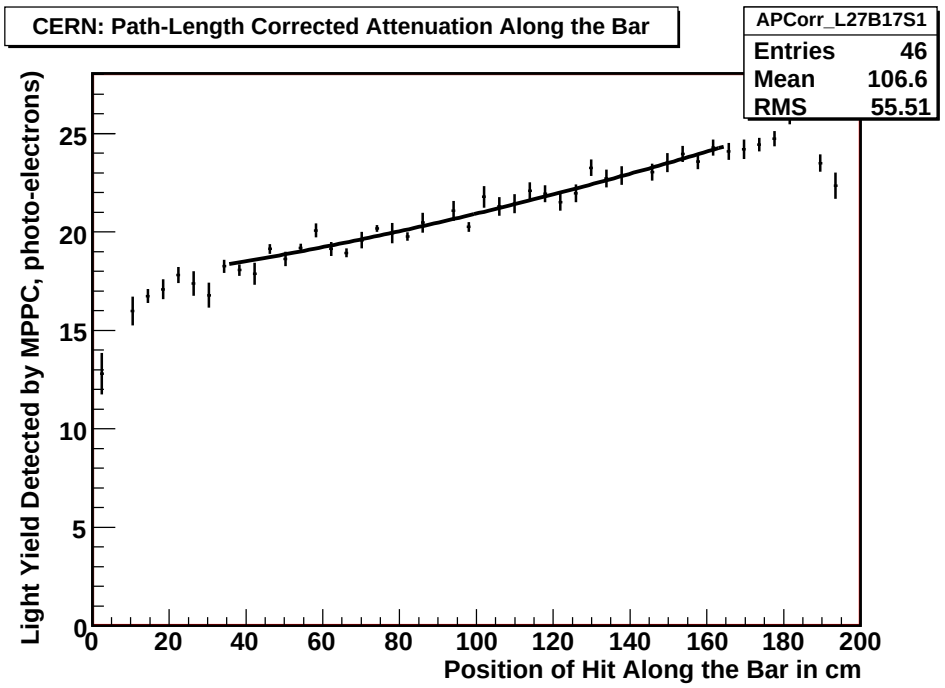

Figure 89: An example attenuation profile of charge spectra MPV for each pixel along a bar plotted as a function of the position of the cosmic ray track hits along the bar. This profile is for layer 27, bar 17 and photosensor 1 specifically. The fit works well for the central region but fails at the ends where there are lower statistics and the pe. count drops. This is a well known effect that should not contribute significantly to the attenuation constants, but can be modelled later if desired.

the fit and the the number of degrees of freedom (NDF) corresponds to the number of points used in the fit minus the number of free parameters. The χ^2 per NDF test is represented by Equation 7.2.4.

$$\chi^2/NDF = \frac{\sum_{i=0}^{n}(\frac{\Delta_i}{\sigma_i})}{n-f}, \tag{24}$$

where Δ is the deviation of each point i from the curve, σ is the size of the error bars, n is the number of data points and f is the nummber of free parameters in the fit.

The distribution of MPV (in pe) of the charge spectra at a given position along the bar (or pixel) are validated first. The MPV in pe at a given position (say 40 cm) along the bar, will vary between bars—as this is the purpose of the attenuation correction—however, huge differences are not expected. That is to say that at 40 cm (i.e pixel 10) along each of the bars of the DSECal, the MPV obtained from pixel 10 will not always be the same, but likewise should not be hugely different. Thus the χ^2 per NDF of the MPV in pe of a given pixel, for all bars in the detector is a good validity test. Figures 90, 91 and 92 show the MPV from the charge spectra at 40, 100 and 160 $\pm$2 cm respectively along the bar (equivalent to pixel 10, 25 and 40 respectively).

The plots show that, for the pixel in the centre of the bars, the distribution of MPVs agree well—with a χ^2 per NDF of around 1. The peak in the χ^2 per NDF moves from a mean of less than one at 40$\pm$2 cm from the MPPC, to around 1 at 100$\pm$2 cm—the centre of the bar—to a mean of greater than one at 160$\pm$2 cm from the MPPC. This maybe due to the fit worsening at greater distances fromthe MPPC. Nonetheless, the χ^2 per NDF is still very good.

We validate the attenuation profiles of each bar in the same way: by con-

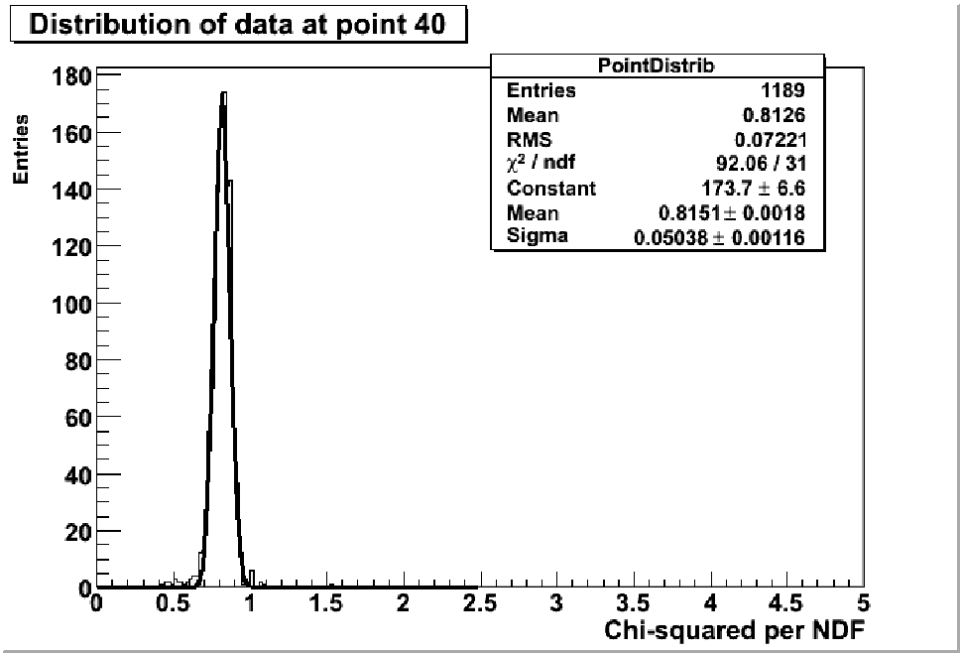

Figure 90: The χ^2 per NDF of the charge MPV in pe from CERN cosmic data, at 40 $\pm$2 cm (pixel 10) from the readout photosensor. Very little spread is seen in the MPV showing good agreement at this distance.

sidering the χ^2 per NDF of each profile (i.e. each bar). If the χ^2 per NDF > 2.5 then we reject the attenuation profile of that bar and no attenuation constants exist for that bar. In order that every bar has an atenuation calibration, we use the attenuation profiles of the nearest neighbouring bar—of the same orientation and readout end and that passsed the validity tests—to the bar that has failed, to represent the failed bar. This model is used as the nearest neighbour of a given bar is seen to have the closest approximation to the attenuation constants of that bar. Figure 93 shows the distribution of χ^2 per NDF for every bar of the DSECal using the CERN cosmic data. While many profiles fall within the acceptance region there are also quite a few which do not—which we expect.

The data taken at Tokai underwent the same testing. In this case, the number of bars which failed the χ^2 per NDF test of their attenuation profile

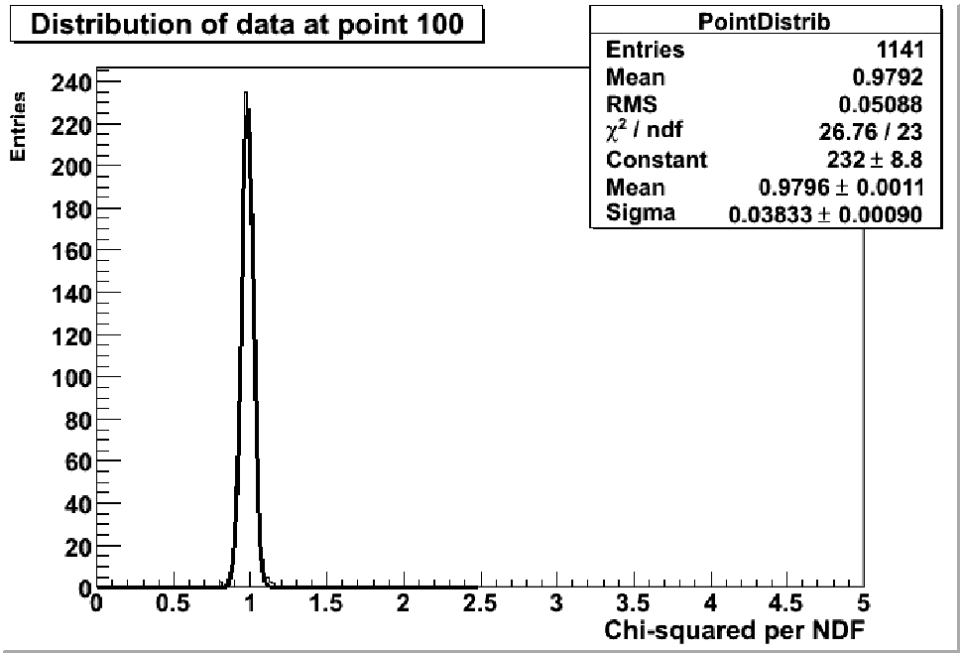

Figure 91: The χ^2 per NDF of the charge MPV from CERN cosmic data, at 100±2 cm (pixel 25 i.e. the centre of the bar) from the readout photosensor. Very little spread is seen in the MPV showing good agreement at this distance.

was greatly reduced, since the dead TFBs had been mended.

7.2.5 The Database Tables

The attenuation constants are stored in the nd280calib MYSQL (Reference [49]) database in a table named

`ECAL_BAR_ATTENUATION_CONST_TABLE,`

along with an accompanying validity table named

`ECAL_BAR_ATTENUATION_CONST_TABLEVLD.`

There are 12 attenuation constants stored in

`ECAL_BAR_ATTENUATION_CONST_TABLE:`

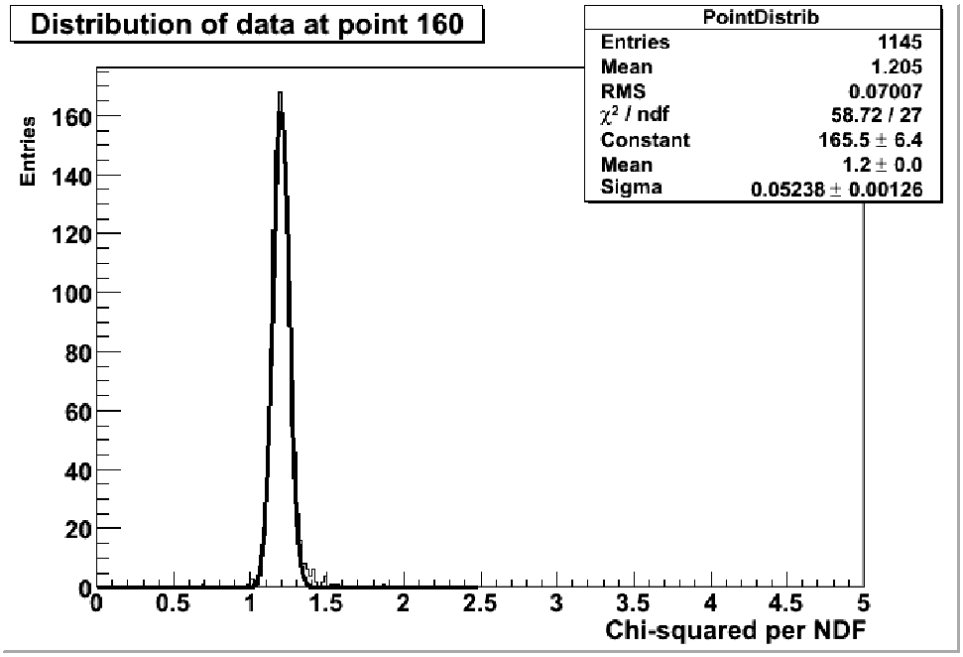

Figure 92: The χ^2 per NDF of the charge MPV from CERN cosmic data, at 160±2 cm (pixel 40) from the readout photosensor. Very little spread is seen in the MPV showing good agreement at this distance.

ECAL, LAYER, BAR, END, LONG, LONG ERR, SHORT, SHORT ERR, NORMALISATION, NORMALISATION ERR, RATIO and RATIO ERR.

ECAL is a numerical value representing which of the 13 ECal modules the subsequent constants, the number assigned to each ECal module is shown in Table 3.

LAYER and BAR represent the layer and bar of the given ECal module that the row of constants are for.

END represents the photosensor where 0 = sensor -1 and 1 = sensor 1.

LONG, LONG ERR, SHORT, SHORT ERR, NORMALISATION, NORMALISATION ERR, RATIO and RATIO ERR, give the attenuation constants their comparisons and errors.

The database table structure can be seen in Figure 95.

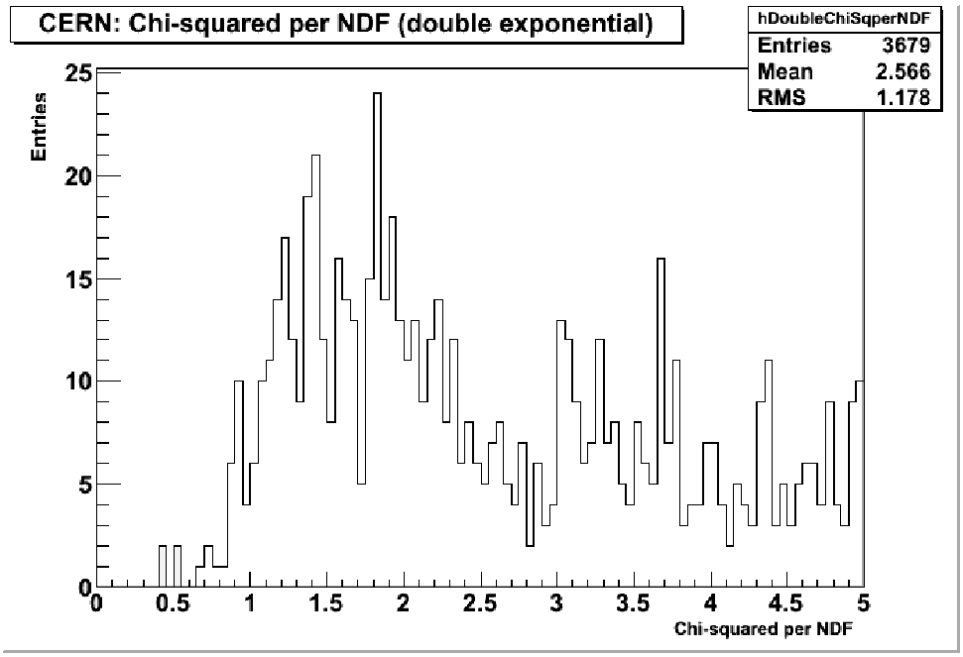

Figure 93: The χ^2 per NDF of the attenuation profiles for every bar of the DSECal using the cosmic data taken during the CERN testbeam and cosmics running. Those bars with a χ^2 per NDF greater than 2.5 fail the test and are replaced by that of their nearest neighbour with the same orientation.

DSECal	1
left top TECal	2
left middle TECal	3
left bottom TECal	4
right top TECal	5
right middle TECal	6
right bottom TECal	7
left top PECal	8
left middle PECal	9
left bottom PECal	10
right top PECal	11
right middle PECal	12
right bottom PECal	13

Table 3: The number assigned to represent each ECal module in the database table.

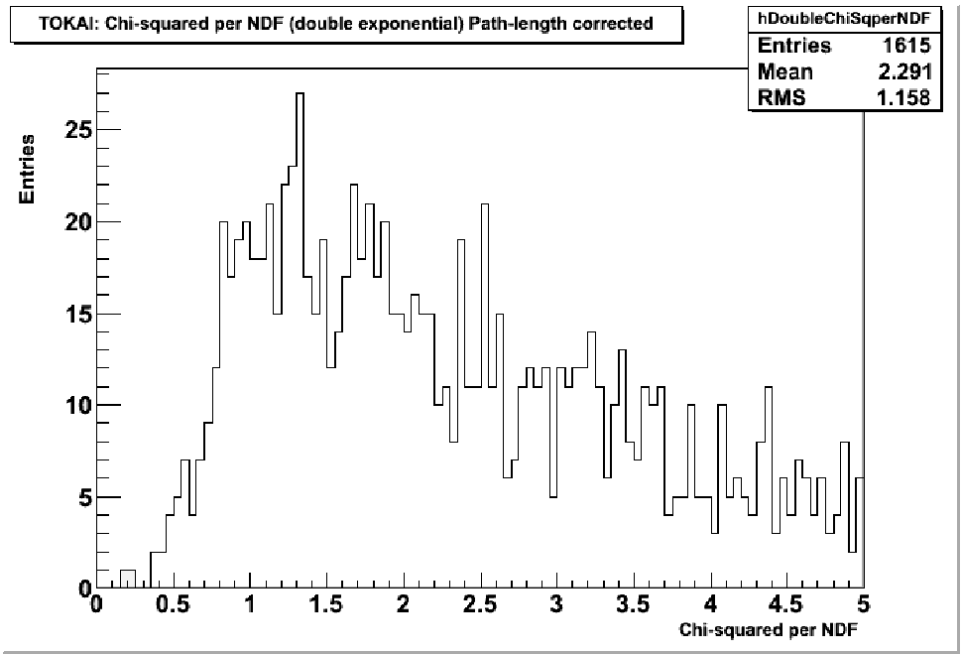

Figure 94: The χ^2 per NDF of the attenuation profiles for every bar of the DSECal using the cosmic data taken during the Tokai cosmic running. Those bars with a χ^2 per NDF greater than 2.5 fail the test and are replaced by that of their nearest neighbour with the same orientation.

Field	Type	Null	Key	Default	Extra
SEQNO	int(11)	NO	PRI		
ROW_COUNTER	int(11)	NO	PRI		
I_ECAL	int(11)	YES		NULL	
I_LAYER	int(11)	YES		NULL	
I_BAR	int(11)	YES		NULL	
I_END	int(11)	YES		NULL	
F_LONG	float	YES		NULL	
F_LONG_ERROR	float	YES		NULL	
F_SHORT	float	YES		NULL	
F_SHORT_ERROR	float	YES		NULL	
F_NORM	float	YES		NULL	
F_NORM_ERROR	float	YES		NULL	
F_RATIO	float	YES		NULL	
F_RATIO_ERROR	float	YES		NULL	

Figure 95: The structure of database table for the attenuation constants—ECAL_BAR_ATTENUATION_CONST_TABLE.

7.3 Using The Constants

The attenuation constants tables are read into the main software suite using three files named ECal_Bar_Attenuation_Const_Table.cxx/.hxx/_Linkdef respectively, and a wrapper file—TECALGetAttenuation, enabling the end user to use simple "get" functions without having to understand the inner workings of the code. All are stored in the source directory of ecalRecon. An end user will be able to return the the long, short normalisation and ratio values with errors for a given ECal, layer bar and photosensor, using GetLong, GetShort, GetNormalisation and GetRatio respectively and the attenuation value defined as in Equation 7.2.1, by calling GetAttenuation.

The attenuation correction is used by ecalRecon (for real data) and in elecSim (for Monte Carlo).

7.3.1 CERN Vs Tokai

Two dead TFBs were discovered during the CERN testbeam and cosmic running, which were later mended at Tokai prior to the installation of the DSECal in the ND280 pit (as I have already stated). For this reason the CERN data alone cannot be used to find the attenuation calibration constants for every bar of the DSECal. The period of cosmic running at Tokai when the detector was fully instrumented is needed and it is important to compare the attenuation profiles for the instrumented bars at Tokai and at CERN. Consistency—within reason—of the two data sets could allow them to be combined to increase statistics, thereby producing more accurate attenuation constants and allowing the bars affected by the dead TFBs at CERN to be corrected for attenuation. It is also important to use the Tokai data as the electronics were re-calibrated after the move to Tokai and these changes can also affect the attenuation calibration.

The first step in the attenuation calibration is to find the hit charge in pe of the selected muon tracks and therefore the charge distributions for selected cosmic hits at CERN and Tokai are compared first. Figure 96 shows the normalised charge distributions of the selected tracks that are used for the attenuation for Tokai (in red) and CERN (in black)—hits with a charge below 10 pe were not included in the attenuation correction. The shape of the distributions is due to the nature of the track finding algorithm (described above) which selects the highest (or second highest) charge tracks. The charge offset between the CERN and Tokai data is due to the re-calibration of the electronics at Tokai and in part, the inclusion of the TFBs that were dead at CERN.

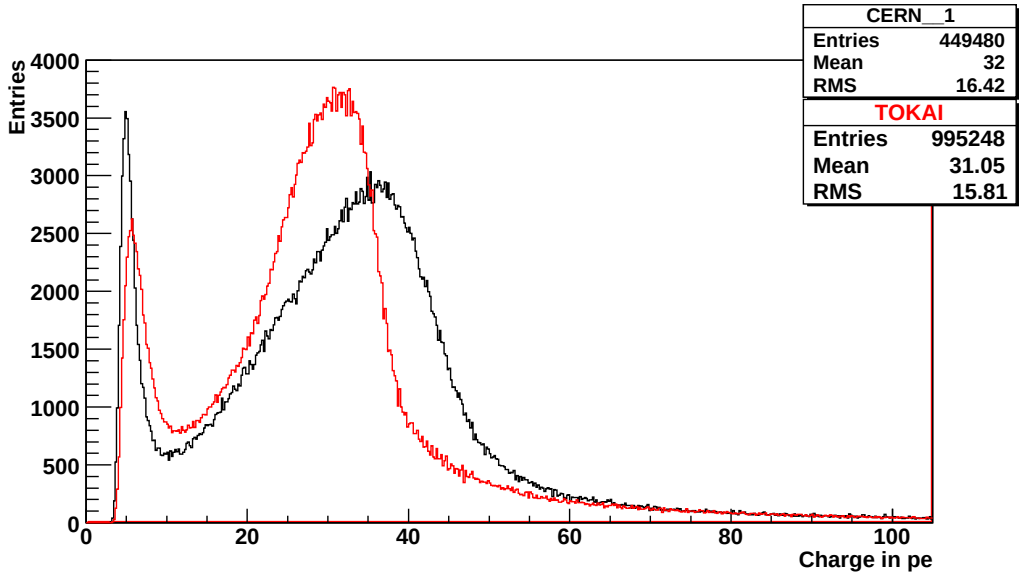

Figure 96: The normalised hit charge in pe of tracks saved by the track selecting algorithm for CERN cosmic data in black and Tokai cosmic data in red (charge less than 10 pe is not used to make attenuation plots).

The attenuation profiles of identical bars from the same readout MPPC at Tokai and CERN were compared. Figures 97 and 98 show the attenuation profiles for layer 15, bar 30 and MPPCs 0 and 1 respectively, for cosmic data

taken at CERN. Figures 99 and 100, show the attenuation profiles for the same bars and MPPCs but using Tokai cosmic data. There will of course be some differences in the attenuation constants produced using the two data sets, due to the movement of the detector during its shipping to Japan and the electronics that were changed and re-calibrated. However, the attenuation profiles from Tokai and CERN were found to compare well.

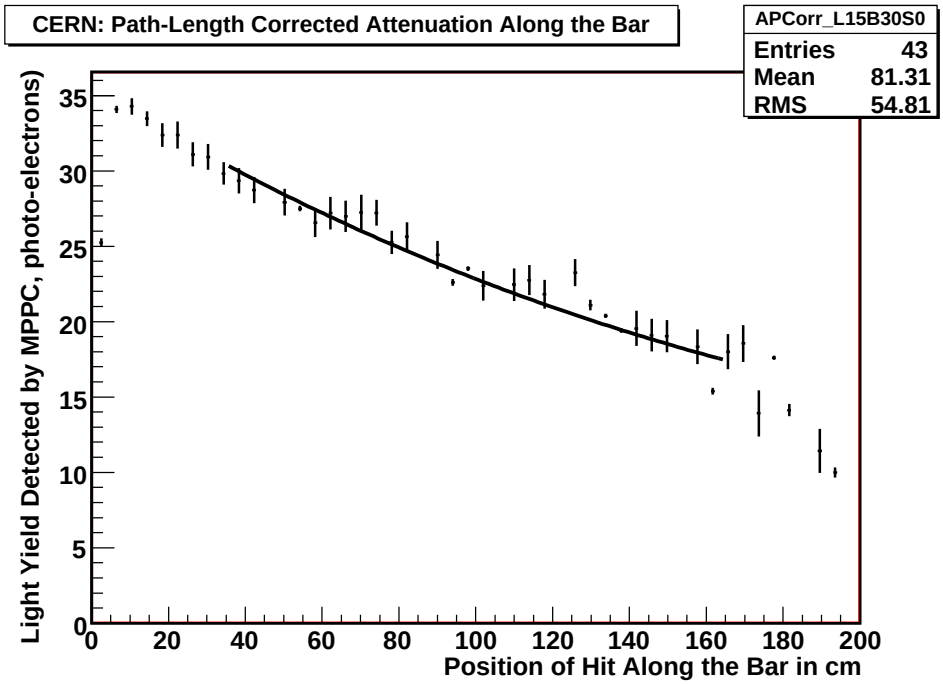

Figure 97: An example attenuation profile of charge spectra MPV for each pixel along a bar plotted as a function of the position of the cosmic ray track along the bar. This profile is for layer 15, bar 30 and photosensor 0, using cosmic data taken at CERN.

The distribution of the long and short attenuation lengths from the CERN and Tokai cosmic data can also be compared. Figures 101 and 102 show the distribution of long attenuation lengths from CERN and Tokai cosmic data respectively and Figures 103 and 104 show the distribution of short attenuation lengths—again from CERN and Tokai cosmic data respectively.

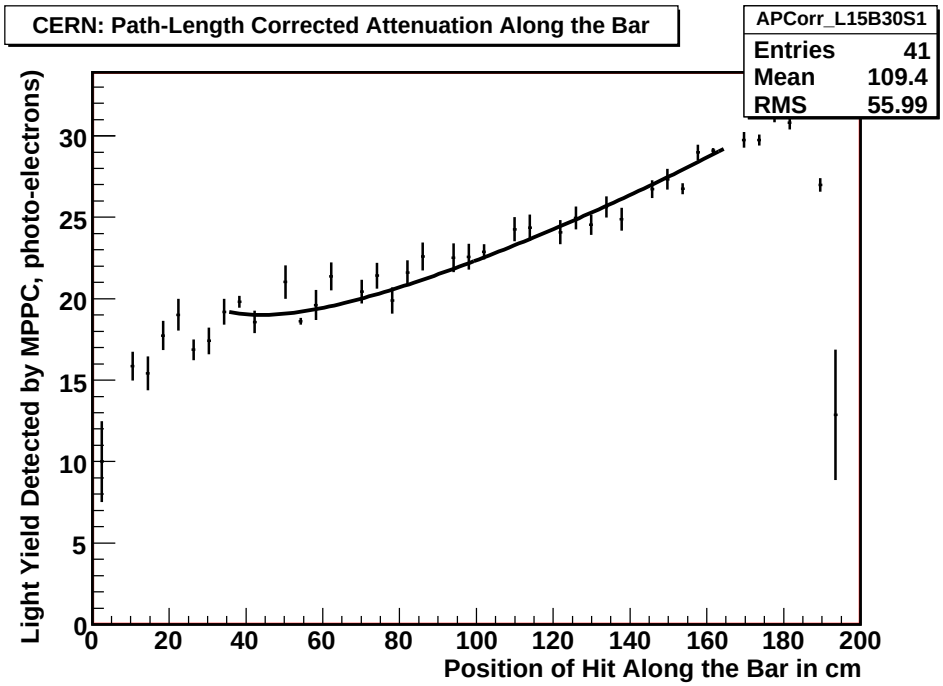

Figure 98: An example attenuation profile of charge spectra MPV for each pixel along a bar plotted as a function of the position of the cosmic ray track along the bar. This profile is for layer 15, bar 30 and photosensor 1, using cosmic data taken at CERN.

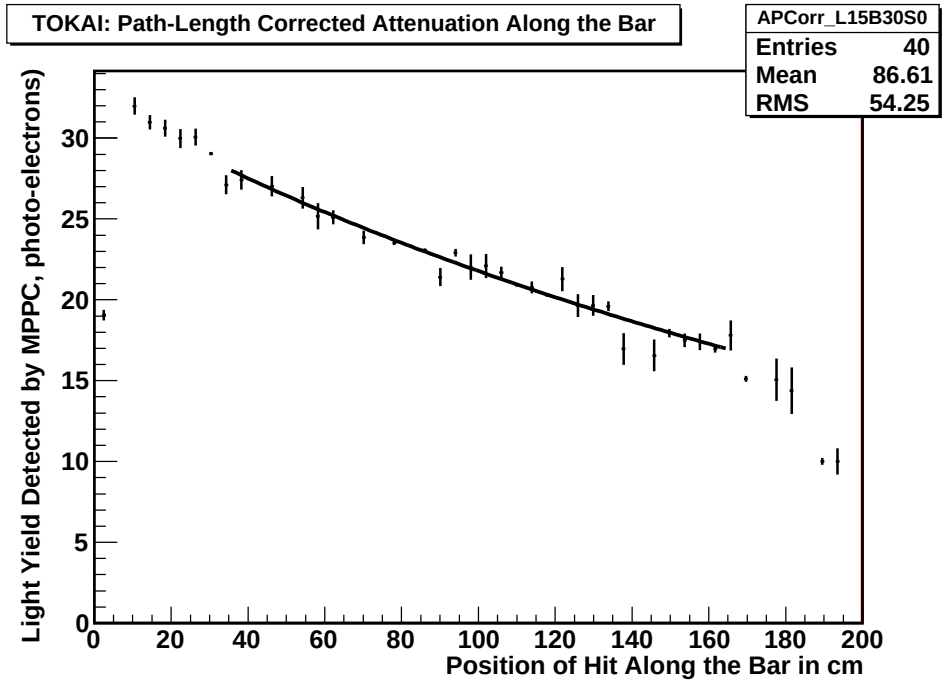

Figure 99: An example attenuation profile of charge spectra MPV for each pixel along a bar plotted as a function of the position of the cosmic ray track along the bar. This profile is for layer 15, bar 30 and photosensor 0, using cosmic data taken at Tokai. The profile is found to compare well with the data taken at CERN.

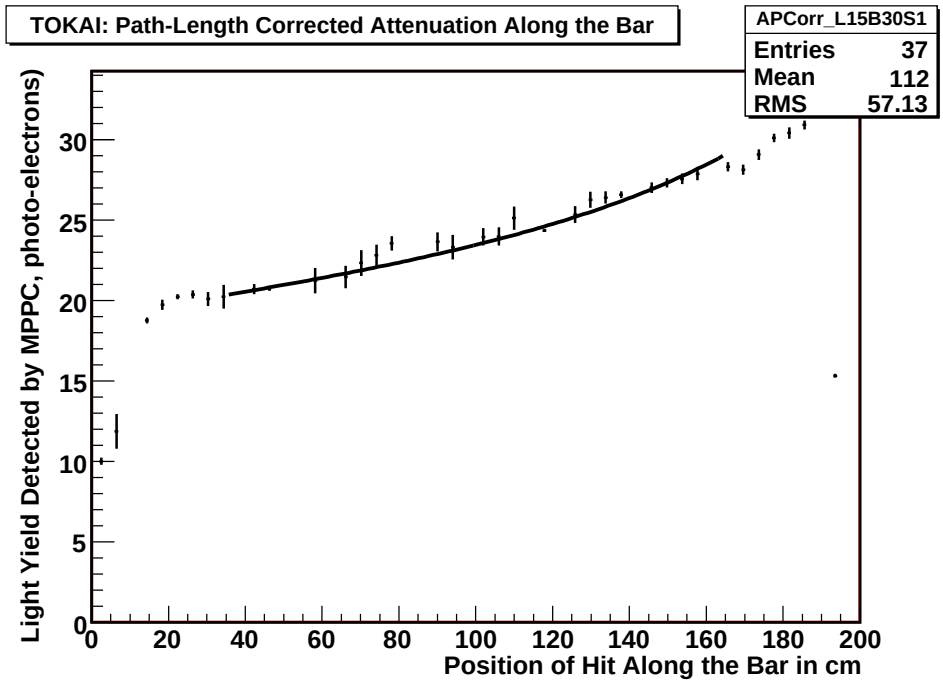

Figure 100: An example attenuation profile of charge spectra MPV for each pixel along a bar plotted as a function of the position of the cosmic ray track along the bar. This profile is for layer 15, bar 30 and photosensor 1, using cosmic data taken at Tokai. The profile is found to compare well with the data taken at CERN.

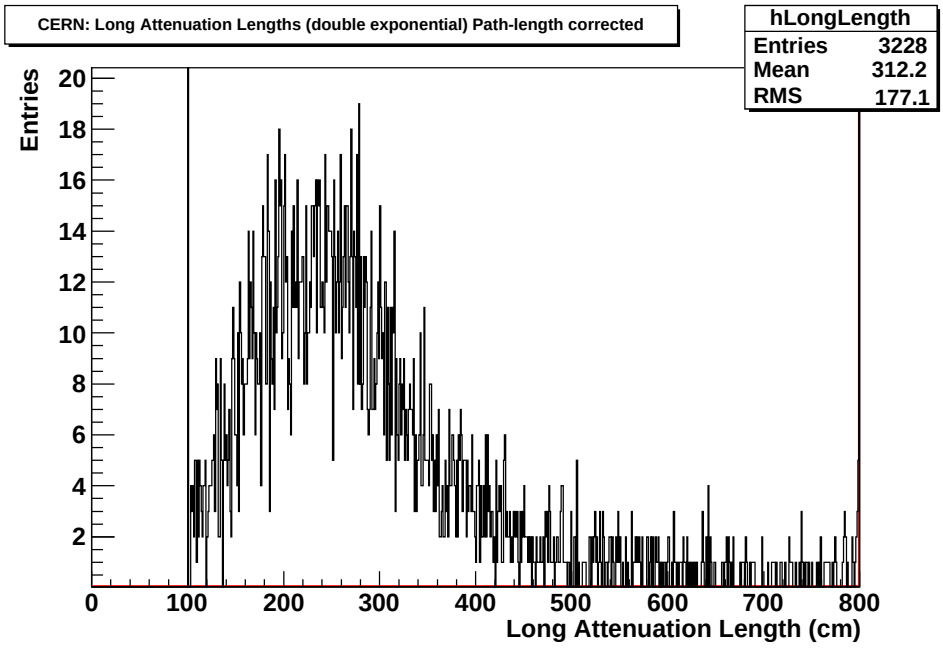

Figure 101: The distribution of the long attenuation lengths for all bars of the DSECal from cosmic data taken at CERN. Those bars with attenuation lengths of 100 or 800 cm failed the χ^2 test and their nearest neighbour approximation of the attenuation lengths are used. The errors are not shown as this plot is not for analysis but to compare the simple distributions and to see the number that fail the attenuation χ^2 test.

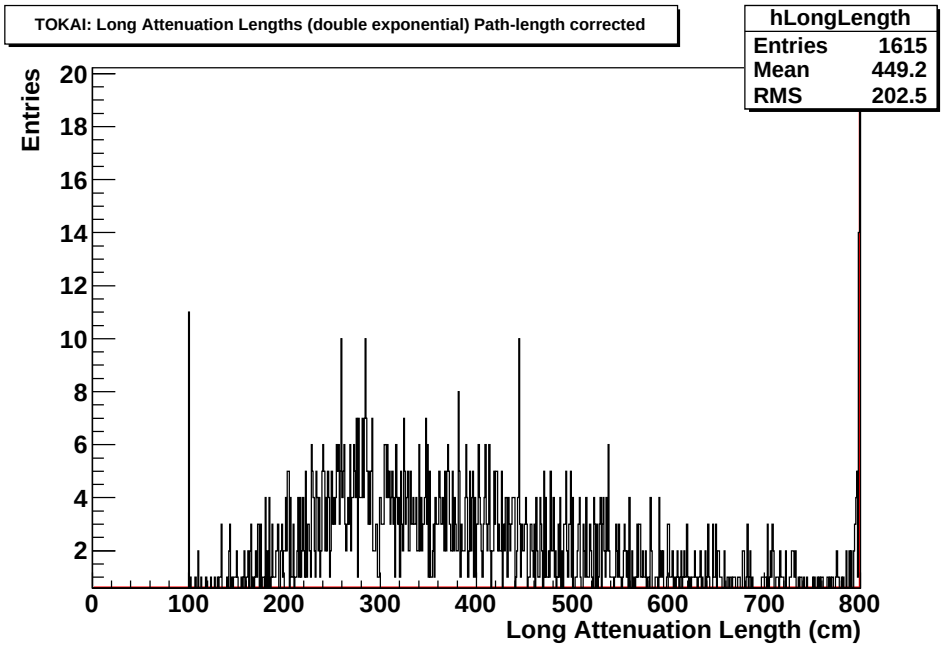

Figure 102: The distribution of the long attenuation lengths for all bars of the DSECal from cosmic data taken at Tokai. Those bars with attenuation lengths of 100 or 800 cm failed the χ^2 test and their nearest neighbour approximation of the attenuation lengths are used. The errors are not shown as this plot is not for analysis but to compare the simple distributions and to see the number that fail the attenuation χ^2 test.

There are two significant differences between the distributions of the long attenuation lengths for CERN and Tokai. The peak long attenuation length from Tokai data is around 25 cm greater than for CERN data. This is due to the re-calibration of the electronics. There are also far fewer bars failing the attenuation calibration for Tokai than for CERN. This is to be expected as the the two dead TFBs are alive in the Tokai cosmic data.

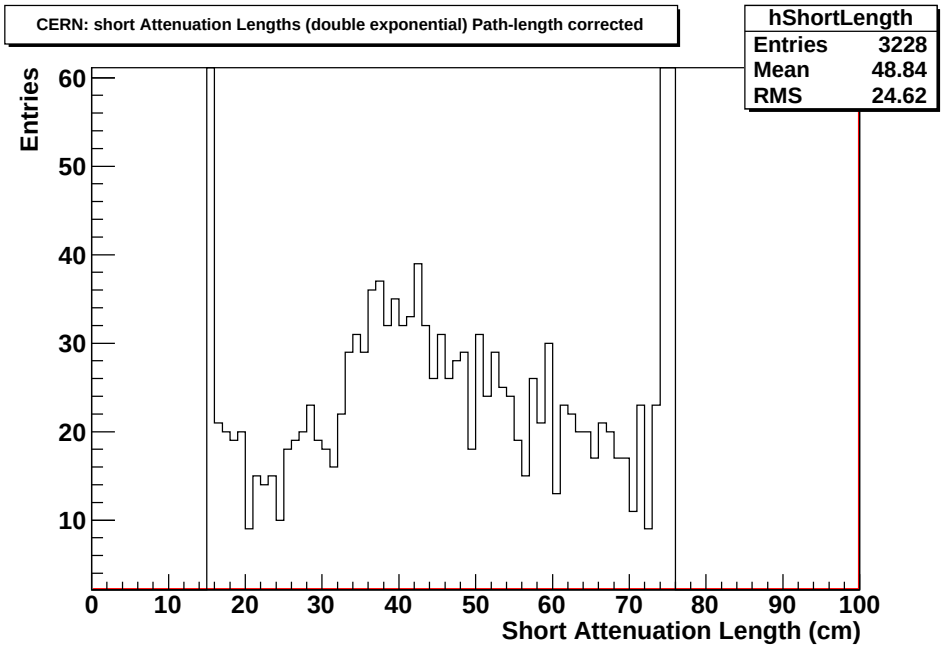

Figure 103: The distribution of the short attenuation lengths for all bars of the DSECal from cosmic data taken at CERN. Those bars with attenuation lengths of greater than 70 or less than 18 cm failed the χ^2 test and their nearest neighbour approximation of the attenuation lengths are used. The errors are not shown as this plot is not for analysis but to compare the simple distributions and to see the number that fail the attenuation χ^2 test.

The distributions of the short attenuation lengths for Tokai again show a greater peak length than for CERN, however, the peak in the Tokai distribution is a lot less defined in this case. Fewer bars are again observed to fail the χ^2 test at Tokai, due to the alive TFBs.

The differences in the Tokai and CERN data are caused in part by the

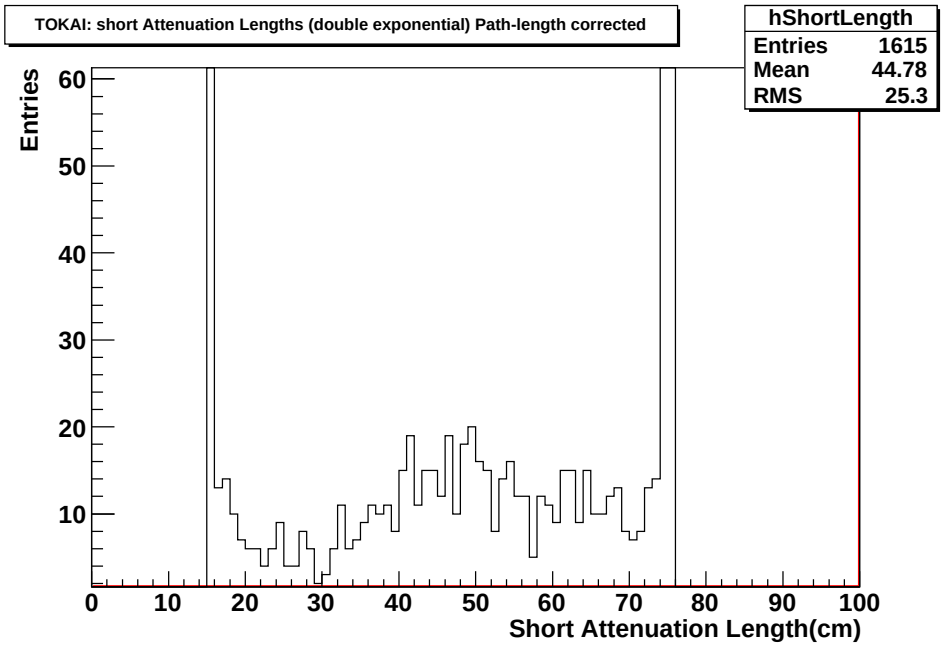

Figure 104: The distribution of the short attenuation lengths for all bars of the DSECal from cosmic data taken at Tokai. Those bars with attenuation lengths of greater than 70 or less than 18 cm failed the χ^2 test and their nearest neighbour approximation of the attenuation lengths are used. The errors are not shown as this plot is not for analysis but to compare the simple distributions and to see the number that fail the attenuation χ^2 test.

re-calibrated electronics and are therefore significant enough that the two data sets should not be combined, but rather the Tokai data set alone used for the first set of attenuation calibration constants. These constants have now been uploaded to the database.

7.3.2 The Attenuation Calibration For Future ECals

The various pieces of code which were made to produce this attenuation correction have been made available in the ND280 software, for use in future DSECal attenuation studies (since the attenuation correction will change with time). It is also designed to be used to produce the attenuation calibration constants for future ECal modules by simply changing the number of pixels, layers, bars and from double to single ended readout according to the dimensions of the ECal to be tested. The constants obtained from future runs can be added to the existing database table, remembering to change the first index in the table to represent the number of the ECal module to which the constants pertain, as described in Section 7.2.5. Later iterations of the attenuation correction can also be added to the existing table using a later creation date—which will be used preferentially over constants of an earlier creation date.

7.4 Cosmic Muon Monte Carlo to Data Comparison

The comparison of MC to data using cosmic muons can tell us many things about the experimental readiness of a detector and its software. The MC production tools must have accurate detector geometry representations, simulation of the cosmic trigger and full electronics simulation—as these are the things that will affect the validity of the MC. Also, the reconstruction and analysis tools must correctly implement the calibration and particle identifi-

cation (PID). Once all these things are in place, the MC should compare well with the data and the MC can be used to check the reconstruction tools.

I twice compared the cosmic muon data taken during the testbeam and commissioning run of the DSECal at CERN with the CERN cosmic MC. The first time was before the calibration and cosmic trigger had been implemented in the MC—to flag the work needing to be done in these areas from the differences between the MC and data. Then again, a second time after most of the calibration steps had been included and the reconstruction and PID were much further advanced. For this second run a simulation of the cosmic trigger was also used.

7.4.1 The Method

The comparisons were carried out after reconstruction and I therefore included it as an analysis macro in oaAnalysis (see Section 5.1.6). Whilst this analysis macro was used to analyse the DSECal only, it is designed to be run for any of the 13 ECal modules and is available within the software suite for this purpose. It will be run again for the next 12 ECal modules once they are ready for commissioning and calibration.

The energy spectrum and detector occupancy (distribution of hits within the DSECal) are compared for data and MC to test the reconstruction and cosmic trigger implementation. The directions of the muon tracks for data and MC are compared with MC propagation, reconstruction and PID.

7.4.2 Cosmic MC-Data Comparison of CERN Data

The post calibration MC and data files from the CERN testbeam cosmics run were produced at Queen Mary University of London. There were several million events available for both MC and data. A first pass of the cosmic

trigger was implemented for the MC and many of the calibration steps were included, but there are still more calibration steps which await conclusion and subsequent inclusion into the software.

The first thing to be considered is a hit map or detector occupancy plot, showing the bars and layers of the detector in 2D for the MC and data. This is very useful to see the obvious basic problems which may exist which can sometimes be hidden by the more high level quantities, such as directional comparisons.

Figure 105 shows the hit map for the CERN cosmic data for the DSECal lying down. Layers of the DSECal are shown on the vertical axis, while bars are shown on the horizontal axis. This was the same orientation as that of the detector during the cosmic tests. We can see the cosmics entering the detector from above. The hatched region in the top left of the plot shows the 2 broken TFBs which were later fixed in Tokai, but cannot be corrected in the CERN data. A higher density of cosmics is observed in the top half of the plot—layers 34-17—since the cosmic trigger triggers on this half of the detector. The hit map for data, therefore, looks as expected.

Consideration of the MC hit map demonstrated one obvious problem; the MC had been simulated entering the detector from the bottom, i.e. in the wrong direction. I produced a crude rerun which does not follow the full analysis chain, but allows some features of the MC to be compared to data using a hit map. Figure 106 shows this crude hit map for MC—using the CERN cosmic flux. The effect of the cosmic trigger can again be seen, but the clear cut off at the middle layer seen in data is no longer observed. This demonstrates that further work is needed to produce a more realistic DSECal cosmic trigger for MC simulation. More cosmic tracks are observed travelling vertically straight

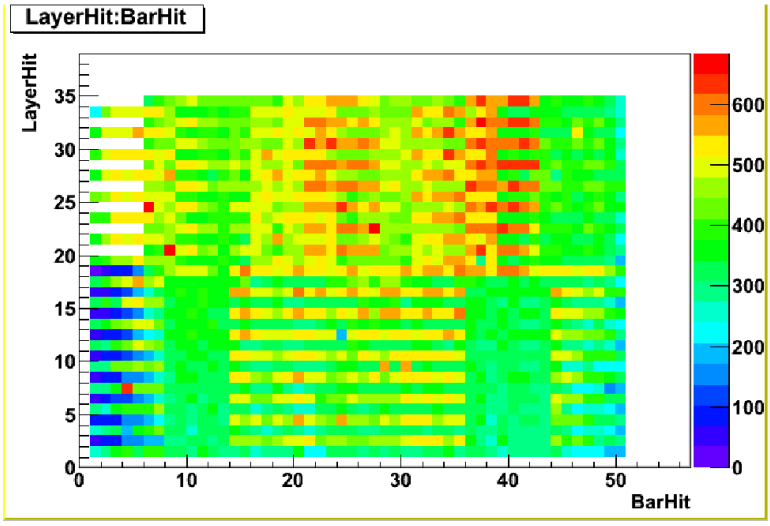

Figure 105: 2D representation of the DSECal in the flat (lying down) position, showing data hits in the bars and layers of the DSECal. The bars are shown on the horizontal axis and the layers on the vertical axis, the hit density by colour gradient is shown on the vertical bar on the left of the plot. The two dead TFBs can be seen in the hatched region of missing hits on the left top of the plot.

through the DSECal than in the data. This is due to the known effect of not having muons travelling horizontally at zenith angles of 70–90°. The MC hit map thereby demonstrates where improvements are needed and will need to be rerun through the full analysis chain for further analysis, but is beyond the timescale of this thesis.

A schematic showing the DSECal's orientation and what the bar and layer axes mean in these terms is shown in Figure 80.

The reconstructed "visible energy" in pe, for the CERN DSECal cosmic MC and data are compared in Figure 107. The MC is shown in red while the data is in black. There is a slight offset in the peak energy of < 0.3 pe higher peak energy for MC than for data. There is also less of a high energy tail for MC than the data which is expected, due to the lack of high angle muons in the cosmic flux MC which are also a large proportion of the muons with higher

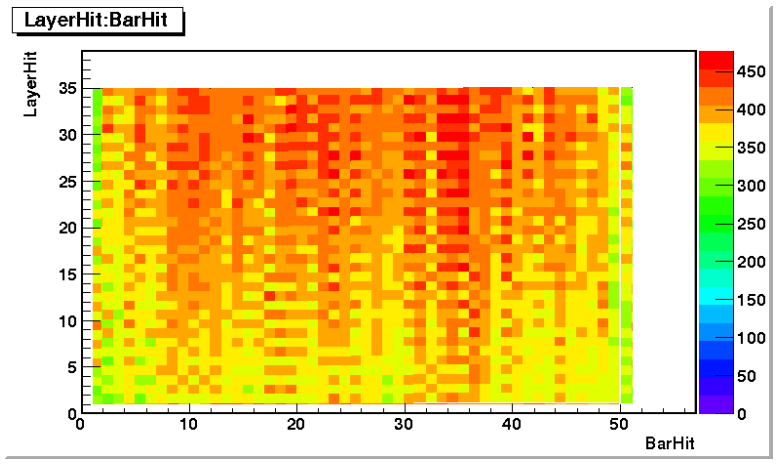

Figure 106: 2D representation of the DSECal in the flat (lying down) position, showing MC hits in the bars and layers of the DSECal. The bars are shown on the horizontal axis and the layers on the vertical axis, the hit density by colour gradient is shown on the vertical bar on the left of the plot. are observed than expected due to the lack of events in the flux at zenith angles of 70–90°.

energies, since to travel farther through the atmosphere and still to reach the detector they are usually required to be of higher energies.

The direction in x and y where $x = \sin\theta\cos\phi$ and $y = \sin\theta\sin\phi$ are shown for MC in Figure 108 and for data in Figure 109. The direction in z where $z = \cos\theta$ and consequently the angle of the tracks in degrees, cannot be compared until the cosmic MC has been rerun with the tracks in the correct direction. The directions in x and y, however, compare well, with the exception of the known differences in angular range between the MC and data.

7.5 Calibration Conclusions

Cosmic muons are an excellent tool for detector calibration as they often produce straight through going tracks that populate across the ECal.

I convened the UK cosmic muon analysis group whose work has improved the calibration of the DSECal dramatically, through, but not limited to: work

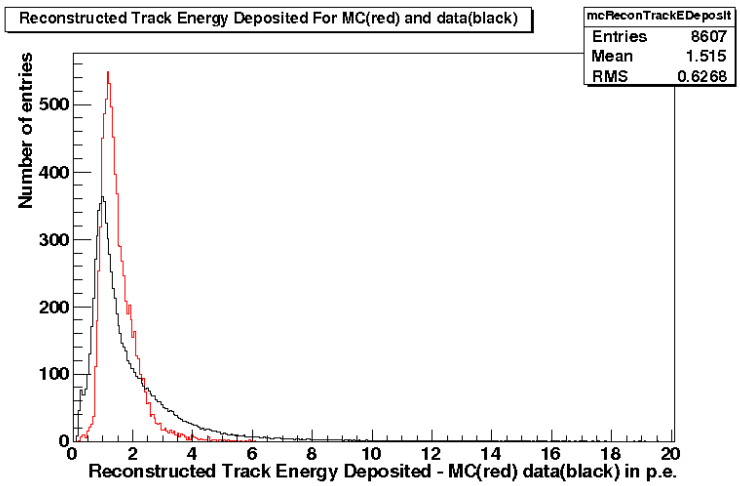

Figure 107: The MC (red) and data (black) cosmic muon energy in pe

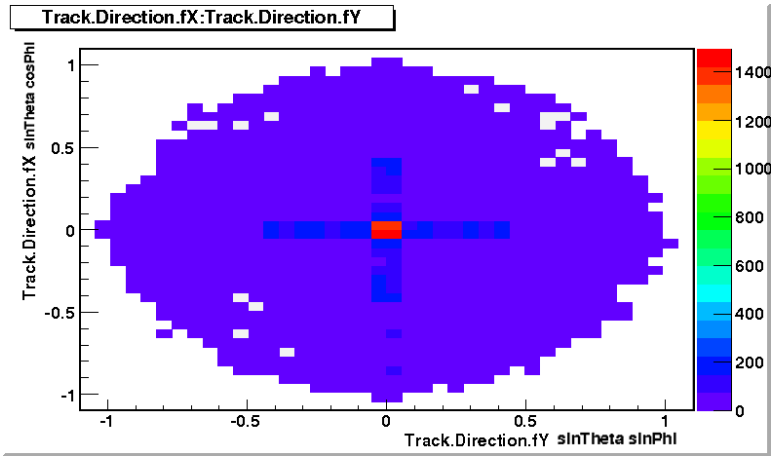

Figure 108: The direction of cosmic muon MC tracks in x and y where $\mathrm{X} = \sin\theta\cos\phi$ and $\mathrm{Y} = \sin\theta\sin\phi$.

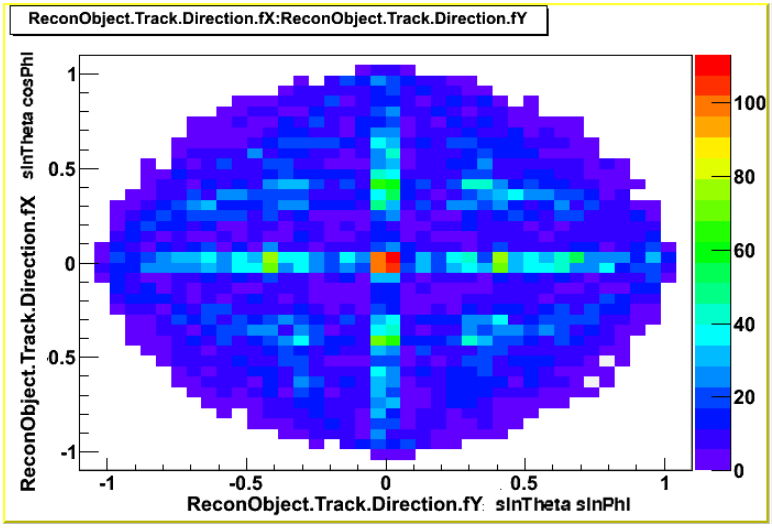

Figure 109: The direction of cosmic muon data tracks in x and y where $\mathrm{X} = \sin\theta\cos\phi$ and $\mathrm{Y} = \sin\theta\sin\phi$.

using the timing information; gain calibrations; identifying hot and dead channels; and performing studies of stopping muons and Michel electrons; as well as improving the reconstruction software.

I performed cosmic muon MC to data comparisons at various stages throughout the calibration process. The final results have shown that the calibration and reconstruction is in very good shape, but that there is some work needed to improve the implementation of the cosmic trigger for MC simulations, and the current cosmic MC from CERN needs to be remade (but compares well taking into account the ECal is positioned upside-down).

I also performed the attenuation correction for the DSECal with G. S. Davies of Lancaster University. Since the light from particles traversing the ECals will attenuate differently along different bars, it is important to understand these differences. We have now obtained the attenuation correction calibration constants for each bar of the DSECal. These constants are stored in a database and are used by the ECal reconstruction tools. The code is ready

to be used to produce the attenuation constants for the bars of the remaining 12 ECal modules when they are ready to be tested.

8 Conclusions

In this thesis I have shown the importance of the testing and calibration the ND280 sub-detector. I have also demonstrated the many uses of cosmic muon flux MC and cosmic muon data taking. These two main goals were achieved through the consideration of many of the T2K ND280 sub-detectors and in particular the DSECal, along with the novel MPPCs which are used by all but one of the ND280 sub-detectors.

I begin by describing the history of the neutrinos and of neutrino oscillations, outlining the major breakthroughs and the experiments which made them over the past few decades. I have explained the physics and mathematical representation of neutrino oscillations and shown those parameters which we are yet to measure fully. One such parameter is θ_{13}. Improving the sensitivity to θ_{13} by an order of magnitude is the main physics goal of T2K.

T2K is a long baseline neutrino oscillation experiment aiming to observe, for the first time, sub-dominant $\nu_\mu \rightarrow \nu_e$ oscillations. Situated in Japan, T2K consist of two detectors; the suite of near detectors (ND280) 280 m from the start of the beam—whose purpose is to characterise fully the 95% ν_μ, 4% $\overline{\nu}_\mu$ and $< 1\%$ ν_e beam and the interactions of neutrinos—and a far detector Super-Kamiokande 295 km away in Kamioka. The T2K experiment and its main physics goals, detectors and experimental readiness, are explained in Chapter 3. Here I also describe my work to characterise and test the MPPCs, prior to their installation in the tracker and P0D ECal modules.

I describe the T2K ND280 software in detail, as I have used it continuously and helped to develop it throughout my time working on T2K. I was the leader of the documentation task force and as such ensured the accurate documentation of the entire suite of software. I was also the sole producer of the T2K

ND280 Workbook. The Workbook is a guide to all aspects of work using the ND280 software and is designed for all levels of collaborator—with in-depth guides on how to get started for those new to T2K and also information for software developers and package managers.

It is essential to have a scientifically accurate cosmic muon flux specifically designed according to the conditions of the experiment, to be used for cosmic muon analysis studies. Such a flux was not in existence for the T2K ND280 collaboration. I produced the T2K ND280 cosmic flux which was used for the commissioning and calibration of all ND280 sub-detectors and which will continue to be used in the future. A simulation of the ND280 pit will be produced using the cosmic flux and subsequently a full MC will be produced. This flux and MC will be used for all future ND280 cosmic studies.

Cosmic muons are an essential calibration tool, as I have demonstrated throughout this thesis. They populate all areas of a detector with straight—often through going—tracks. Their unique and well understood nature enables accurate calibration studies to be performed, which is essential to accurate reconstruction. I convened the UK cosmic muon analysis group for the DSECal and I describe the work involved in Chapter 7. The work of the group helped to ensure that the DSECal was fully functional and well understood when it was installed in the ND280 pit, and it has been taking data since December 2009. I was responsible for cosmic MC and data comparison at various times throughout the commissioning and calibration process and have flagged many improvements that needed to be made to the software tools, calibration and to the detector itself. These improvements have helped to improve greatly the accuracy of the DSECal.

The nature of the scintillator bars of the ECals means that photons will

propagate differently along the bar depending upon the position along the bar at which a particle created them. This will vary between bars and photosensors. For this reason I and a colleague, produced the attenuation correction for the scintillator bars of the DSECal. This has allowed variations between how the bars propagate light—according to the position at which a hit was received—to be determined, and the long and short attenuation lengths and their associated errors, in addition to the total attenuation correction for that bar to be stored in a database. These calibration constants have improved the accuracy of the ECal reconstruction for the DSECal. All of the code pertaining to the attenuation correction has been saved and documented. This enables the attenuation corrections for the next 12 ECal modules to be determined easily, saved and used within the existing structure without further design and with minimal work. The attenuation correction is also described in Chapter 7.

My work within the T2K collaboration: assembling and testing the MPPCs; producing the ND280 Workbook; ensuring the adequate documentation of the ND280 software; producing the ND280 cosmic flux and calibrating the DSECal through the attenuation correction and MC data comparison; in addition to my leadership roles within T2K ND280, have been described. My work in these areas has helped to prepare T2K for data taking—which begun in late 2009.

A MainPage Doxygen Template

MainPage Doxygen Template

This is a basic template designed by the task force to show how the main pages should look. The basic structure here is an introduction, describing the very basic knowledge needed to understand what the package does and how to run it with defaults. Separate subsections should then be used to explain appropriate steps in more detail.

Introduction (max 1 page)

1. What? (Relate to physical ND280.) If possible relate the package back to the physical detector, i.e. for recon packages briefly describe your sub-detector and its output

2. Why? (what does it do?) The next part of the introduction should be describing the role the package plays. For example, elecSim simulates the ND280 electronics to provide reasonably accurate output responses from each detector. This modelling is used to test and develop the reconstruction packages.

3. How? (steps it takes to achieve the 'why'?) This part should describe how the package fulfils its role. Here the description should be reasonably brief, as most steps will require a further, more detailed description, placed in its own subsection outside the introduction.

4. How2? (How do we use it?) Finally there should be a brief explanation of how the package is used. Input file type and the package which created it should be stated here, along with the output type. Further I/O (input/output) and usage information should be given in a separate subsection. State nd280Control module to include when running from

nd280Control. Also, give an example of how to run the package without nd280control.

Subsections:

In many cases an increased number of subsections can help in the navigation through information contained in the main page. The idea being that topics introduced in the introduction such as the I/O of the packages, can be further explained for those interested, in a separate section in greater detail. As for how many and specific information about each package's subsections—these details are obviously best known by package managers. If further clarification, or examples of possible subsections for your package would help, please let us know.

If any subsection is more involved and requires more than a 1 page subsection, a separate Related Page should be created and a link to it given in the short subsection description.

Example Subsections:-

Where there are options to be set, these should be described. I/O explained in more detail. Any obvious subsections to package to have their own subsection e.g. Recon packages matching = subsection - clustering = subsection etc.

*****Further notes*****

1. Each time you refer to an object, please make the name of the object a link to the appropriate class. (This can be done simply using a

   ```
   '\ref'
   ```

   before the class, or object name.

2. When using any abbreviations or package or programming specific terms, please describe what they mean in brackets next to the term.

3. We found example code very useful, especially when trying to understand the use of an object. Please add appropriate examples where you can, and place them within:

   ```
   '\code'.
   ```

   .

B CORSIKA Datacards

RAL Datacard:

This is a script which produces datacards with sequential run numbers and different random seeds, each card producing 7500000 events. 200 consecutive datacards are run at one time and analysed as the next set is in production. The CORSIKA commands appear on the left and their meaning is on the right.

```
#!/bin/bash



#Define functions


writedatacard(){
cat <<EOF >datacard-$RunNo
RUNNR   $RunNo                      run number
EVTNR   1                           number of first shower event
NSHOW   $NSHOW                      number of showers to generate
SEED    998   0   0                 seed for 1. random number sequence
SEED    $RNDSEED2   0   0           seed for 2. random number sequence
PRMPAR  14                          particle type of prim. particle
ERANGE  1.E0 1.E5                   energy range of prim. particle in GeV
ESLOPE  -2.7                        slope of primary energy spectrum
THETAP  0.  70.                     range of zenith angle (degree)
PHIP    0.  360.                    range of azimuth angle (degree)
ATMOD   2                           atmospheric model
MAGNET  19.27  14.66                magnetic field
```

```
QGSJET  T 2                          QGSJET model
QGSSIG  T                            use QGSSIG
HADFLG  0  0  0  0  0  2             flags hadr.interact.&fragmentation
ELMFLG  T   T                        em. interaction flags (NKG,EGS)
STEPFC  1.0                          mult. scattering step length fact.
RADNKG  200.E2                       outer radius for NKG lat.dens.distr.
ECUTS   0.05 0.05 0.003 0.003        En cut-offs->hadrons, mu, e's, phot
MUADDI  T                            additional info for muons
MUMULT  T                            muon multiple scattering angle
ARRANG  0.                           rotation of array to north
OBSLEV  129.E2                       observation level (in cm)
FLUDBG  T                            create fluka debugs
DIRECT  /mnt/lustre/...CorsikaOutputUK/  output dir
PAROUT  F T                          write .tab particle file
USER    MAGeorge                     user
EXIT                                 terminates input
EOF
}


#Main Prog
##Maximum before crash aprox 6m 15sec
NSHOW=7500000
#NSHOW=5

RunNo=8500
```

```
for i in 3 4 5 6 7 8 9 ; do
   for j in 0 1 2 3 4 5 6 7 8 9 ; do
        for k in 0 1 2 3 4 5 6 7 8 9 ; do

            RNDSEED2=$i$j$k
            echo Run $RunNo Seed $RNDSEED2
            writedatacard
            RunNo=$(( $RunNo + 1 ))

            if [ "$RunNo" = 8700 ] ; then
                break 3
            fi
        done
    done
done
```

CERN Datacard:

This is a script which produces datacards with sequential run numbers and different random seeds, each card producing 7500000 events. 200 consecutive datacards are run at one time and analysed as the next set are in production. The CORSIKA commands appear on the left and their meaning on the right.

```
#!/bin/bash


#Define functions

writedatacard(){
cat <<EOF >datacard-$RunNo
RUNNR   $RunNo                      run number
EVTNR   1                           number of first shower event
NSHOW   $NSHOW                      number of showers to generate
SEED    $RNDSEED   0   0            seed for 1. random number sequence
SEED    100   0   0                 seed for 2. random number sequence
PRMPAR  14                          particle type of prim. particle
ERANGE  1.E0 1.E5                   energy range of prim. particle in GeV
ESLOPE  -2.7                        slope of primary energy spectrum
THETAP  0.  70.                     range of zenith angle (degree)
PHIP    0.  360.                    range of azimuth angle (degree)
ATMOD   4                           atmospheric model
MAGNET  22.10  41.77                magnetic field CERN
QGSJET  T 2                         QGSJET model
```

```
QGSSIG  T                          use QGSSIG
HADFLG  0  0  0  0  0  2           flags hadr.interact.&fragmentation
ELMFLG  T   T                      em. interaction flags (NKG,EGS)
STEPFC  1.0                        mult. scattering step length fact.
RADNKG  200.E2                     outer radius for NKG lat.dens.distr.
ECUTS   0.05 0.05 0.003 0.003      En cut-offs->hadrons, mu, e's, phot.
MUADDI  T                          additional info for muons
MUMULT  T                          muon multiple scattering angle
ARRANG  0.                         rotation of array to north
OBSLEV  375.E2                     observation level (in cm) of Geneva
FLUDBG  T                          create fluka debugs
DIRECT  /mnt/lustre/...CorsikaOutputCERN/ output dir
PAROUT  F T                        write .tab particle file
USER    MAGeorge                   user
EXIT                               terminates input
EOF
}


#Main Prog

NSHOW=7500000
#NSHOW=5

RunNo=1400
```

```
for i in 5 6 7 8 9 ; do
    for j in 0 1 2 3 4 5 6 7 8 9 ; do
        for k in 0 1 2 3 4 5 6 7 8 9 ; do

            RNDSEED=$i$j$k
            echo Run $RunNo Seed $RNDSEED
            writedatacard
            RunNo=$(( $RunNo + 1 ))

            if [ "$RunNo" = 1800 ] ; then
                break 3
            fi
        done
    done
done
```

TRIUMF Datacard:

This is a script which produces datacards with sequential run numbers and different random seeds, each card producing 7500000 events. 200 consecutive datacards are run at one time and analysed as the next set is in production. The CORSIKA commands appear on the left and their meaning on the right.

```
#!/bin/bash


#Define functions

writedatacard(){
cat <<EOF >datacard-$RunNo
RUNNR   $RunNo                      run number
EVTNR   1                           number of first shower event
NSHOW   $NSHOW                      number of showers to generate
SEED    $RNDSEED   0   0            seed for 1. random number sequence
SEED    100   0   0                 seed for 2. random number sequence
PRMPAR  14                          particle type of prim. particle
ERANGE  1.E0 1.E5                   energy range of prim. particle in GeV
ESLOPE  -2.7                        slope of primary energy spectrum
THETAP  0.  70.                     range of zenith angle (degree)
PHIP    0.  360.                    range of azimuth angle (degree)
ATMOD   1                           atmospheric model
MAGNET  18.53  51.90                magnetic field
QGSJET  T 2                         QGSJET model
```

```
QGSSIG  T                           use QGSSIG
HADFLG  0  0  0  0  0  2            flags hadr.interact.&fragmentation
ELMFLG  T   T                       em. interaction flags (NKG,EGS)
STEPFC  1.0                         mult. scattering step length fact.
RADNKG  200.E2                      outer radius for NKG lat.dens.distr.
ECUTS   0.05 0.05 0.003 0.003       En cut-offs for hadrons, mu, e's, phot
MUADDI  T                           additional info for muons
MUMULT  T                           muon multiple scattering angle
ARRANG  0.                          rotation of array to north
OBSLEV  -10.E2                      observation level
FLUDBG  T                           create fluka debugs
DIRECT  /mnt/lustre/.../CorsikaOutputTRIUMF/ output dir
PAROUT  F T                         write .tab particle file
USER    MAGeorge                    user
EXIT                                terminates input
EOF
}


#Main Prog

NSHOW=7500000
#NSHOW=5

RunNo=1000
```

```
for i in 1 2 3 4 5 6 7 8 9 ; do
    for j in 0 1 2 3 4 5 6 7 8 9 ; do
        for k in 0 1 2 3 4 5 6 7 8 9 ; do
            RNDSEED=$i$j$k
            echo Run $RunNo Seed $RNDSEED
            writedatacard
            RunNo=$(( $RunNo + 1 ))

            if [ "$RunNo" = 1500 ] ; then
                break 3
            fi
        done
    done
done
```

Tokai Datacard:

This is a script which produces datacards with sequential run numbers and different random seeds, each card produces 7500000 events. 200 consecutive datacards are run at one time and analysed as the next set is in production. The CORSIKA commands appear on the left and their meaning on the right.

```
#!/bin/bash


#Define functions

writedatacard(){
cRUNNR   $RunNo                    run number
EVTNR    1                         number of first shower event
NSHOW    $NSHOW                    number of showers to generate
SEED     $RNDSEED   0   0          seed for 1. random number sequence
SEED     101    0   0              seed for 2. random number sequence
PRMPAR   14                        particle type of prim. particle
ERANGE   1.E0 1.E5                 energy range of prim particle in GeV
ESLOPE   -2.7                      slope of primary energy spectrum
THETAP   0.  70.                   range of zenith angle (degree)
PHIP     0.  360.                  range of azimuth angle (degree)
ATMOD    1                         atmospheric model
MAGNET   30.77  35.02              magnetic field
QGSJET   T 2                       QGSJET model
QGSSIG   T                         use QGSSIG
```

```
HADFLG  0  0  0  0  0  2          flags hadr.interact.&fragmentation
ELMFLG  T   T                     em. interaction flags (NKG,EGS)
STEPFC  1.0                       mult. scattering step length fact.
RADNKG  200.E2                    outer radius for NKG lat.dens.distr.
ECUTS   0.05 0.05 0.003 0.003     En cut-offs for hadrons, mu, e's, phot
MUADDI  T                         additional info for muons
MUMULT  T                         muon multiple scattering angle
ARRANG  0.                        rotation of array to north
OBSLEV  -169.E1                   observation level (in cm)
FLUDBG  T                         create fluka debugs
DIRECT  /mnt/lustre/.../CorsikaOutputTokai/  output dir
at <<EOF >datacard-$RunNo
PAROUT  F T                       write .tab particle file
USER    MAGeorge                  user
EXIT                              terminates input
EOF
}


#Main Prog

NSHOW=7500000
#NSHOW=5

RunNo=1800
```

```
for i in 1 2 3 4 5 6 7 8 9 ; do
    for j in 0 1 2 3 4 5 6 7 8 9 ; do
        for k in 0 1 2 3 4 5 6 7 8 9 ; do

            RNDSEED=$i$j$k
            echo Run $RunNo Seed $RNDSEED
            writedatacard
            RunNo=$(( $RunNo + 1 ))
if [ "$RunNo" = 2199 ] ; then
                break 3
            fi
        done
    done
done
```

References

[1] W. C. Haxton, *Edward Teller and Nuclei: Along the Trail to the Neutrino* (2008), `0808.1098`.

[2] F. Reines and C. L. Cowan, *The neutrino*, Nature, vol. 178, 446–449 (1956).

[3] G. Danby et al., *Observation of High-Energy Neutrino Reactions and the Existence of Two Kinds of Neutrinos,*, Phys. Rev. Lett., vol. 9, 36–44 (1962).

[4] K. Kodama et al., *Identification of neutrino interactions using the DONUT spectrometer*, Nucl. Instrum. Meth., vol. A516, 21–33 (2004).

[5] B. Pontecorvo, *Inverse beta processes and nonconservation of lepton charge*, Sov. Phys. JETP, vol. 7, 172–173 (1958).

[6] Z. Maki, M. Nakagawa and S. Sakata, *Remarks on the unified model of elementary particles*, Prog. Theor. Phys., vol. 28, 870–880 (1962).

[7] M. Herrero, *The Standard model* (1998), `hep-ph/9812242`.

[8] J. N. Bahcall, *Standard solar models*, Nucl. Phys. Proc. Suppl., vol. 77, 64–72 (1999), `astro-ph/9808162`.

[9] E. G. Adelberger, *Solar fusion cross sections II: the pp chain and CNO cycles* (2010).

[10] A. Kopylov and V. Petukhov, *Neutrinos from CNO cycle at the present epoch of the solar neutrino research*, Prog. Part. Nucl. Phys., vol. 64, 423–425 (2010).

[11] A. Bandyopadhyay, S. Choubey, S. Goswami and D. P. Roy, *Implications of the first neutral current data from SNO for solar neutrino oscillation*, Phys. Lett., vol. B540, 14–19 (2002), hep-ph/0204286.

[12] G. L. Fogli et al., *Addendum to: Solar neutrino oscillation parameters after first KamLAND results*, Phys. Rev., vol. D69, 017301 (2004), hep-ph/0308055.

[13] I. M. Brancus, *Lateral charged particle distribution of extensive air showers: Source of information about energy and nature of the primary cosmic particles*, Rom. Rep. Phys., vol. 59, 311–321 (2007).

[14] A. De Santo, *An experimentalist's view of neutrino oscillations*, Int. J. Mod. Phys., vol. A16, 4085–4152 (2001), hep-ex/0106089.

[15] Super Kamiokande Collaboration, http://neutrino.phys.washington.edu/ superk/.

[16] Y. Ashie et al., *A Measurement of Atmospheric Neutrino Oscillation Parameters by Super-Kamiokande I*, Phys. Rev., vol. D71, 112005 (2005), hep-ex/0501064.

[17] P. Adamson et al. (MINOS), *Observation of muon intensity variations by season with the MINOS far detector,*, Phys. Rev., vol. D81, 012001 (2010), 0909.4012.

[18] Q. Y. Liu, S. P. Mikheyev and A. Y. Smirnov, *Parametric resonance in oscillations of atmospheric neutrinos?*, Phys. Lett., vol. B440, 319–326 (1998), hep-ph/9803415.

[19] M. Apollonio et al. (CHOOZ), *Limits on Neutrino Oscillations from the CHOOZ Experiment*, Phys. Lett., vol. B466, 415–430 (1999).

[20] A. A. Aguilar-Arevalo et al., *The Neutrino Flux prediction at MiniBooNE*, Phys. Rev., vol. D79, 072002 (2009), 0806.1449.

[21] MINOS collaboration (2010), proceedings of the Neutrino 2010 Conference.

[22] T2K Collaboration, *T2K Official Plot* (2010).

[23] M. Pimia, *Track finding in the UA1 central detector at the CERN $p\bar{p}$ collider* (1985), hU-P-D45.

[24] S. Anvar et al., *Large bulk Micromegas detectors for TPC applications*, Nucl. Instrum. Meth., vol. A602, 415–420 (2009).

[25] G. Bondarenko et al., *Silicon Photomultipliers* , Nuclear Phys. Proc., vol. 61B (1998).

[26] S. Cova et al., *Avalanche photodiodes and quenching circuits for single-photon detection* , Applied Optics (1996).

[27] S. Gomi et al., *Development of Multi-Pixel Photon Counters*, Nuclear Science Symposium Conference Record, IEEE, vol. 2, 1105–1111 (2006).

[28] A. Zylberstejn (D0), *Selected preliminary results from the D0 experiment*, presented at 23rd International Symposium on Ultra-High Energy Multiparticle Phenomena, Aspen, CO, 12-17 Sep 1993.

[29] A. Vacheret et al., *The Front End Readout System For The T2K-ND280 Detectors,*, Nuclear Science Symposium Conference Record, IEEE, vol. 3, 1984–1991 (2007).

[30] R. D. Russell, *MIDAS: A MULTILEVEL INTERACTIVE DATA ACQUISITION SYSTEM*, IEEE Trans. Nucl. Sci., vol. 16, 122–126 (1969).

[31] C. Arnault, *CMT: A software configuration management tool*, prepared for International Conference on Computing in High- Energy Physics and Nuclear Physics (CHEP 2000), Padova, Italy, 7-11 Feb 2000.

[32] S. Lopienski, I. Reguero and M. Guijarro, *Cluster architectures used to provide CERN central CVS service*.

[33] I. Antcheva et al., *ROOT: A C++ framework for petabyte data storage, statistical analysis and visualization*, Comput. Phys. Commun., vol. 180, 2499–2512 (2009).

[34] J. Apostolakis, *Geometry in Geant 4*, talk given at Computing in High-energy Physics (CHEP 97), Berlin, Germany, 7-11 Apr 1997.

[35] J. Arabnia, Ni and S. Wang, *Proceeding of the 2005 International Conference on Grid Computing and Applications (GCA'05)*, iSBN 1-932415-57-2, CSREA Press.

[36] Y. Uchida (2010), private communication by Yoshi Uchida.

[37] D. Heck et al., *Report FZKA 6019* (1998), http://wwwik.fzk.de/corsika/physics description/corsika phys.html.

[38] T. Antoni et al. (KASCADE), *The Cosmic ray experiment KASCADE*, Nucl. Instrum. Meth., vol. A513, 490–510 (2003).

[39] A. Haungs et al. (KASCADE-Grande), *The air-shower experiment KASCADE-Grande*, Nucl. Phys. Proc. Suppl., vol. 196, 80–85 (2009).

[40] N. N. Kalmykov, S. S. Ostapchenko and A. I. Pavlov, *Quark-gluon string model and EAS simulation problems at ultra-high energies*, Nucl. Phys. Proc. Suppl., vol. 52B, 17–28 (1997).

[41] A. Fasso et al., *The physics models of FLUKA: Status and recent development* (2003), hep-ph/0306267.

[42] C. Amsler et al. (Particle Data Group), *Review of particle physics*, Phys. Lett., vol. B667 (2008).

[43] D. Casper, *The NUANCE neutrino physics simulation, and the future*, Nucl. Phys. Proc. Suppl., vol. 112, 161–170 (2002), hep-ph/0208030.

[44] M. Hillas (1988), private communication by M. Hillas.

[45] M. Besnier (2010), private communication by M. Besnier.

[46] The TPC sub-detector group, private communication by The TPC sub-detector group.

[47] A. Masliah, P. Vacheret and J. Dobson, *elecSim Status, Aug 2010* (2010).

[48] M. Murdoch (2009), private communication by Matthew Murdoch.

[49] R. Tsenov, *MYSQL Data-Base Applications for DST-Like Physics Analysis*, prepared for 8th International Conference on Advanced Technology and Particle Physics (ICATPP 2003): Astroparticle, Particle, Space Physics, Detectors and Medical Physics Applications, Como, Italy, 6-10 Oct 2003.